2021

UNDERSTANDING THE EFFECTS OF WATER VAPOR AND TEMPERATURE ON AEROSOL USING NOVEL MEASUREMENT METHODS

Tyler Jacob Capek
Michigan Technological University, tjcapek@mtu.edu

UNDERSTANDING THE EFFECTS OF WATER VAPOR AND TEMPERATURE ON AEROSOL USING NOVEL MEASUREMENT METHODS

By

Tyler J. Capek

A DISSERTATION

Submitted in partial fulfillment of the requirements for the degree of

DOCTOR OF PHILOSOPHY

In Physics

MICHIGAN TECHNOLOGICAL UNIVERSITY

2021

This dissertation has been approved in partial fulfillment of the requirements for the Degree of DOCTOR OF PHILOSOPHY in Physics.

Department of Physics

Dissertation Advisor:	*Dr. Claudio Mazzoleni*
Committee Member:	*Dr. Jacek Borysow*
Committee Member:	*Dr. Will Cantrell*
Committee Member:	*Dr. Simon Carn*
Department Chair:	*Dr. Ravindra Pandey*

Table of Contents

List of Figures

List of Tables

Author Contribution Statement

Chapter 2 is related to, but not entirely based on, a paper recently published in the journal Aerosol Science and Technology (AS&T). Chapter 3 contains work from an unpublished paper that is currently a work in progress and shares some data from the paper published in AS&T. Further revisions are anticipated for each of these chapters based on feedback from co-authors and reviewers.

Chapter 2 is based on experiments I performed at Los Alamos National Lab (LANL) as part of the U.S. Department of Energy (DOE) Office of Science Graduate Student Research (SCGSR) program. Some of the datasets in Chapter 2 are the same as used in a paper published to the AS&T; however, they are presented in a different manner. Chapter 2 focuses on aspects of characterization not covered in the paper and goes into greater detail in describing the size-dependent truncation biases. I wrote the truncation correction software described in this Chapter 2 and performed all the experiments and analysis for the data presented. A small technical note introducing the software and describing the truncation corrections may be published to AS&T in the future.

Chapter 3 is based on more experiments performed at LANL as part of the SCGSR program. Some of the data presented in this chapter was published in the AS&T paper mentioned previously; however, it is presented and used differently. I performed all the experiments and analysis for the paper, and the code for determining the refractive index was written by collaborator and eventual coauthor, Kyle Gorkowski.

Chapter 4 was published in the journal *Remote Sensing* and is republished in its entirety as a chapter in this dissertation. Data collection was performed by Dr. Claudio Mazzoleni and Dr. Jacek Borysow. I performed all analysis with significant input from my co-authors: Dr. Jacek Borysow, Dr. Claudio Mazzoleni, and Dr. Massimo Moraldi. I wrote most of the paper with significant contributions and feedback from each of the co-authors.

While this dissertation covers a significant portion of my graduate work at Michigan Technological University (MTU), it does not cover the full extent of my efforts and contributions to science. I have been involved in the development of several instruments in the Environmental Optics Laboratory, including a broadband cavity enhanced extinction spectrometer (BD-CEES), a tunable diode laser absorption hygrometer (H-TDLAS), four-wavelength photoacoustic spectrometer (PAS-4), an acoustic levitator, as well as a couple standalone, single wavelength, photoacoustic instruments. Many of these instruments will play a critical role measurement performed by EOL for years to come. The BB-CEES's description and characterization was published in AS&T in 2020. I was largely involved with some of the experiments characterizing the instrument, and the Allan deviation calculations were performed using software I had written in Python for the photoacoustic instrumentation. Before the pandemic, we had begun performing experiments using the BD-CEES and photoacoustic instrument to study the optical properties and physical properties of various wood smokes used in flavoring food. The results of photoacoustic measurements of cherry wood indicated high brown carbon production.

In July of 2017, I participated in the ACTRIS-2 field campaign. My role was to deploy one of our single wavelength photoacoustic instruments to a remote observation site atop Monte Cimone and to collect samples for microscopy analysis. The photoacoustic was not sensitive enough to measure low signal at Monte Cimone, an issue tied to having to replace its original laser with a laser of lower power a few days into the campaign. This photoacoustic will eventually be deployed to the more polluted Bologna, which is located in the heavily polluted Po Valley region. I presented preliminary results of the microscopy analysis at the 10th International Aerosol Conference in St. Louis, MO. One of the samples collected contained a high fraction of tar ball aggregates (~15%), an aerosol commonly found in biomass burning and typically observed as individual spheres. Results from this sample were published as part of a wider study into tar ball aggregates by Guilia Girotto in Environmental Science and Technology. In addition, a manuscript, which I will be co-author on, is currently being prepared by Dr. Swarup

China at Pacific Northwest National Laboratory looking into the chemistry of the microscopy samples collected at Monte Cimone.

While working at the Center for Aerosol Forensic Experiments (CAFE) at Los Alamos National Lab, I assembled an inverted soot generator that is currently being used for experiments. I also wrote the standard operating procedures and helped with safety documentation for the soot generator. I performed a few experiments looking at the hygroscopic properties of soot produced by the inverted burner using the H-CAPS-PM_{SSA}. While hygroscopicity did not change, we found a significant increase in the SSA of soot exposed to UV light. The truncation code and empirical corrections described in Chapter 2 are also being used by the CAFÉ team to truncation related uncertainties for all work being performed using the H-CAPS-PM_{SSA}. A manuscript (of which I will be co-author) is currently being prepared looking at water uptake on brown carbon surrogates.

Acknowledgements

I would like to express my appreciation and gratitude to my advisor, Dr. Claudio Mazzoleni. Dr. Mazzoleni has always been my biggest advocate by encouraging me to pursue every opportunity and providing me with the mentorship I needed to be successful as a graduate student. I am grateful to have had the opportunity to work with Dr. Mazzoleni and do research with the Environmental Optics Lab (EOL) group.

I would like to thank my committee: Dr. Jacek Borysow, Dr. Will Cantrell, and Dr. Simon Carn. Thank you all for the valuable feedback regarding my research and dissertation.

I am grateful to the Physics Department at Michigan Tech for taking a chance on me back in Fall 2014, the Elizabeth and Richard Henes Center for Quantum Phenomena for providing support for travel to conferences (as well as research fellowships to help continue my studies), and the DeVleig foundation for supporting me with a fellowship during the Summer of 2017. I would also like to thank the U.S. Department of Energy's Office of Science for providing me the opportunity to work at Los Alamos National Lab during the Fall of 2018.

I would like to thank my research group and other collaborators for thoughtful discussions during our group meetings. This includes Dr. Swarup China, Dr. Janarjan Bhandari, Dr. Noopur Sharma, who helped me in my early years by providing constructive criticism and sharing their research with me during so many Friday group meetings. Thanks to Shreya Joshi, Susan Mathai, Megan Morgenstern, Eduardo Rodriguez-Feo, and Aiswarya Mundakkal for always asking interesting questions and keeping me on my toes during group discussions. I enjoyed working with each of you, even if it seems I was frustrated (let us be honest, it was the equipment's fault). Thanks to Kendra Wright for introducing me to the photoacoustic spectrometers. I am sorry your laser broke. Thanks to Dr. Ravi Varma, Dr. Dennis van der Voort, and Dr. Massimo Moraldi for the research related discussions and collaboration. Thanks to the myriad of

undergraduates who provided me the opportunity to be a mentor, the research progress you mad, and participating in group discussions. This includes Kaelan Anderson, Renato Pinto, Illiya Chibirev, Novia Berriel, Reed Downs, Keegan Downham, and Wyatt Perry.

I want to express my gratitude to everyone I worked with at LANL's Center for Aerosol Forensic Experiments. Special thanks to Dr. Manvendra Dubey for helping me prepare my SCGSR application and always providing me with ideas to further my research. I would also like to thank Jared Lam for showing me how to use the H-CAPS-PM_{SSA}, Dr. Christian Carrico for helping me modify the H-CAPS-PM_{SSA} and for supporting my efforts, and Dr. James Lee for helping conduct experiments in the CAFÉ lab. I want to thank Dr. Kyle Gorkowski for providing me with his grid search code for refractive indices. In addition, I would like to thank Dr. Allison Aiken and Dr. Petr Chylek for their help and feedback on my work. To Dr. Tim Onasch and Dr. Andrew Freedman at Aerodyne Inc., I would like to thank for your discussions regarding the H-CAPS-$PM_{SSA.}$ I would also like to thank Dr. Carl Necker, Dr. Julie Bremser, Dr. Phil Tubesing, Jeremy Bremser, and Blythe Bremser for providing me with a roof over my head and being my family away from home.

Thanks to my friends, who helped to keep me sane during graduate school. I am glad I found a group of people I could share my struggles with, but also enjoy a game of broomball, softball, frisbee golf, or even some potent potables. Special thanks to Chad Brisbois, Lisa Eggart, Jesse & Natalie Anderson, Teresa Wilson, Abu Shawon, Jeff Kabel, Kevin Waters, Joseph Niehaus, Scott & Stephanie Rutterbush, Subin Thomas, Andrew & Huyen Puyleart, Prasanth Prabhakaran, and Greg Kinney. Special, heartfelt thanks to my oldest friends, Codey Hatfield, Michael Wojcik, and Kristin Klimeck, whose friendship I will always cherish.

Thanks to my family, for being so understanding and supportive of me. I know that I can be distant at times and I will try to do better by you in the future. Despite this, your support has been unwavering and has helped me through some dark times. Thank you to my mother, Dianna Nichols – thanks always working so hard and for always making me

smile. To my father, Scott Capek, thanks for your strength, determination, and perseverance. I am as proud of you as you are of me. To my stepmother, Sharon Capek: You are one of the most generous and thoughtful people I know. To all my siblings, Danielle Small, Elisha Capek, Michael Seng, Bo Seng, Samantha Seng, and Chandel Lamberty. And to my extended family, too vast for even this dissertation. To my grandfather, Leonard Nichols, the hardest working man I know. To my grandmothers Minnie Nichols and Betty Capek, who played a big role in my upbringing but are no longer with us.

Lastly, and most importantly, I want to thank my wife. You are my rock, my editor-in-chief, and my best friend. Thank you for sacrificing so much to help me realize my dreams. None of this would be possible without your support, and I am sorry you had to endure so many UP winters.

List of Abbreviations

The following abbreviations are used in this dissertation:

AAE	Absorption Ångström Exponent
CCN	Cloud Condensation Nuclei
CPC	Condensation particle counter
CPMA	Centrifugal Particle Mass Analyzer
CRD	Cavity Ring Down Spectrometer
DMA	Dynamic Mobility Analyzer
EAE	Extinction Ångström Exponent
EC:OC	Elemental carbon to organic carbon
EMS	Extinction Minus Scattering
H-CAPS-PMSSA	Humidified Cavity Attenuated Phase Shift Albedometer
HEPA	High Efficiency Particulate Air
HRM	Highly reflective mirror
LED	Light emitting diode
LiDAR	Light Detection and Ranging
OCM	Organic carbon mass
PD	Photodiode
PID	proportional-integral-derivative
PMT	Photomultiplier Tube
PRR	Pure-rotational Raman
PSAP	Particle Soot Absorption Photometer
RH	Relative Humidity
RH&T	Relative Humidity and Temperature
SAE	Scattering Ångström Exponent
SMPS	Scanning mobility particle sizer
SSA	Single scattering albedo
TLDR	Two-line different branch ratio
TLSR	Two-line same branch ratio
VRR	Vibrational-rotational Raman

Abstract

Aerosol and water are inexorably linked, and both are ubiquitous within our atmosphere and required components for cloud formation. Relative humidity (RH), a temperature dependent quantity, can have a significant influence on the size, shape, and ultimately, the optical properties of the aerosol. RH can vary substantially on small spatial and short temporal scales in turbulent conditions due to rapid fluctuations in temperature and water vapor mixing ratio. Accurate assessment of optical enhancements due to an increase in RH is key for determining the particles' impact on the climate and visibility.

A humidity-controlled cavity attenuated phase-shift albedometer (H-CAPS-PM_{SSA}) was designed and characterized to measure the humidity response of aerosol extinction and scattering. Size-dependent truncation, a significant source of systematic bias within the H-CAPS-PM_{SSA}, was characterized and a correction scheme developed. The H-CAPS-PM_{SSA} was then used to determine the optical and hygroscopic properties of ammonium sulfate, nigrosin, and two mixtures of ammonium sulfate and nigrosin. It was determined that enhancements in single scattering albedo of these aerosol because of humidification could be approximated using a quadratic function with a single fitting parameter related to the hygroscopicity of the two species in the mixture.

To determine RH in a turbulent environment, non-invasive temperature measurements are necessary. Temperature can be inferred from vibro-rotational Raman (VRR) scattering. Several methods of extracting temperature from the VRR spectra of N_2 and O_2 were investigated. It has been shown that the non-rigidity of N_2 and O_2 must be considered for accurate temperature measurement and that methods involving more VRR lines, and therefore greater photon statistics, had the greatest precision and self-consistency. It was also found that separation between the lines was an important consideration for temperature measurement precision.

1 Introduction

Particulate matter that is suspended in the atmosphere have important implications for human health, the hydrological cycle, visibility, and Earth's radiative balance. These particles suspensions, typically referred to as aerosol, can be liquid or solid and can be produced naturally or by anthropogenic activities. The properties of these aerosol can be affected by the temperature as well as the water is available in the atmosphere. This dissertation uses novel measurements to understand how the optical properties of aerosol can be affected by temperature and water vapor.

1.1 Motivation

Aerosol interact with light by first either redirecting the light or scattering it and then by absorbing the light's electromagnetic energy and mostly converting it to thermal energy. The contributions of scattering and absorption are additive to the total extinction of radiation. Extinction, scattering, and absorption are typically expressed either as a linear attenuation coefficient, B, with units of inverse distance (Mm^{-1}) or as a cross-section, σ, with units of area (μm^2). By scattering or absorbing light, aerosol can prevent the amount of light from that reaching Earth's surface. By scattering or absorbing light, aerosol reduce the amount of light that reaches earth's surface. As a result, aerosol directly impact Earth's radiative budget, leading to a net instantaneous cooling effect at the surface (Yu et al. 2006). However, strongly absorbing aerosol can lead to localized heating, affecting the temperature and relative humidity (RH) of the surrounding environment. Often, the brightness of an aerosol is quantified as the ratio of the total scattered light to total extinction. This is referred to as the aerosol single scattering albedo (SSA), a key parameter for estimating the net cooling or warming aerosol can have on the atmosphere (Chylek and Wong 1995).

In addition to the aerosol direct effect mentioned in the previous paragraph, aerosol can indirectly influence earth's radiative budget by acting as condensation nuclei for cloud droplets. The ways in which aerosol can affect the optical properties of clouds is referred

to as the aerosol indirect effect (Lohmann and Feichter 2005). Aerosol act as cloud condensation nuclei and therefore play a significant role in cloud formation and precipitation. Clouds cover 70% of the earth, and aerosol has a considerable effect in determining their net warming or cooling through the aerosol indirect effect (Stubenrauch et al. 2010) (Boucher et al. 2013). Aerosol can also initiate ice formation in clouds, which increase the chances of a cloud precipitating. Wu and Lau estimated that 69% of precipitation originates as ice in clouds (Lau and Wu 2003).

There exists a third effect in which aerosol can influence earth's radiative budget referred to as the aerosol semi-direct effect. The semi-direct effect is the process by which aerosol affect cloud formation by altering the localized air temperature through light absorption (Ackerman et al. 2000). The degree to which these three effects occur is often dictated by atmospheric state variables such as temperature and the concentration of water vapor present. Therefore, aerosol themselves can have an impact on atmospheric state variables as well. The relation between aerosol properties and atmospheric state variables are not well understood due to the difficulty of effectively measuring them. Reducing uncertainties associated with aerosol radiative forcing has proven to be one of the biggest challenges in climate science. The current upper and lower bounds for effective radiative forcing stand at -0.35 and -2.0 Wm^{-2} respectively, a modest reduction in comparison to the 2013 IPCC uncertainty range of -0.1 and -1.9 Wm^{-2} (Bellouin et al. 2020). The challenge results from the difficulty of "simultaneously constraining aerosols, clouds, and radiation state variables as well as the relationships between them so as to constrain uncertainty in the change of state on multiple timescales" (Regayre et al. 2018). Regayre et al. estimate that uncertainty is largely dominated by aerosol-related parameters; however, atmospheric state variables still account for about 30% of this uncertainty (Regayre et al. 2018).

Aerosols are often composed in part by water, and increases in water content can lead to enhancements in the optical properties of the aerosol, which is of particular interest for the aerosol direct effect (Baynard et al. 2006; D. Liu et al. 2013). Increased water content

will result in larger aerosol size, which results in a larger scattering cross-section (I. N. Tang 1996). Water can also act in a similar fashion to a lens, focusing light down onto light-absorbing species encapsulated by the water. Mikhailov et al. showed that at RH near 100%, three-fold increases in aerosol absorption could be achieved for soot (Mikhailov et al. 2006). The addition of water to aerosol will also cause the aerosol to become heavier, resulting in shorter lifetimes in the atmosphere (Roelofs 2013).

This dissertation is being written in what is hopefully the tail end of the SARS-COVID-19 pandemic. The relationship between aerosol lifetimes and water vapor has gained renewed discussion through the lens of viral transmissivity (Asadi et al. 2020). Studies linking the transmissivity of COVID-19 have to date been largely inconclusive (Luo et al. 2020), though similar viruses have shown greater survivability at RH less than 50% (J. W. Tang et al. 2006).

1.1.1 Aerosol, Relative Humidity, and Temperature

The amount of water hygroscopic aerosol is dependent on the relative humidity (RH) of the atmosphere. Relative humidity is defined as ratio of the partial pressure of water vapor (p_v) to the saturation vapor pressure of water (p_s). The saturation vapor pressure of water is dependent on the temperature according to the Magnus formulation of the Clausius-Clapyron equation (Alduchov and Eskridge 1997; H.R. Pruppacher 1997):

$$p_s(T) = 6.1094e^{17.625T/234.04-T} \qquad \text{Equation 1.1}$$

where T is atmospheric temperature in Kelvin. In this formulation, the vapor pressure is expressed in units of hPa. The hygroscopicity of an aerosol is dependent on its composition. In the presence of solute containing aerosol, the equilibrium vapor pressure over a plane surface of a solution is reduced due to the Raoult effect. This allows for the exchange of water molecules between solute containing aerosol and the atmosphere even when the humidity less than 100%. Aerosol containing freshly emitted soot or mineral dust tend to be hydrophobic and therefore will not exchange water easily (Weingartner et

al. 1997; Carrico et al. 2003). On the other hand, aerosol such as inorganic salts or water-soluble organics tend to readily adsorb water even when the relative humidity is below saturation ($RH \div 100 = p_v/p_s < 1.0$) (Chan et al. 2005; Xu and Penner 2012). Many inorganic salts will not uptake water until a particular RH is reached, a phenomenon known as deliquescence. The water in a hydrated inorganic salt will suddenly evaporate if the RH gets too low, which is known as efflorescence. Because the RH that an aerosol effloresces at is lower than when it deliquesces, most salts exhibit a water uptake hysteresis loop. It is therefore important to know the history of aerosol with respect to RH exposure to predict how its water content will change with RH.

The scattering and absorption cross-section of an aerosol at a given wavelength is dependent upon the refractive index, the size, and the shape of the aerosol. When water is added to an aerosol, each of these properties can change. This can lead to substantial changes in an aerosol's optical properties. For atmospherically relevant inorganic salts such as sodium chloride and ammonium sulfate, the addition of water can lead to large enhancements in light scattering (I. N. Tang 1996). In the case of soot, aging and mixing with more hydrophilic aerosol can cause it to become more hydrophilic. Because soot is not soluble, water will form a coating around the soot. The water coating should enhance the scattering and absorption through particle size growth and lensing effect. While scattering enhancements have been confirmed, field studies and experiments have shown mixed results for absorption. Laboratory measurements have shown absorption enhancements as high 3 for black carbon and other light-absorbing organics (Mikhailov et al. 2006; Brem et al. 2012). However, Lack et al. observed absorption enhancements from biomass burning that was between 1.2 and 1.6 (Lack et al. 2012) while Liu found absorption enhancements of 1.5 in winter time measurements of black carbon(S. Liu et al. 2015). In contrast to this, Cappa et al. found absorption enhancements of urban black carbon aerosol of only 1.06 (Cappa et al. 2012) while Healy et al found no enhancement for black carbon at 781nm for biomass burning aerosol (Healy et al. 2015). This last study did however find large absorption enhancements for (>2) for brown carbon at 450nm. These studies suggest that absorption enhancements are more variable than those

predicted in climate models for absorbing aerosol with organic coatings (Cappa et al. 2019). Experiments focused on absorption enhancements due to water coatings are limited due to the difficulty of measuring absorption in the presence of liquid water. Therefore, an instrument capable of detecting small changes in absorption in the presence of water is necessary to fully determine climatic impact of interactions between water and absorbing aerosol.

Explanations for reduced absorption enhancements are typically morphological. Enhancements can be high if water forms a shell around the absorbing particle to cause lensing-based enhancement (Jacobson 2001). Modeling performed by Jacobson's study showed significant enhancements in absorption coefficient, especially in high humidity environments for internally mixed aerosols (i.e. a mixture of species in a single particle) as compared to externally mixed aerosols (i.e. different species in different particles). However, one source of uncertainty in this study is that it assumes a middle ground value for the density of the soot particles that may not accurately predict the optical properties of heavily aged, more compact soot particles (Jacobson 2012). Cappa et al. surmised that absorption enhancements could be suppressed by black carbon being closer to the edge of the aerosol, thus mitigating the lensing effect (Cappa et al. 2012). Another explanation for reduced absorption enhancements is that coatings can also lead to the compaction of soot, which are shaped like lacy chains when freshly emitted. Such compaction processes are expected to lead to a modest and wavelength-dependent change in absorption for soot but a larger change in scattering (China et al. 2015). As a result, there are two competing processes occurring within these aerosols.

In the atmosphere, temperature and water vapor concentration are constantly fluctuating, an effect that can be enhanced by turbulence. Kulmala et al. shows that the average saturation ratio and the variability of the saturation variable are dependent on the average temperature, the water vapor pressure, and the covariance of these two quantities, $\overline{p'_v T'}$ (Kulmala et al. 1997):

$$\overline{p'_v T'} = C_{p'_v,T}\sigma_{p_v}\sigma_T \qquad \text{Equation 1.2}$$

where p'_v and T' are fluctuation terms of water vapor pressure and temperature respectively, $C_{Pv,T}$ is a coupling coefficient for the two quantities, and σ_{Pv} and σ_T are the standard deviations of water vapor pressure and temperature. Because the size and, by extension, optical properties of many atmospheric aerosol are dependent on relative humidity, turbulence fluctuations in relative humidity are directly relevant to the aerosol direct effect.

1.1.2 Measurements of Aerosol Optical Properties

Direct measurements of an aerosol's properties are typically done using in situ instrumentation. Such instruments allow for accurate measurements of intensive parameters in a well characterized environment. The most common approach to determining the hygroscopic properties of aerosol has been the use of Humidified Tandem Differential Mobility Analyzers (H-TDMA) (Swietlicki et al. 2008). These instruments measure the change in electric mobility diameter of aerosol. Since the technique measures changes in size, optical properties must be inferred using Mie calculations or empirical data. Nephelometry, a technique for measuring integrated light scattering, has successfully been coupled with humidification systems to determine the scattering response of aerosol to high humidity (Gomez et al. 2018).

Despite the global impact that changes in SSA due to water uptake by light-absorbing aerosol might have, the measurement of these effects is still challenging. Absorption is typically measured using one of three different methods: attenuation of light by aerosol deposited on filters, photoacoustic spectroscopy, or difference between extinction and scattering. Filter based methods are prone to several biases because the morphology of individual particles is disturbed at deposition and the method performs erratically at medium-high RH (Arnott et al. 2003). Some studies using humidified nephelometers to estimate light scattering have measured absorption using filter-based methods at low RH

but then assume no change in absorption occurs at high RH to estimate SSA (Nessler et al. 2005; Fierz-Schmidhauser et al. 2010). However, absorption is an RH dependent parameter, and the absorption measurement is performed on a volume of aerosol that differs from the scattering measurement volume.

Photoacoustic instruments with integrated nephelometers can provide accurate measurements of SSA. An advantage of this method is that the scattering and absorption measurements are performed on the same volume; however, the performance of photoacoustic measurements degrades when RH>65% (Arnott et al. 2003 ; Langridge et al. 2013). In extinction minus scattering (EMS) methods, scattering and extinction are measured separately. Typically, scattering is measured using an integrating nephelometer, and extinction is measured using a cavity-enhanced technique such as a cavity ring down spectrometer (CRDS). Recently, instrumentation capable of measuring extinction and scattering on the same sample volume have been developed, reducing the uncertainty involved with measurements on separate volumes and allowing for accurate measurement of SSA (Onasch et al. 2015). Instruments capable of performing the EMS method to determine the RH dependency of aerosol SSA have also been recently developed (Zhou et al. 2020; Carrico et al. 2021). Such instrumentation will be critical for determining optical parameterizations for aerosol containing light-absorbing materials and should help to better reduce uncertainties involving light-absorbing aerosol.

1.1.3 Remote Measurement

Instruments that perform in situ aerosol measurements are a powerful tool for understanding their properties. However, in the atmosphere, fluctuations occur over faster time scales and smaller spatial scales that cannot be probed by many instruments. Most instruments require averaging times of a minute or longer to achieve sensitivity capable of measuring atmospheric aerosol with a high degree of precision. In addition, the sampling volumes of these instruments are often larger than the volumes in which small scale fluctuations occur. Furthermore, these instruments are generally only able to sample the aerosol in a single location, such as a sampling port. This means that the sample is

extracted from its environment, potentially changing the atmospheric state of the sample and losing important information as a result. Therefore, the effects of localized fluctuations operating on small time scales on an ensemble of aerosol is lost. One such instance is the effects of humidity fluctuations on aerosol properties. Processes such as deliquescence can lead to significant growth in aerosol over a very small range of RH values. Fluctuations in RH that push small, localized regions beyond an aerosol's deliquescence point could lead to significant growth in aerosol, even if the average RH (or supersaturation) is too low for ensemble deliquescence to occur.

It would therefore be advantageous to generate a map of the humidity field and the light scattering within a test volume, such as inside the Michigan Tech Cloud Chamber (Chang et al. 2016). The Michigan Tech Cloud Chamber, also known as the Π-Chamber, can produce clouds through turbulent mixing via Rayleigh-Benard convection. The Π-Chamber can also be operated in a subsaturated mode, allowing for measurements of cloud-free atmospheric state on aerosol in a turbulent environment. Measurements from within the Π-Chamber are made by sampling the chamber using external instrumentation or by immersing sensors within the cloud volume. One example of the latter is a thermistor array for the measurement of the spatial temperature profiles within the cloud chamber. These thermistors could disrupt the flow within the chamber, making it difficult to clearly detect turbulence-induced processes. Extraction of the samples from inside of chamber using external instruments can alter the humidity and temperature of the sample, due to a temperature difference between the instruments and the sample. This temperature difference could influence the measurement of important variables, such as aerosol size. Remote, non-invasive measurements avoid such issues and allow for measurement of important parameters without internal or external influence.

To perform remote measurements that explore the role turbulence plays on the optical properties of aerosol, three simultaneous measurements are necessary: temperature, water vapor, and elastic scattering intensity. The first two measurements are for determining the RH field within the chamber as Equation 1.1, while the third measurement is for

determining the optical response of aerosol and cloud droplets to these changes. Of these measurements, remote temperature measurement is the most challenging. There are several methods available for the remote measurement of temperature; however, pure rotational Raman (PRR) has largely become the method of choice in atmospheric LiDAR applications (Wulfmeyer et al. 2015). The intensity of lines within the PRR spectrum depend on the temperature according to the Maxwell-Boltzmann distribution. This method is performed by isolating two sections of the PRR spectrum using optical bandpass filters and taking a ratio of the two transmitted signals (Behrendt et al. 2002). An issue with PRR measurement is that it is spectrally close to the elastic scattering, which results in light leakage through the bandpass filters. This is especially true in a volume such as the Π-Chamber, which will be filled with particles that are elastically scattering. Light leakage is dependent on spectral proximity of the elastically scattered line to the filter transmission wavelength window, as well as the angle of incidence of light with respect to the band-pass filter. In LiDAR, angularly dependent leakage is mitigated somewhat by having extremely limited fields of view (typically 0.75 mrad or less) which forces light to have near normal incidence with the filters (Radlach et al. 2008). However, a remote measurement system within the cloud chamber will not have this advantage, as we anticipate fields of view greater than 30 mrad may be necessary to image a section of the Π-Chamber large enough to see spatial variations in temperature. As a result, we choose to focus on the vibro-rotational Raman (VRR) spectrum of N_2 and O_2, which is spectrally distant from elastic scattering. The VRR spectrum's temperature dependence is like that of the PRR spectrum; however, the intensity is two orders of magnitude lower. As a result, research examining the efficacy of deriving temperature from the VRR spectra of N_2 and O_2 is somewhat limited. This dissertation will show experiments and analyses used to infer temperature from the VRR spectrum and how we used our results to quantify the best methods to apply for the study of aerosol response to temperature fluctuations in a turbulent medium.

To non-invasively estimate relative humidity within the cloud chamber, the water vapor mixing ratio needs to be measured in tandem with temperature. This measurement should

be performed by taking a ratio of the fundamental vibrational Raman transitions for water vapor and nitrogen, which is well mixed and has a constant number concentration in the atmosphere (Cooney 1970). Like the VRR spectra, the fundamental vibrational lines are spectrally distant from elastic scattering and therefore less prone to leakage. The water vapor measurement was demonstrated in lab by Chibirev et al., who found that the system described in Chapter 4 of this paper could achieve mixing ratio sensitivity of 3.3×10^{-7} kg/kg (Chibirev et al. 2018). For standard atmospheric conditions, this is good enough for RH measurements to be made with precisions as good as 0.002%. The measurement of RH is therefore limited to the sensitivity of the temperature measurement. The sensitivity of the water vapor measurement is related to sum of the inverse roots of the number of photons collected from the nitrogen and water vapor vibrational lines. Assuming the photons detected are linear with laser power, the current setup should provide an order of magnitude better sensitivity in water vapor detection.

1.2 Research Objectives

The objective of this dissertation is to understand how temperature and water vapor affect the optical properties of aerosol. Novel measurement methods were implemented to investigate how temperature and water vapor play a role in altering the optical properties of aerosol. This dissertation will center around the following research topics:

a) Describing and characterizing the humidified cavity attenuated phase shift albedometer (H-CAPS-PM_{SSA}) system developed at the Los Alamos National Laboratory.
b) Quantifying and parameterizing size-dependent light scattering truncation biases in the H-CAPS-PM_{SSA}. A software package for predicting truncation is described, and empirical relationships between Mie theory, aerosol diameter, and truncation are derived.
c) Discussing an optical study on ammonium sulfate and nigrosin, as well as mixtures of the two. From this we determined the following:

i. Refractive indices of nigrosin and the ammonium sulfate nigrosin mixtures.
ii. Hygroscopic properties of each aerosol species.
iii. Enhancements in single scattering albedo and absorption
iv. Parameterization of the single scattering albedo as a function of nigrosin volume fraction.
v. Parameterization of absorption enhancements as a function of scattering enhancement.

d) Non-invasive temperature measurement using the vibro-rotational spectrum of O_2 and N_2. Three expressions for temperature are derived and compared:
   i. Two-line ratios: ratio of any two lines in the VRR spectrum of O_2 and N_2
   ii. Linear regression of VRR line intensities from the same branch
   iii. Ratios of two sections of the VRR spectrum, each containing multiple lines and increased line intensity.

1.3 Dissertation Overview

This section provides a brief description of the structure of the dissertation and how the chapters are organized. The chapters are of the dissertation are as follows:

Chapter 1 is the introduction.

Chapter 2 provides an overview of H-CAPS-PM_{SSA}. This instrument can measure extinction and scattering as a function of relative humidity. Experiments were performed at Los Alamos National Laboratory as part of the DOE Office of Science Graduate Student Research Program to characterize the instrument, with particular focus on size-dependent light scattering truncation biases. Experimentally measured biases are compared to Lorenz-Mie calculations, and empirical corrections are derived. These corrections are then compared to truncation values measured from humidified ammonium sulfate. It is then determined that the empirical correction based on aerosol diameter works best for humidified aerosol. This correction scheme is used in Chapter 3.

Chapter 3 covers experiments that were performed on ammonium sulfate and nigrosin, as well as two mixtures of these substances, using the H-CAPS-PM_{SSA} at Los Alamos National Laboratory in the Fall of 2018 and 2019. Experiments were performed to determine the refractive indices of nigrosin as well as of two mixtures of ammonium sulfate and nigrosin at different molar fractions. We report the hygroscopic properties of these mixtures and compare them to volume mixing rules. Then, enhancements in single scattering albedo and absorption were parameterized based on the volume fraction of nigrosin and scattering enhancement, respectively. These or similar parameterizations could be used in climate models to better estimate light absorption of mixtures.

Chapter 4 covers experiments and analyses looking at noninvasively inferring temperature from the VRR spectra of N_2 and O_2 using a multi-pass cell and high-power CW laser. Several expressions are derived and applied to the measured VRR spectrum. These methods are then compared to each other using statistical methods. We determine which methods are the most self-consistent and achieve the highest precision, and which regions of the spectra are the most suitable for accurately and precisely measuring temperature.

Chapter 5 summarizes the work and results from the previous chapters. The implications of the results are discussed, and future directions and potential studies are proposed. These future research activities should allow for a better understanding of the role water vapor and temperature play in affecting the optical properties of aerosol also in the presence of small spatial and temporal temperature and water vapor mixing ratio fluctuations due to atmospheric turbulence.

1.4 References

Ackerman AS, Toon OB, Stevens DE, Heymsfield AJ, Ramanathan V, Welton EJ. 2000. Reduction of Tropical Cloudiness by Soot. Science 288(5468):1042-1047.

Alduchov OA, Eskridge RE. 1997. Improved Magnus` form approximation of saturation vapor pressure. ; Department of Commerce, Asheville, NC (United States). No. DOE/ER/61011-T6; Other: ON: DE98001239; TRN: 97:005834 United States

10.2172/548871 Other: ON: DE98001239; TRN: 97:005834 OSTI as DE98001239 ORO English.

Arnott WP, Moosmuller H, Sheridan PJ, Ogren JA, Raspet R, Slaton WV, Hand JL, Kreidenweis SM, Collett JL. 2003. Photoacoustic and filter-based ambient aerosol light absorption measurements: Instrument comparisons and the role of relative humidity. Journal of Geophysical Research-Atmospheres 108(D1).

Asadi S, Bouvier N, Wexler AS, Ristenpart WD. 2020. The coronavirus pandemic and aerosols: Does COVID-19 transmit via expiratory particles? Aerosol Science and Technology 54(6):635-638.

Baynard T, Garland RM, Ravishankara AR, Tolbert MA, Lovejoy ER. 2006. Key factors influencing the relative humidity dependence of aerosol light scattering. Geophysical Research Letters 33(6).

Behrendt A, Nakamura T, Onishi M, Baumgart R, Tsuda T. 2002. Combined Raman lidar for the measurement of atmospheric temperature, water vapor, particle extinction coefficient, and particle backscatter coefficient. Applied Optics 41(36):7657-7666.

Bellouin N, Quaas J, Gryspeerdt E, Kinne S, Stier P, Watson-Parris D, Boucher O, Carslaw KS, Christensen M, Daniau AL et al. . 2020. Bounding Global Aerosol Radiative Forcing of Climate Change. Reviews of Geophysics 58(1).

Boucher O, Randall D, Artaxo P, Bretherton C, Feingold G, Forster P, Kerminen V-M, Kondo Y, Liao H, Lohmann U et al. . 2013. Clouds and Aerosols. In: Stocker TF, Qin D, Plattner G-K, Tignor M, Allen SK, Boschung J, Nauels A, Xia Y, Bex V, Midgley PM, editors. Climate Change 2013: The Physical Science Basis. Contribution of Working Group I to the Fifth Assessment Report of the Intergovernmental Panel on Climate Change. Cambridge, United Kingdom and New York, NY, USA: Cambridge University Press. p. 571–658.

Brem BT, Gonzalez FCM, Meyers SR, Bond TC, Rood MJ. 2012. Laboratory-Measured Optical Properties of Inorganic and Organic Aerosols at Relative Humidities up to 95%. Aerosol Science and Technology 46(2):178-190.

Cappa CD, Onasch TB, Massoli P, Worsnop DR, Bates TS, Cross ES, Davidovits P, Hakala J, Hayden KL, Jobson BT et al. . 2012. Radiative Absorption Enhancements Due to the Mixing State of Atmospheric Black Carbon. Science 337(6098):1078-1081.

Cappa CD, Zhang XL, Russell LM, Collier S, Lee AKY, Chen CL, Betha R, Chen SJ, Liu J, Price DJ et al. . 2019. Light Absorption by Ambient Black and Brown Carbon and its Dependence on Black Carbon Coating State for Two California, USA, Cities in Winter and Summer. Journal of Geophysical Research-Atmospheres 124(3):1550-1577.

Carrico CM, Kus P, Rood MJ, Quinn PK, Bates TS. 2003. Mixtures of pollution, dust, sea salt, and volcanic aerosol during ACE-Asia: Radiative properties as a function of relative humidity. Journal of Geophysical Research-Atmospheres 108(D23):18.

Carrico CM, Capek TJ, Gorkowski KJ, Lam JT, Gulick S, Karacaoglu J, Lee JE, Dungan C, Aiken AC, Onasch TB et al. . 2021. Humidified Single Scattering Albedometer (H-CAPS-PMSSA): Design, Data-Analysis, and Validation. Aerosol Science and Technology:1-25.

Chan MN, Choi MY, Ng NL, Chan CK. 2005. Hygroscopicity of Water-Soluble Organic Compounds in Atmospheric Aerosols: Amino Acids and Biomass Burning Derived Organic Species. Environmental Science & Technology 39(6):1555-1562.

Chang K, Bench J, Brege M, Cantrell W, Chandrakar K, Ciochetto D, Mazzoleni C, Mazzoleni LR, Niedermeier D, Shaw RA. 2016. A Laboratory Facility to Study Gas-Aerosol-Cloud Interactions in a Turbulent Environment: The Pi Chamber. Bulletin of the American Meteorological Society.

Chibirev I, Mazzoleni C, van der Voort DD, Borysow J, Fink M. 2018. Raman spectrometer for field determination of H2O in natural gas pipelines. Journal of Natural Gas Science and Engineering 55:426-430.

China S, Scarnato B, Owen RC, Zhang B, Ampadu MT, Kumar S, Dzepina K, Dziobak MP, Fialho P, Perlinger JA et al. . 2015. Morphology and mixing state of aged soot particles at a remote marine free troposphere site: Implications for optical properties. Geophysical Research Letters 42(4):1243-1250.

Chylek P, Wong J. 1995. Effect of absorbing aerosols on global radiation budget. Geophysical Research Letters 22(8):929-931.

Cooney J. 1970. Remote Measurements of Atmospheric Water Vapor Profiles Using the Raman Component of Laser Backscatter. Journal of Applied Meteorology and Climatology 9(1):182-184.

Fierz-Schmidhauser R, Zieger P, Gysel M, Kammermann L, DeCarlo PF, Baltensperger U, Weingartner E. 2010. Measured and predicted aerosol light scattering enhancement factors at the high alpine site Jungfraujoch. Atmospheric Chemistry and Physics 10(5):2319-2333.

Gomez SL, Carrico CM, Allen C, Lam J, Dabli S, Sullivan AP, Aiken AC, Rahn T, Romonosky D, Chylek P et al. . 2018. Southwestern US Biomass Burning Smoke Hygroscopicity: The Role of Plant Phenology, Chemical Composition, and Combustion Properties. Journal of Geophysical Research-Atmospheres 123(10):5416-5432.

H.R. Pruppacher JDK. 1997. Microphysics of Clouds and Precipitation. Dordrecth, The Netherlands: Kluwer Academic Publishers.

Healy RM, Wang JM, Jeong CH, Lee AKY, Willis MD, Jaroudi E, Zimmerman N, Hilker N, Murphy M, Eckhardt S et al. . 2015. Light-absorbing properties of ambient black carbon and brown carbon from fossil fuel and biomass burning sources. Journal of Geophysical Research-Atmospheres 120(13):6619-6633.

Jacobson MZ. 2001. Strong radiative heating due to the mixing state of black carbon in atmospheric aerosols. Nature 409(6821):695-697.

Jacobson MZ. 2012. Investigating cloud absorption effects: Global absorption properties of black carbon, tar balls, and soil dust in clouds and aerosols. Journal of Geophysical Research-Atmospheres 117:25.

Kulmala M, Rannik U, Zapadinsky EL, Clement CF. 1997. The effect of saturation fluctuations on droplet growth. Journal of Aerosol Science 28(8):1395-1409.

Lack DA, Langridge JM, Bahreini R, Cappa CD, Middlebrook AM, Schwarz JP. 2012. Brown carbon and internal mixing in biomass burning particles. Proceedings of the National Academy of Sciences of the United States of America 109(37):14802-14807.

Langridge JM, Richardson MS, Lack DA, Brock CA, Murphy DM. 2013. Limitations of the Photoacoustic Technique for Aerosol Absorption Measurement at High Relative Humidity. Aerosol Science and Technology 47(11):1163-1173.

Lau KM, Wu HT. 2003. Warm rain processes over tropical oceans and climate implications. Geophysical Research Letters 30(24):5.

Liu D, Allan J, Whitehead J, Young D, Flynn M, Coe H, McFiggans G, Fleming ZL, Bandy B. 2013. Ambient black carbon particle hygroscopic properties controlled by mixing state and composition. Atmos. Chem. Phys. 13(4):2015-2029.

Liu S, Aiken AC, Gorkowski K, Dubey MK, Cappa CD, Williams LR, Herndon SC, Massoli P, Fortner EC, Chhabra PS et al. . 2015. Enhanced light absorption by mixed source black and brown carbon particles in UK winter. Nature Communications 6:10.

Lohmann U, Feichter J. 2005. Global indirect aerosol effects: a review. Atmospheric Chemistry and Physics 5:715-737.

Luo W, Majumder MS, Liu D, Poirier C, Mandl KD, Lipsitch M, Santillana M. 2020. The role of absolute humidity on transmission rates of the COVID-19 outbreak. medRxiv:2020.02.12.20022467.

Mikhailov EF, Vlasenko SS, Podgorny IA, Ramanathan V, Corrigan CE. 2006. Optical properties of soot-water drop agglomerates: An experimental study. Journal of Geophysical Research-Atmospheres 111(D7).

Nessler R, Weingartner E, Baltensperger U. 2005. Effect of humidity on aerosol light absorption and its implications for extinction and the single scattering albedo illustrated for a site in the lower free troposphere. Journal of Aerosol Science 36(8):958-972.

Onasch TB, Massoli P, Kebabian PL, Hills FB, Bacon FW, Freedman A. 2015. Single Scattering Albedo Monitor for Airborne Particulates. Aerosol Science and Technology 49(4):267-279.

Radlach M, Behrendt A, Wulfmeyer V. 2008. Scanning rotational Raman lidar at 355 nm for the measurement of tropospheric temperature fields. Atmospheric Chemistry and Physics 8(2):159-169.

Regayre LA, Johnson JS, Yoshioka M, Pringle KJ, Sexton DMH, Booth BBB, Lee LA, Bellouin N, Carslaw KS. 2018. Aerosol and physical atmosphere model parameters are both important sources of uncertainty in aerosol ERF. Atmos. Chem. Phys. 18(13):9975-10006.

Roelofs GJ. 2013. A steady-state analysis of the temperature responses of water vapor and aerosol lifetimes. Atmospheric Chemistry and Physics 13(16):8245-8254.

Stubenrauch CJ, Cros S, Guignard A, Lamquin N. 2010. A 6-year global cloud climatology from the Atmospheric InfraRed Sounder AIRS and a statistical analysis in synergy with CALIPSO and CloudSat. Atmos. Chem. Phys. 10(15):7197-7214.

Swietlicki E, Hansson HC, Hameri K, Svenningsson B, Massling A, McFiggans G, McMurry PH, Petaja T, Tunved P, Gysel M et al. . 2008. Hygroscopic properties of submicrometer atmospheric aerosol particles measured with H-TDMA instruments in various environments - a review. Tellus Series B-Chemical and Physical Meteorology 60(3):432-469.

Tang IN. 1996. Chemical and size effects of hygroscopic aerosols on light scattering coefficients. Journal of Geophysical Research-Atmospheres 101(D14):19245-19250.

Tang JW, Li Y, Eames I, Chan PKS, Ridgway GL. 2006. Factors involved in the aerosol transmission of infection and control of ventilation in healthcare premises. Journal of Hospital Infection 64(2):100-114.

Weingartner E, Burtscher H, Baltensperger U. 1997. Hygroscopic properties of carbon and diesel soot particles. Atmospheric Environment 31(15):2311-2327.

Wulfmeyer V, Hardesty RM, Turner DD, Behrendt A, Cadeddu MP, Di Girolamo P, Schlüssel P, Van Baelen J, Zus F. 2015. A review of the remote sensing of lower tropospheric thermodynamic profiles and its indispensable role for the understanding and the simulation of water and energy cycles. Reviews of Geophysics 53(3):819-895.

Xu L, Penner JE. 2012. Global simulations of nitrate and ammonium aerosols and their radiative effects. Atmos. Chem. Phys. 12(20):9479-9504.

Yu H, Kaufman YJ, Chin M, Feingold G, Remer LA, Anderson TL, Balkanski Y, Bellouin N, Boucher O, Christopher S et al. . 2006. A review of measurement-based assessments of the aerosol direct radiative effect and forcing. Atmospheric Chemistry and Physics 6:613-666.

Zhou JC, Xu XZ, Zhao WX, Fang B, Liu QQ, Cai YQ, Zhang WJ, Venables DS, Chen WD. 2020. Simultaneous measurements of the relative-humidity-dependent aerosol light extinction, scattering, absorption, and single-scattering albedo with a humidified cavity-enhanced albedometer. Atmospheric Measurement Techniques 13(5):2623-2634.

2 Humidified Cavity Attenuated Phase-Shift Albedometer

Water condensing on atmospheric particles can enhance their ability to scatter and absorb sunlight. Therefore, an accurate assessment of these enhancements is key to understand the particles' effects on climate. A novel method for measuring the light extinction and scattering of atmospheric particles exposed to high relative humidity has been developed. A cavity attenuated phase-shift albedometer (CAPS-PM_{SSA}) was integrated with a humidifier that allows us to control the humidity of the sample volume. In this chapter we describe the instrument and report various characterizations of the instrument. Of particular interest to absorption measurement using this instrument is the size-dependent truncation, or the amount of light lost due to leakage through the instrument's apertures. Custom Python software for predicting this truncation is introduced and compared to empirical corrections. It is found that the truncation is enhanced by the reflectivity of the cavity's central tubing, and the empirical methods are the best method to use for now.

2.1 Introduction

Aerosol and water vapor are abundant within earth's atmosphere and interact with each other playing a significant role in regulating earth's radiative balance. Aerosol directly influence the amount of light reaching Earth's surface through light scattering and absorption, commonly referred to as the aerosol direct effect (Charlson et al. 1992). Parameters related to aerosol, especially light-absorbing aerosol, represent some of the largest sources of uncertainty in climate models (Regayre et al. 2018; Bellouin et al. 2020). One area in which this could be improved is how absorption from light-absorbing aerosol responds to increasing humidity (Cappa et al. 2012; Wang et al. 2018). Due to the difficulty of the measurement, there is a lack of data quantifying how the absorption changes with humidity for light-absorbing aerosol. It is because of these challenges that new instrumentation is necessary for the reduction of uncertainties associated with aerosol representations in models.

2.1.1 Hygroscopic Properties of Aerosol

Aerosol that readily adsorb water in an environment at a given relative humidity (RH) are referred to as hygroscopic. When exposed to a change in RH, an aerosol will exchange water molecules with the atmosphere. As a result, the size of the aerosol changes until the vapor pressure of the water adjacent to the aerosol is in equilibrium with the surrounding environment at the new RH. The change in aerosol size due to a change in RH from 0 to RH is quantified by the growth factor defined as:

$$g[RH] = d[RH]/d_0 \qquad \text{Equation 2.1}$$

where d_0 is the dry diameter, or diameter when RH=0%, of the aerosol. However, RH=0% is difficult to achieve. For aerosol size changes when the relative humidity increases from RH_{lo} to RH_{hi}, Equation 2.1 can be expressed as:

$$g[RH_{hi}, RH_{lo}] = \frac{g[RH_{hi}]}{g[RH_{lo}]} = \frac{d[RH_{hi}]}{d[RH_{lo}]} \qquad \text{Equation 2.2}$$

This equation allows for comparison of aerosol size changes between any two relative humidity values.

Köhler theory is typically employed to describe the growth of hygroscopic aerosol exposed to a humid atmosphere. The diameter of a hygroscopic aerosol in equilibrium with the atmosphere is dependent on the concentration of the solute within the aerosol, the Raoult effect, as well as the curvature of the aerosol, the Kelvin effect (H.R. Pruppacher 1997). Petters and Kreidenweis distilled this formulation down to a single parameter equation known as the κ-Köhler equation (Petters and Kreidenweis 2007). This formulation uses a single parameter, hygroscopicity parameter κ, to relate the water activity (a_w) of an aerosol to the volume of water uptake (V_w) for a given solute volume (V_s):

$$\frac{1}{a_w} = 1 + \kappa \frac{V_s}{V_w} \qquad \text{Equation 2.3}$$

For large droplets, 100nm or greater, the water activity and RH are nearly equal (Lewis 2008; Brock et al. 2016). This allows for a simplified form of the κ-Köhler parameterization for determining the diameter ratio:

$$g[RH] = \left(1 + \kappa \frac{RH}{100 - RH}\right)^{1/3} \qquad \text{Equation 2.4}$$

This formulation is with respect to the dry volume equivalent diameter of the aerosol, so often this equation is applied in conjunction with Equation 2.2 for estimating the value of an aerosol's κ value.

Humidified tandem differential mobility analyzers (H-TDMA) have been the primary method of determining an the hygroscopicity of different aerosol particles (Swietlicki et al. 2008). The technique exposes the same aerosol sample at two different relative humidity values and then measure is the size distribution of the aerosol at each RH value to determine g. The hygroscopicity of an aerosol is largely dependent on its composition. For example, soot is generally hydrophobic when freshly emitted (Weingartner et al. 1997), meanwhile inorganics salts such as ammonium sulfate are very hygroscopic (Tang and Munkelwitz 1994; Petters and Kreidenweis 2007). In fact, aerosol hygroscopicity tends to be inversely correlated with carbonaceous fraction (Carrico et al. 2005; Orozco et al. 2016).

2.1.2 Optical Properties of Aerosol

The single scattering albedo (SSA) of an aerosol at a specific wavelength, λ, can be described by taking the ratio of the aerosol's scattering (σ_{sca}) and extinction (σ_{ext}) cross-sections at λ to give you single scattering albedo (SSA):

$$SSA[\lambda] = {\sigma_{sca}[\lambda]}\Big/{\sigma_{ext}[\lambda]} \qquad \text{Equation 2.5}$$

The single scattering albedo is an important quantity for determining the climatic impact of aerosol (Chylek and Wong 1995). Since scattering and absorption are additive, only two of the three optical properties are necessary to calculate SSA. Often the optical

properties of an aerosol are wavelength dependent. For absorption, the wavelength dependence is often quantified using measurements at two wavelengths through the absorption Ångström exponent (AAE) (Ångström 1964):

$$AAE[\lambda_1, \lambda_2] = -ln\left[\frac{\sigma_{abs}\,[\lambda_1]}{\sigma_{\,abs}[\lambda_2]}\right] \Big/ ln\left[\frac{\lambda_1}{\lambda_2}\right] \qquad \text{Equation 2.6}$$

Angström exponents can be extended to scattering and extinction and are often referred to as the scattering Ångström exponent (SAE) and extinction Ångström exponent (EAE), respectively.

2.1.3 Measuring Absorption of Humidified Aerosol

Direct methods of measuring absorption are generally not suited for high relative humidity experiments. Filter deposition-based methods, such as the particle soot absorption photometer (PSAP), are prone to biases and perform erratically at medium-high RH (Arnott et al. 2003). Photoacoustic instruments, which measure absorption by converting absorbed electromagnetic energy into an acoustic wave, perform poorly when the RH ≥65% (Arnott et al. 2003). This is due to the loss of acoustic energy in absorbing aerosol due to the evaporation of water (latent heat) within the sample (Langridge et al. 2013). Measuring the extinction and scattering of humidified aerosol has proven less daunting. Nephelometers are generally employed for experiments looking at the scattering of lab and ambient aerosol (Fierz-Schmidhauser et al. 2010; Gomez et al. 2018). Cavity-based systems, such as cavity ring down spectrometers (CRDS), have been implemented to determine the extinction of humidified aerosol (Flores et al. 2012; Brock et al. 2016). The cavity attenuated phase-shift (CAPS) technique has allowed extinction measurements with large optical path lengths and compact instrumental size (Kebabian et al. 2007). One such system was recently outfitted with an integrating nephelometer for simultaneous measurement of particle extinction and scattering on the same volume (Onasch et al. 2015). This instrument is known as the CAPS-PM_{SSA}, and its modification for humidity experiments and subsequent characterization are the primary focus of this chapter.

Absorption can be inferred from an aerosol sample in the CAPS-PM_{SSA} using the extinction minus scattering method (EMS). The EMS method is generally only sensitive if the extinction measurement is performed over a long optical path length, such as those obtained using an optical cavity (H. Moosmüller et al. 2009). The big disadvantage of determining absorption using EMS that the absorption of high SSA aerosol have high uncertainty. The high relative uncertainty for absorption is due to the uncertainty in scattering and extinction being added in quadrature, whereas the absorption is calculated by taking a difference. It is therefore best to perform extinction and scattering measurements simultaneously and on the same sample volume to avoid systematic errors in either measurement (H. Moosmüller et al. 2009). This is especially true for measurements of aerosol where humidity can alter their optical properties. Additionally, any biases in the extinction and scattering measurement carry over into the calculated absorption. It is therefore imperative to minimize, or correct, any form of bias present in either measurement. The next section covers one such bias and how we correct for it in the H-CAPS-PM_{SSA}.

2.1.4 Truncation Errors in Scattering Measurement

Scattering is not angularly isotropic; rather, the intensity of light scattered at specific angles are highly dependent on the size, shape, and refractive index of the particle (Bohren and Huffman 1998). To measure the integrated scattering coefficient of an aerosol sample, an instrument would need to measure the full scattering phase function (Varma et al. 2003). However, this is infeasible as apertures are needed for light and aerosol to enter the instrument and the instrument must be finite in length. As a result, constraints are placed on scattering instrumentation on the near forward and backward scattering angles (Anderson et al. 1996). Truncation refers to the unmeasured scattered light due to these instrumental constraints. Aerosol become more forward scattering as they increase in size, thus larger aerosol will have high truncation error and the truncation error of hygroscopic aerosol will increase with RH. Additionally, truncation errors can be a factor of two larger for light-absorbing aerosol than for non-absorbing aerosol (Hans

Moosmüller and Arnott 2003). Recently, an albedometer was developed incorporating cavity-enhanced extinction measurements and similar scattering measurement geometry to the CAPS-PM_{SSA} (Zhou et al. 2020). This study used truncation reduction tubes to limit angular truncation losses, but size-dependent truncation corrections were not reported.

2.2 Instrumental Overview

2.2.1 Cavity Attenuated Phase Shift Albedometer

The following section is a brief description of the CAPS-PM_{SSA}. A more complete description can be found in Onasch et al., (Onasch et al. 2015). The CAPS-PM_{SSA} measures both the scattering and extinction attenuation coefficients simultaneously, and the measurement for both parameters is performed on the same sample volume. Figure 2.1 shows the internal geometry of the CAPS-PM_{SSA}. The optical cell within the CAPS-PM_{SSA} is bookended by two high reflectivity mirrors (HRM). The reflectivity of these mirrors is greater than 0.9998, which allows for an equivalent optical path length of 2km. Light emitted from a square wave modulated (17kHz) light emitting diode (LED) at is collimated, passed through a bandpass filter (BP) centered on 450nm, and then enters the optical cavity through the input HRM. Light that transmits through the output HRM is imaged onto a large vacuum photodiode (PD). Light that makes it this far is phase-shifted from the input light, and this phase shift is dependent on the extinction within the cell (Kebabian et al. 2007). The optical cavity is encased by an integrating sphere used for scattering measurement; this geometry allows for a maximum amount of light to be collected by the photomultiplier tube (PMT) and reduces angular bias (Varma et al. 2003). Scattering measurements are only performed while the LED is off to reduce measurement of stray radiation, and apertures are used to separate the HRM from the aerosol sample. Aerosol are passed through the space between the two apertures, and the space between each aperture and HRM are purged with filtered air to reduce the chances of aerosol depositing on the HRM. Due to the purge space, a geometrical correction to

the extinction measurement is required. Onasch et al. (Onasch et al. 2015) determined this correction for the CAPS-PM_{SSA} to be 1.37, and this correction is applied to the extinction measurement via the instrument's firmware.

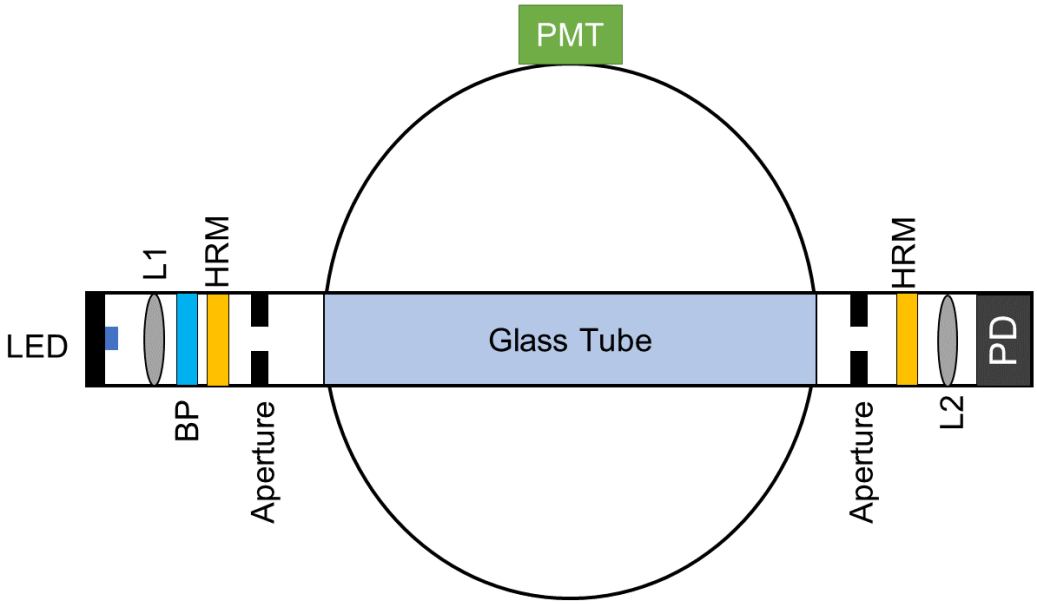

Figure 2.1: Diagram of the CAPS-PM_{SSA}. Some of the major components include an LED light source, a collimating lens (L1), a bandpass filter (BP), two apertures, two highly reflective mirrors (HR), a collection lens (L2). Extinction measurements are performed using a photodiode, while scattering measurements are performed using a photomultiplier tube (PMT). This diagram is based on Figure 1 from Onasch et al. (Onasch et al. 2015).

2.2.2 Humidification System

The following section is a brief overview the of humidification system and enclosure housing the CAPS-PM_{SSA}. Greater detail is covered in Carrico et al.(Carrico et al. 2021). A diagram of the enclosure is shown in Figure 2.2. Upon entry aerosol are passed through a desiccant dryer containing DrieRite calcium sulfate. After passing through the dryer, the aerosol could pass through one of two lines depending on whether the system is operating in dry mode or humid mode. The system's mode can be selected using custom

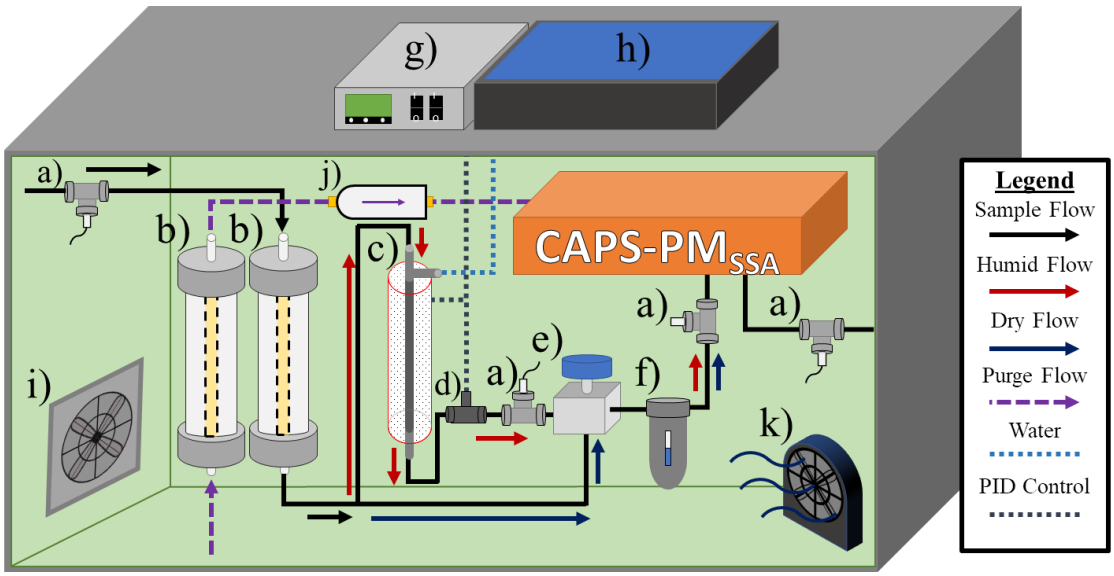

Figure 2.2: Diagram of the enclosure containing the humidification system and H-CAPS-PM_{SSA}. The enclosure contains the following **a)** RH&T sensor, **b)** desiccant dryer, **c)** humidifier, **d)** capacitive RH sensor, **e)** actuated ball valve, **f)** condensation trap, **g)** PID controller, **h)** water reservoir, **i)** thermoelectric cooler, **j)** HEPA filter, **k)** circulating fan. Incoming aerosol sample flow is depicted by a solid black line. After the split in the sample line, humid and dry aerosol flow are depicted by red and blue lines, respectively. The flow for purging the mirrors is depicted by the purple dashed line. The water line and the PID control for the humidifier are depicted by blue and grey dotted lines.

data acquisition and process control software written in LabView. The software communicates with an actuated 3-way ball valve, which allows us to control whether aerosol pass through the dry line or the humid line. In the humid line, aerosol is passed through a humidifier before being sent to the CAPS-PM_{SSA}. The humidifier is cylindrical in construction, and it consists of water permeable tubing surrounded concentrically by a stainless-steel shell. The space between the tubing and the shell is occupied by water, and we refer to this space as the water jacket. The aerosol sample passes through the water permeable tubing, so the only thing separating the aerosol from the water jacket is the water permeable tubing. Heat tape is wrapped around the shell, and insulation is wrapped around the heat tape. Humidification within the humid line is accomplished by heating the water jacket, the temperature of which is controlled by a proportional-integral-derivative (PID) controller. This feedback loop is interfaced with a capacitive RH sensor

immediately downstream of the humidifier. The instrument is outfitted with four relative humidity and temperature sensors (RH&T). One RH&T sensor is immediately downstream of the inlet, one downstream of the humidifier, one immediately upstream of the CAPS-PM_{SSA}, and one immediately downstream of the CAPS-PM_{SSA}. Despite efforts to keep the H-CAPS-PM_{SSA} isothermal using insulation and circulating fans, there is an increasing temperature gradient between the humidifier and the CAPS-PM_{SSA}. As a result, deliquescent aerosol will deliquesce upstream of the CAPS-PM_{SSA}, and then as the RH decrease,s the aerosol will move down the upper part of their hysteresis curve. This means the observed deliquescence RH for aerosol are much lower than expected.

2.2.3 CAPS-PM_{SSA} Truncation

The CAPS-PM_{SSA} has openings in the near forward and backward scattering regions of the integrating sphere. Any scattered light that leaks through these openings goes unmeasured and represents a critical measurement bias, which we refer to as truncation. We model truncation errors using two algorithms employing Lorenz-Mie theory (henceforth referred to as Mie). The first is the C-based MieAmigo, a software developed by Aerodyne for estimating the truncation within the CAPS-PM_{SSA}. The second is a custom software written in Python developed to have more flexibility and greater batch processing ability compared to MieAmigo. Both are based on the Bohren and Huffman algorithm for determining the optical properties of spheres (Bohren and Huffman 1998). The Python code relies on the PyMieScatt Python package, developed by Benjamin Sumlin at Washington University (Sumlin et al. 2018).

The MieAmigo and the Python-based codes treat the geometry of the cell similarly. This geometry is described in Figure 2.3. The z-axis is defined along the axial coordinate of the glass tube in the direction of the light propagation, and the origin is defined at the center of the integrating sphere. We also assume azimuthal symmetry and that scattering is only contributed by aerosol along the z-axis. There are three regions in which aerosol can occupy within the CAPS-PM_{SSA}: (1) before the integrating sphere, (2) inside of the integrating sphere, and (3) after the integrating sphere. Only the case of an aerosol

occupying the second is depicted in Figure 2.3. The forward (θ_F) and backward (θ_B) scattering angles represent the angles in which light does not escape the integrating sphere. They are defined based on an aerosol's position with respect to each opening. For example, θ_F is defined as the angle from the z-axis in the forward direction to a diagonal drawn from the particle to the edge of the opening in the forward direction, respectively. The definition for θ_B is similar, but the diagonal is now drawn from the particle to the edge of the opening in the backward direction.

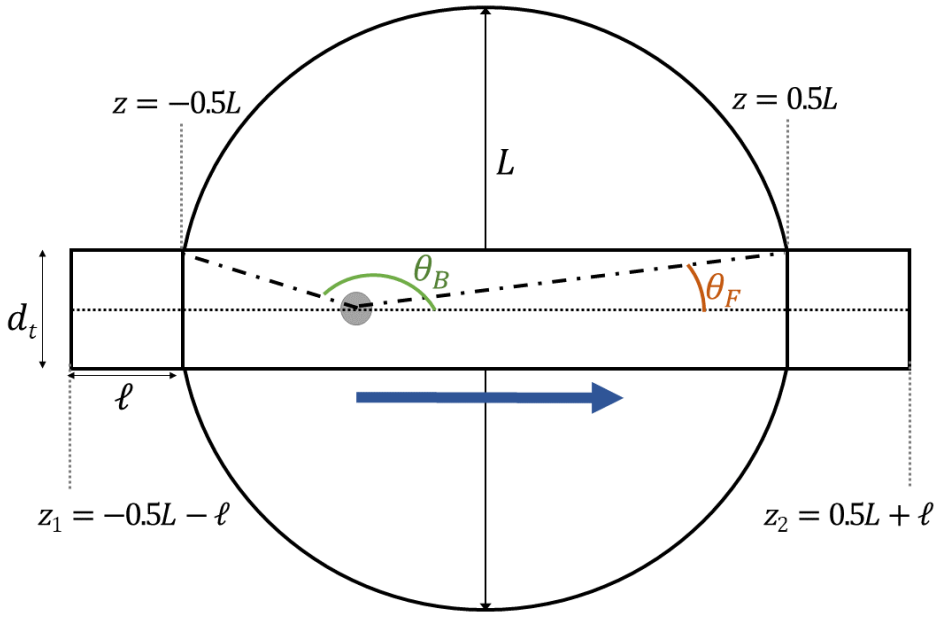

Figure 2.3: Geometry considered for truncation calculations in the CAPS-PMSSA. The z-axis is taken as the center line in each cell, and important positions along the z-axis are denoted at the bottom. The blue arrow indicates the direction of light propagation. Also depicted are the length of the cell (L), the diameter of the tube (d_t), the length in which calculations are extended outside of the cavity (ℓ), the forward scattering angle (θ_F) the backward scattering (θ_B), and the limits of integration (z_1 and z_2).

Truncated and ideal scattering efficiencies are calculated at several positions along the z-axis. The truncation factor is then defined as a ratio of the truncated scattering efficiency to the ideal scattering efficiency integrated from z_1 to z_2 along the z-axis:

$$\mathcal{T}(x) = \mathcal{T}(x_0, m_0)^{-1} \frac{\int_{z_1}^{z_2} Q_{trunc}(x, z, m) dz}{\int_{z_1}^{z_2} Q_{ideal}(x, z, n + ik)\ dz} \qquad \text{Equation 2.7}$$

where m is the complex refractive index of the aerosols, x is the is the size parameter of the aerosol ($x = 2\pi\lambda/d_p$), and $\mathcal{T}(\mathrm{x}_0, m_0)^{-1}$ is the truncation factor calculated for the aerosol used to calibrate the instrument; x_0 is the size parameter of the calibration aerosol; and m_0 is the refractive index of the calibration aerosol. It is assumed that x_0 is small enough such that $\mathcal{T}(\mathrm{x}_0, m_0)^{-1}$ is one 1. The calibration is described in greater detail in Section 2.3.2, but our process involves calibrating with ammonium sulfate size selected at 150nm. The Python based program assumes 150nm monodisperse ammonium sulfate aerosol for the default value for $\mathcal{T}(\mathrm{x}_0, m_0)^{-1}$; however, this can be changed in the dictionary containing instrumental settings. To quantify light that might scatter into the integrating sphere from aerosol between the HRM and the integrating sphere, the integration range begins and ends a distance (ℓ) outside of the integrating sphere. For an integrating sphere of length L, the integration range starts at $z_1 = -0.5L - \ell$ and ends at $z_2 = 0.5 + \ell$. The scattering efficiency is then defined as the scattering phase function integrated from θ_F to θ_B:

$$Q(x, z, m) = \int_{\theta_F}^{\theta_B} \frac{2P[x, \theta, m]}{x^2} sin[\theta] d\theta \qquad \text{Equation 2.8}$$

where P is the scattering phase function, or angular distribution of scattered intensity. We assume that the scattering phase function is symmetric about the z-axis. For Q_{ideal}, the integration range is thus defined as $\theta_F = 0$ to $\theta_B = 180$. The angles of integration for Q_{trunc} are dependent on the position of the aerosol with respect to the interface of the glass tube and the integrating sphere, as shown in Figure 2.3. For θ_F we have:

$$\theta_F = \begin{cases} \vartheta_F;\ z\ < 0.5L \\ \pi - \vartheta_F;\ \ z \geq 0.5L \end{cases} \qquad \text{Equation 2.9}$$

For θ_B we have:

$$\theta_B = \begin{cases} \vartheta_B; \ z < -0.5L \\ \pi - \vartheta_B; \ z \geq -0.5L \end{cases} \qquad \text{Equation 2.10}$$

We define ϑ_F and ϑ_B as the arctangents of the aerosol's displacement from each interface and the half diameter of the glass tube:

$$\vartheta_F = tan^{-1}\left[\frac{0.5d_t}{|0.5d_t - z|}\right]$$
$$\vartheta_B = tan^{-1}\left[\frac{0.5d_t}{|-0.5d_t - z|}\right] \qquad \text{Equation 2.11}$$

Our Python module uses trapezoidal integration to determine each of the integrals (SciPy). The default instrument parameters provided in Table 2.1 are used in both codes.

Table 2.1: The default parameters used in MieAmigo and our Python based truncation code.

$\boldsymbol{\lambda}$	$\boldsymbol{L}$	$\boldsymbol{d_t}$	$\boldsymbol{\ell}$	$\boldsymbol{dz}$	$\boldsymbol{d\theta}$	$\boldsymbol{d_0}$	$\boldsymbol{m_0}$
450 nm	10 cm	1 cm	0.6 cm	0.112 cm	0.2°	150 nm	1.53+0i

The Python module for estimating truncation contains four primary functions: *trunc_mono*, and *trunc_size_dist*, *trunc_lognorm*, *settings*. Truncation factors for monodisperse and polydisperse aerosol can be calculated using *trunc_mono* and *trunc_size_dist* respectively. *trunc_lognorm* is a specialized wrapper around *trunc_size_dist* that calculates the truncation factors for a distribution of known geometric mean and standard deviation. The *settings* function is called in each of the other functions and stores the default parameters listed in Table 2.1. When called, it returns a Python dictionary containing all the default instrument parameters. These default parameters can be changed in the setting function, though any change should be accompanied by recalculating $\mathcal{T}(\mathrm{x}_0, m_0)$. This recalculation can be performed in the function by setting the variable *calBool=True*, allowing for greater flexibility in determining the truncation factor. The added flexibility allows for modifications between different CAPS-PM_{SSA} instruments or different calibration sources, but the user can adjust different parameters such as ℓ to better match experimental results. Additionally,

this level of flexibility allows a user to completely change the instrumental parameters to match different instruments of similar geometry. One drawback of the Python based code in comparison to MieAmigo is the performance. Python is inherently slower than C; therefore, calculations take longer. While the Python code's scripting capability usually mitigates this, it is something to keep in mind when dealing with size distributions with many bins.

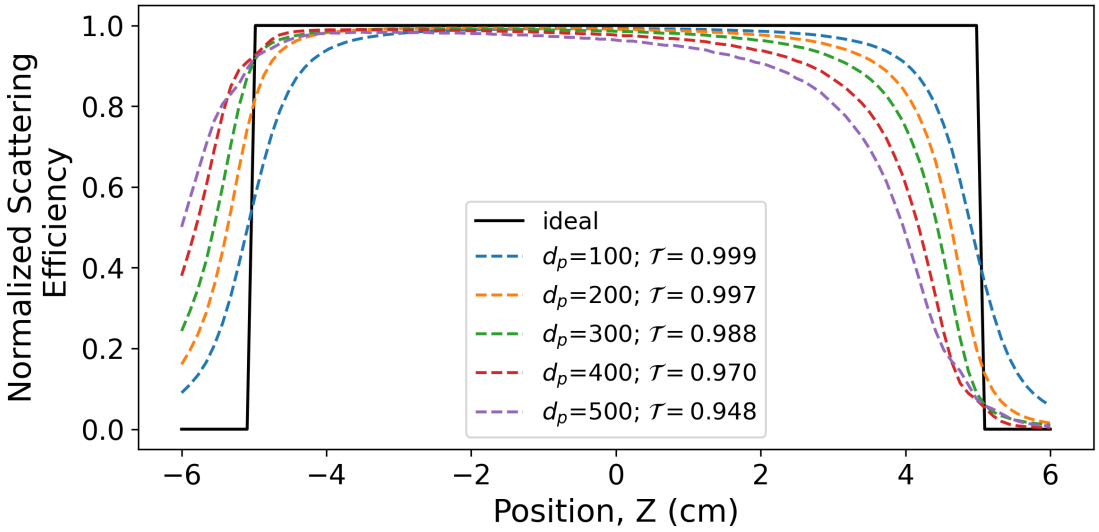

Figure 2.4: Normalized scattering efficiency of various diameter aerosol within the CAPS-PM$_{SSA}$ modelled using the Python based truncation code. The scattering efficiencies were normalized such that the ideal scattering efficiency inside of the integrating sphere was 1.0 for each diameter. Each diameter was simulated using a m= 1.53+0j, and $\ell = 1.0$ cm was used in the calculations.

Figure 2.4 shows monodisperse Python based Mie estimates of the scattering efficiency, normalized to the ideal case, along the z-axis of the CAPS-PM$_{SSA}$. The cases of $z > 5$ cm and $z < -5$ cm in this plot represent the light that is forward scattered and backward scattered into the CAPS-PM$_{SSA}$, respectively. For 100nm particles, the case with the most isotropic scattering phase function, the amount of light backscattered into the instrument is nearly equal to the front scattered light. As the diameter increases, the percent of measured scattered light that came from outside the integrating sphere increases from

4.3% to 8.2%. In each case but the 100nm case, the truncation factor was largely dominated by forward scattered light from the $z < -5$ region. Light scattered into the sphere partially compensates the light exiting the integrating sphere. Despite these competing effects, the measured scattering still becomes more truncated as the size of the aerosol increases. The ratio of light gained to light lost inside of the cell decreased from 0.64 to 0.51 as aerosol diameter increased from 100 to 500 nm. However, Figure 2.4 suggests that larger ℓ may be necessary to fully quantify the light gained from scattering outside of the integrating sphere, especially as the diameter of the aerosol increases.

2.3 Characterizing the H-CAPS-PM$_{SSA}$

2.3.1 Geometry Factor

As mentioned in Section 2.2.1, the space between the HRM and apertures within the CAPS-PM$_{SSA}$ is purged with dry air (see Figure 2.1). As a result, a small section of the cavity is void of aerosol. This void along the optical path, along with the purging air diluting the aerosol sample a small amount, results in the extinction measurement being biased (Kebabian et al. 2007; Onasch et al. 2015). Onasch et al. measured the extinction of PSL spheres of varying diameters, compared experimental results to the expected extinction from Mie theory, and determined the geometry factor to be 1.37 (Onasch et al. 2015). Modini et al. (Modini et al. 2020) applied a similar approach to several CAPS-PM$_{SSA}$ instruments of varying wavelengths during several field deployments during a yearlong study. They found that instrument-to-instrument variability in the geometry factor, even from instruments of the same wavelength, varied by as much as 3% for some instruments over the test period (Modini et al. 2020).

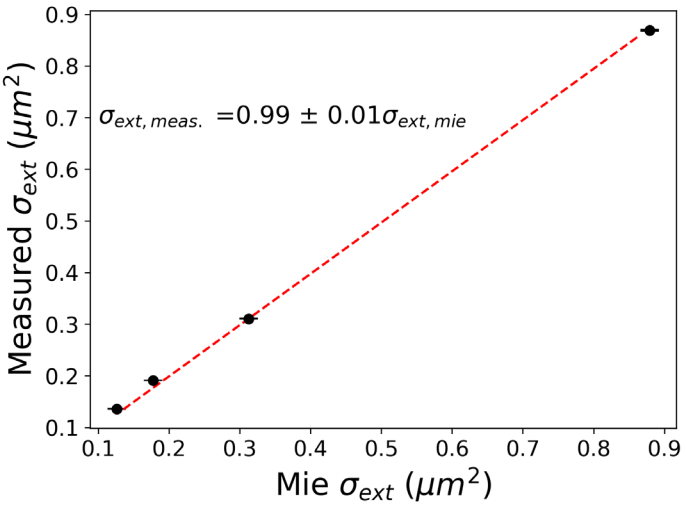

Figure 2.5: Linear fit of measured and modelled extinction cross-sections for polystyrene Latex spheres of varying size. A slope near 1 indicates that the geometric factor has not deviated from the factory setting.

To confirm our instrument's geometric factor, we measured the extinctions of four different sizes of polystyrene Latex spheres (PSL) (269nm, 300nm, 350nm, and 495nm). The PSL (ThermoScientific TS#3xxxA) were generated using a portable aerosol generator (TSI 3079A), and then mobility and mass size selected using an electrostatic classifier (TSI 3080) and a centrifugal particle mass analyzer (CPMA) connected in series. A condensation particle counter (CPC, TSI 3010) was run in parallel with the CAPS-PM_{SSA} to measure the particle concentration. Extinction cross-sections were determined by dividing the extinction attenuation coefficient measured by the CAPS-PM_{SSA} and the concentration. In Figure 2.4, we compare the measured extinction cross-section to the expected extinction calculated from PyMieScatt by using a linear fit. The slope is nearly 1.0, which confirms that the correction has not drifted or deviated from the firmware programmed value. This is an important parameter to confirm, as it suggests that further corrections to our extinction data is not necessary.

2.3.2 Calibration

To accurately determine the scattering of an aerosol, a cross-calibration step is necessary. This is performed by scaling the scattering coefficient to the extinction coefficient using a non-absorbing aerosol (ω∼1) with a relatively small diameter to avoid biases from truncation. For non-absorbing aerosol, the extinction and scattering should be equal. We regularly perform this calibration by generating and size-selecting ammonium sulfate using the same procedure outlined in Section 2.3.1. We chose to size select the ammonium sulfate ($(NH_4)_2SO_4$, Sigma Aldrich Inc. CAS 7783-20-2) at 150nm because it is small enough that truncation biases are low but large enough to get a relatively large dynamic range of signal (≥100 Mm^{-1}).

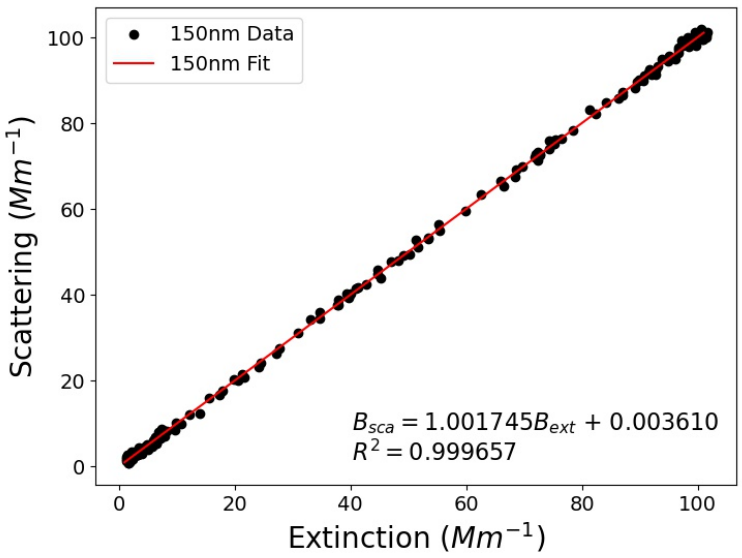

Figure 2.6: An example of a calibration fit using 150 nm ammonium sulfate aerosol. This was the second calibration used to confirm that the first calibration was effective.

Between 1 and 200nm the truncation normalization, $\mathcal{T}(x_0, m_0)^{-1}$, increases by only 0.014 for ammonium sulfate. However, between 200 and 300nm, the truncation normalization increases by 0.024. An example of this calibration is shown in Figure 2.6. The calibration is performed iteratively, and for each iteration, the calibration coefficient

is changed by multiplying the value of the slope until an iteration is performed where the slope is within 1% of unity. During a field campaign, Modini et al. (Modini et al. 2020) studied the stability of this calibration over the course of a field campaign. They found that the calibration parameter for the 450nm instrument drifted by as much 34% during the campaign, indicating the need to continually check the calibration of the instrument. They were unable to determine diagnostically if this was the result of instrumental malfunction.

2.3.3 Truncation Errors

Quantifying the size-dependent truncation for aerosol with extremely low absorption, such as ammonium sulfate, can be performed by measuring the SSA for various sizes of the aerosol. Because of the negligible absorption, the SSA for these aerosol should remain 1.0 regardless of diameter. Any deviation from 1.0 is the result of truncation and will scale directly with truncation. A comparison of the size-dependent truncation values for doubly size-selected ammonium sulfate is shown in Figure 2.7. As can be seen, the bias introduced by size-dependent truncation is as high as 13% for 500nm ammonium sulfate aerosol. Additionally, Mie scattering calculations underestimate the measured truncation, even when the *extra-length* parameter, ℓ, is set to 0. The reason for the discrepancy between the Mie based code and the measured truncation factors is likely the models' failure to account for the reflectivity of glass tube. The MieAmigo estimate is in good agreement with the Python estimate when $\ell = 0.6$, which is expected, as MieAmigo uses the same value for ℓ. Using radiative transfer modelling, Liu et al. (Liu et al. 2018) found that truncation was largely dependent on the size and morphology of the aerosol in addition to the reflectivity of the glass tube in the CAPS. Modini et al. improved on the Mie-based approach by incorporating Fresnel equations into the truncation calculation to estimate the likelihood of a scattered photon being reflected into or out of the integrating sphere (Modini et al. 2020). Upgrading the Python program with Fresnel equation reflection estimates is currently under way.

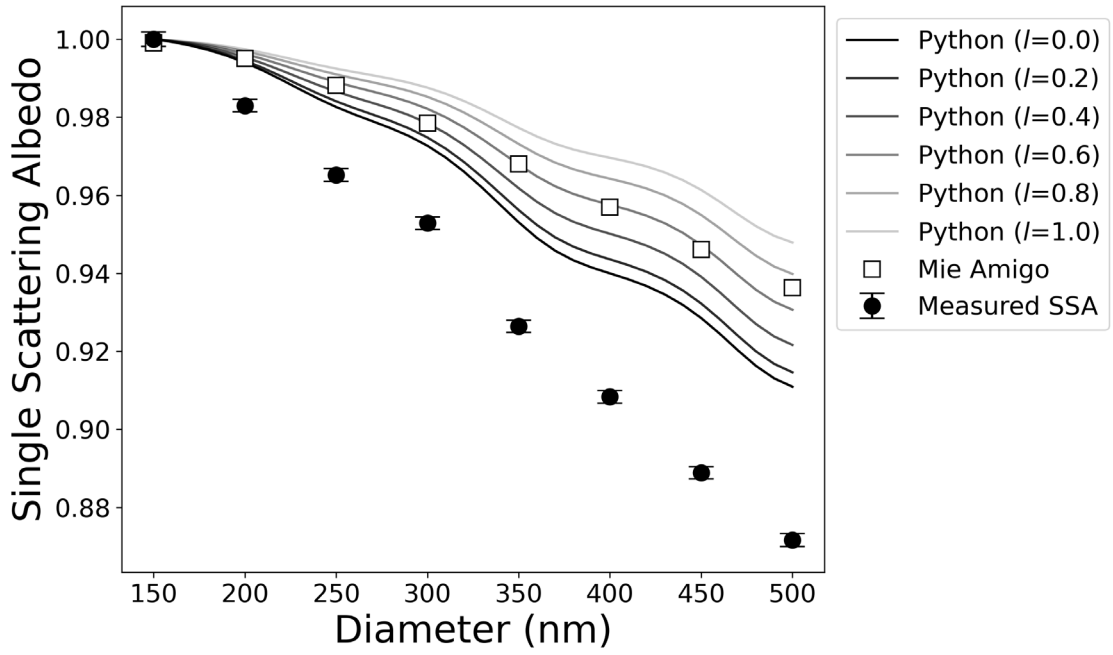

Figure 2.7: Comparison of measured SSA of ammonium sulfate aerosol to Mie based calculations for different diameter aerosol. Significant deviations between estimated and measured truncation values are highlighted. Python estimates were performed by varying the extra-length parameter, ℓ, from 0.0 to 1.0. These were estimated assuming a monodisperse distribution and a complex refractive index of 1.53+0j.

It is apparent from Figure 2.7 that an empirical approach is still necessary for accurately determining the truncation. Several experiments were performed to quantify the truncation related errors within the CAPS-PM_{SSA}. These experiments were then compared to truncation values estimated using both Python and MieAmigo. They were performed using ammonium sulfate, PSL, and nigrosin. Both ammonium sulfate and PSL have low absorption at 450nm. Nigrosin (Alfa-Aesar, Inc. CAS: 8005-03-6) is a light-absorbing aerosol that is often used as a surrogate for soot in aerosol optical properties studies. Nigrosin and PSL are spherical in shape, making them ideal for comparison with Mie theory (Lack et al. 2006). It has also been shown that ammonium sulfate can be closely approximated as a sphere optical studies as well (Perry et al. 1978; Dick et al. 1998). Estimating the truncation for nigrosin required simultaneous measurements of extinction and scattering using the CAPS-PM_{SSA} and absorption using a three-wavelength

photoacoustic soot spectrometer (PASS-3). For these measurements, we were careful to keep the sample RH low (<20%) to avoid biases in the absorption measurement. Using the additive relation between extinction, scattering, and absorption, we determined the truncation of nigrosin in the CAPS-PM_{SSA}:

$$\frac{B_{ext,CAPS} - B_{abs,PASS3}}{B_{sca,CAPS}} = \mathcal{T} \qquad \text{Equation 2.12}$$

The absorption Ångström exponent (AAE) calculated from the PASS-3's 405nm and 780nm channels was used to estimate the photoacoustic absorption signal at 450nm using Equation 2.6. The measured truncations for ammonium sulfate, PSL, and nigrosin are plotted in Figure 2.8.

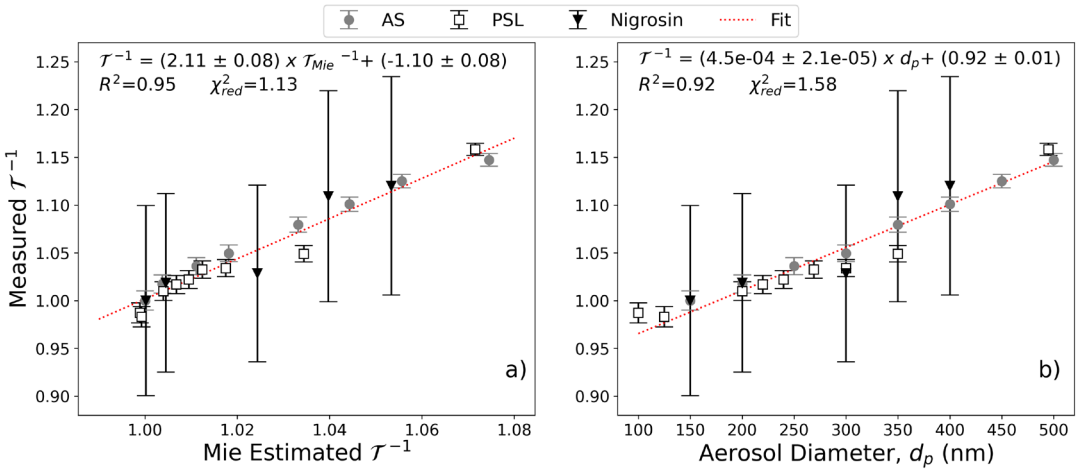

Figure 2.8: Empirical relations were determined for truncation corrections using dry ammonium sulfate (ammonium sulfate), polystyrene latex (PSL), and nigrosin. This was performed by: **a)** fitting the Mie truncations (Python) to the measured truncation values for all aerosol species and **b)** fitting the aerosol diameter to the measured truncation values for all aerosol species. Fitting results and quality of fit parameters are listed at the top of each plot.

These measured truncations were plotted against Mie calculated truncations from our custom software as well as volume equivalent diameters. Mie calculations were performed using the refractive indices in Table 2.2. The empirical relations were developed to estimate actual truncation using linear regression for both Mie estimated

truncation values, as well as particle diameter. Both models displayed a high degree of agreement, as $R^2 \geq 0.9$ and $\chi^2_{red} \leq 1.6$, with the Mie-based fit performing marginally better. However, the uncertainty of the diameter-based fit is about 1% for the range of 100-500nm, whereas the Mie-based fit is estimated to be about 10% in the same size range. This suggests that the diameter of the aerosol is the most important factor over the range of refractive indices explored.

Table 2.2: Refractive indices of test aerosol used to characterize the H-CAPS-PM_{SSA}.

Aerosol	**m=n+ki**	**Source**
Ammonium Sulfate	1.53+0.00i	(Toon et al. 1976)
PSL	1.59+0.00i	ThermoScientific
Nigrosin	1.63+0.16i	Chapter 3

The dataset explored in Figure 2.8 was compiled entirely from aerosol in conditions with low RH (<20%). Because of this, it is pertinent to understand how these truncation correction schemes perform when applied to humidified data. In Figure 2.9, we find that the diameter model performs best for humidified ammonium sulfate aerosol. These aerosol were size selected for three different diameters (100, 200, and 300nm) prior to humidification, and κ-Köhler theory was used to estimate the diameter of the humidified aerosol. The hygroscopic parameter, κ, was determined from extinction data (see Chapter 3). We wanted to focus on only deliquesced ammonium sulfate, so we focused on data collected when RH>70%. Volume mixing rules were used to estimate the refractive index of the ammonium sulfate and water mixtures for Mie truncation estimates. The R^2 and χ^2 statistics were used to determine how well the empirical models agree with the measured data. We found that the diameter-based empirical fit had very good agreement with the humidified ammonium sulfate data. The Mie truncation empirical fit did not perform as well but could still be used effectively. Both models seem to over predict the truncation somewhat for the 100nm size-selected aerosol. This is especially true for the Mie-based estimation, because truncation calculations flatten at 1.0 between 100-200nm, while the measured truncation correction continues to decrease. The Mie truncation model seems to

also under predict the truncation for the 200nm size-selected aerosol, though it is within the model uncertainty. Another difference between the two methods is the estimated uncertainties. The uncertainty for the diameter-based method is comparable to that predicted by Onasch et al. in the small particle limit but less than those reported in Modini et al. (Onasch et al. 2015; Modini et al. 2020).

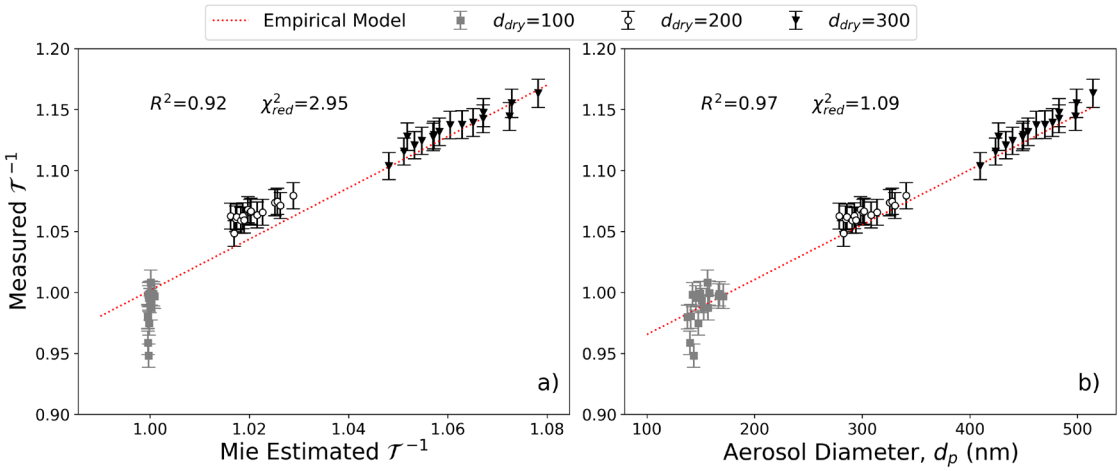

Figure 2.9: Overlay of the empirical relation developed in Figure 2.8 with humidified ammonium sulfate data. Here we show comparison of model and data for **a)** Mie estimated truncations **b)** diameters calculated using κ-Köhler theory. Aerosol were size-selected at 100, 200, and 300nm prior to humidification. Fit quality statistics are used to compare the empirical relations with the humidified data.

2.4 Summary and Conclusion

Determining the optical properties of humidified aerosol is challenging. This is especially true for determining changes in absorption because of humidification of atmospheric aerosol. To meet these challenges, we developed and characterized a humidified cavity attenuated phase shift albedometer (H-CAPS-PM_{SSA}). The instrument measures extinction and scattering at controlled relative humidity, and absorption can be determined from the extinction minus scattering (EMS) method. A limiting factor in the accuracy of EMS methods is the propagation of uncertainty from these two measurements. Biases such as size-dependent truncation of the scattering signal can lead

to significant biases in absorption measurement. Therefore, we have measured and reported size-dependent truncation of three important aerosol for characterizing optical instrumentation: polystyrene latex spheres, ammonium sulfate, and nigrosin. We have developed two empirical relations to correct for size-dependent truncation of the scattering signal. The first method was to relate Mie Theory calculations of the truncation to measured truncation values for all three aerosols using linear regression. The second method related the diameter of the aerosol to the measured truncation values. In each case, there was good agreement between the model and the data, but the method based on Mie theory performed mildly better than the aerosol diameter approach. For humidified ammonium sulfate aerosol, we found that the aerosol diameter approach performed much better. This suggests that aerosol diameter is more important that refractive index when determining size-dependent truncation. This study was limited to aerosol that are spherical or aerosol considered nearly spherical in the case of ammonium sulfate. Therefore, greater work would need to be done to relate truncation to morphology, especially for light-absorbing aerosol with complex morphology such as soot.

2.5 References

Anderson TL, Covert DS, Marshall SF, Laucks ML, Charlson RJ, Waggoner AP, Ogren JA, Caldow R, Holm RL, Quant FR et al. . 1996. Performance characteristics of a high-sensitivity, three-wavelength, total scatter/backscatter nephelometer. Journal of Atmospheric and Oceanic Technology 13(5):967-986.

Ångström A. 1964. The parameters of atmospheric turbidity. Tellus 16(1):64-75.

Arnott WP, Moosmuller H, Sheridan PJ, Ogren JA, Raspet R, Slaton WV, Hand JL, Kreidenweis SM, Collett JL. 2003. Photoacoustic and filter-based ambient aerosol light absorption measurements: Instrument comparisons and the role of relative humidity. Journal of Geophysical Research-Atmospheres 108(D1).

Bellouin N, Quaas J, Gryspeerdt E, Kinne S, Stier P, Watson-Parris D, Boucher O, Carslaw KS, Christensen M, Daniau AL et al. . 2020. Bounding Global Aerosol Radiative Forcing of Climate Change. Reviews of Geophysics 58(1).

Bohren CF, Huffman DR. 1998. Absorption and Scattering of Light by Small Particles. Wiley.

Brock CA, Wagner NL, Anderson BE, Attwood AR, Beyersdorf A, Campuzano-Jost P, Carlton AG, Day DA, Diskin GS, Gordon TD et al. . 2016. Aerosol optical properties in the

southeastern United States in summer - Part 1: Hygroscopic growth. Atmospheric Chemistry and Physics 16(8):4987-5007.

Cappa CD, Onasch TB, Massoli P, Worsnop DR, Bates TS, Cross ES, Davidovits P, Hakala J, Hayden KL, Jobson BT et al. . 2012. Radiative Absorption Enhancements Due to the Mixing State of Atmospheric Black Carbon. Science 337(6098):1078-1081.

Carrico CM, Kreidenweis SM, Malm WC, Day DE, Lee T, Carrillo J, McMeeking GR, Collett JL. 2005. Hygroscopic growth behavior of a carbon-dominated aerosol in Yosemite National Park. Atmospheric Environment 39(8):1393-1404.

Carrico CM, Capek TJ, Gorkowski KJ, Lam JT, Gulick S, Karacaoglu J, Lee JE, Dungan C, Aiken AC, Onasch TB et al. . 2021. Humidified Single Scattering Albedometer (H-CAPS-PMSSA): Design, Data-Analysis, and Validation. Aerosol Science and Technology:1-25.

Charlson RJ, Schwartz SE, Hales JM, Cess RD, Coakley JA, Hansen JE, Hofmann DJ. 1992. Climate Forcing by Anthropogenic Aerosols. Science 255(5043):423-430.

Chylek P, Wong J. 1995. Effect of absorbing aerosols on global radiation budget. Geophysical Research Letters 22(8):929-931.

Dick WD, Ziemann PJ, Huang PF, McMurry PH. 1998. Optical shape fraction measurements of submicrometre laboratory and atmospheric aerosols. Measurement Science and Technology 9(2):183-196.

Fierz-Schmidhauser R, Zieger P, Wehrle G, Jefferson A, Ogren JA, Baltensperger U, Weingartner E. 2010. Measurement of relative humidity dependent light scattering of aerosols. Atmospheric Measurement Techniques 3(1):39-50.

Flores JM, Bar-Or RZ, Bluvshtein N, Abo-Riziq A, Kostinski A, Borrmann S, Koren I, Koren I, Rudich Y. 2012. Absorbing aerosols at high relative humidity: linking hygroscopic growth to optical properties. Atmospheric Chemistry and Physics 12(12):5511-5521.

Gomez SL, Carrico CM, Allen C, Lam J, Dabli S, Sullivan AP, Aiken AC, Rahn T, Romonosky D, Chylek P et al. . 2018. Southwestern US Biomass Burning Smoke Hygroscopicity: The Role of Plant Phenology, Chemical Composition, and Combustion Properties. Journal of Geophysical Research-Atmospheres 123(10):5416-5432.

H.R. Pruppacher JDK. 1997. Microphysics of Clouds and Precipitation. Dordrecth, The Netherlands: Kluwer Academic Publishers.

Kebabian PL, Robinson WA, Freedman A. 2007. Optical extinction monitor using cw cavity enhanced detection. Review of Scientific Instruments 78(6).

Lack DA, Lovejoy ER, Baynard T, Pettersson A, Ravishankara AR. 2006. Aerosol absorption measurement using photoacoustic spectroscopy: Sensitivity, calibration, and uncertainty developments. Aerosol Science and Technology 40(9):697-708.

Langridge JM, Richardson MS, Lack DA, Brock CA, Murphy DM. 2013. Limitations of the Photoacoustic Technique for Aerosol Absorption Measurement at High Relative Humidity. Aerosol Science and Technology 47(11):1163-1173.

Lewis ER. 2008. An examination of Kohler theory resulting in an accurate expression for the equilibrium radius ratio of a hygroscopic aerosol particle valid up to and including relative humidity 100%. Journal of Geophysical Research-Atmospheres 113(D3).

Liu F, Snelling DR, Thomson KA, Smallwood GJ. 2018. Estimate of scattering truncation in the cavity attenuated phase shift PMSSA monitor using radiative transfer theory. Aerosol Science and Technology 52(5):588-596.

Modini RL, Corbin JC, Brem BT, Irwin M, Bertò M, Pileci RE, Fetfatzis P, Eleftheriadis K, Henzing B, Moerman MM et al. . 2020. Detailed characterization of the CAPS single scattering albedo monitor (CAPS PMssa) as a field-deployable instrument for measuring aerosol light absorption with the extinction-minus-scattering method. Atmos. Meas. Tech. Discuss. 2020:1-56.

Moosmüller H, Arnott WP. 2003. Angular truncation errors in integrating nephelometry. Review of Scientific Instruments 74(7):3492-3501.

Moosmüller H, Chakrabarty RK, Arnott WP. 2009. Aerosol light absorption and its measurement: A review. Journal of Quantitative Spectroscopy and Radiative Transfer 110(11):844-878.

Onasch TB, Massoli P, Kebabian PL, Hills FB, Bacon FW, Freedman A. 2015. Single Scattering Albedo Monitor for Airborne Particulates. Aerosol Science and Technology 49(4):267-279.

Orozco D, Beyersdorf AJ, Ziemba LD, Berkoff T, Zhang Q, Delgado R, Hennigan CJ, Thornhill KL, Young DE, Parworth C et al. . 2016. Hygrosopicity measurements of aerosol particles in the San Joaquin Valley, CA, Baltimore, MD, and Golden, CO. Journal of Geophysical Research: Atmospheres 121(12):7344-7359.

Perry RJ, Hunt AJ, Huffman DR. 1978. Experimental Determinations of Mueller Scattering Matrices for Nonspherical Particles. Applied Optics 17(17):2700-2710.

Petters MD, Kreidenweis SM. 2007. A single parameter representation of hygroscopic growth and cloud condensation nucleus activity. Atmospheric Chemistry and Physics 7(8):1961-1971.

Regayre LA, Johnson JS, Yoshioka M, Pringle KJ, Sexton DMH, Booth BBB, Lee LA, Bellouin N, Carslaw KS. 2018. Aerosol and physical atmosphere model parameters are both important sources of uncertainty in aerosol ERF. Atmos. Chem. Phys. 18(13):9975-10006.

Sumlin BJ, Heinson WR, Chakrabarty RK. 2018. Retrieving the aerosol complex refractive index using PyMieScatt: A Mie computational package with visualization capabilities. Journal of Quantitative Spectroscopy and Radiative Transfer 205:127-134.

Swietlicki E, Hansson HC, Hameri K, Svenningsson B, Massling A, McFiggans G, McMurry PH, Petaja T, Tunved P, Gysel M et al. . 2008. Hygroscopic properties of submicrometer atmospheric aerosol particles measured with H-TDMA instruments in various environments - a review. Tellus Series B-Chemical and Physical Meteorology 60(3):432-469.

Tang IN, Munkelwitz HR. 1994. Water Activities, Densities, and Refractive-Indexes of Aqueous Sulfates and Sodium-Nitrate Droplets of Atmospheric Importance. Journal of Geophysical Research-Atmospheres 99(D9):18801-18808.

Toon OB, Pollack JB, Khare BN. 1976. Optical-Constants of Several Atmospheric Aerosol Species - Ammonium-Sulfate, Aluminum-Oxide, and Sodium-Chloride. Journal of Geophysical Research-Oceans and Atmospheres 81(33):5733-5748.

Varma R, Moosmüller H, Arnott WP. 2003. Toward an ideal integrating nephelometer. Optics Letters 28(12):1007-1009.

Wang Y, Ma PL, Peng JF, Zhang RY, Jiang JH, Easter RC, Yung YL. 2018. Constraining Aging Processes of Black Carbon in the Community Atmosphere Model Using Environmental Chamber Measurements. Journal of Advances in Modeling Earth Systems 10(10):2514-2526.

Weingartner E, Burtscher H, Baltensperger U. 1997. Hygroscopic properties of carbon and diesel soot particles. Atmospheric Environment 31(15):2311-2327.

Zhou JC, Xu XZ, Zhao WX, Fang B, Liu QQ, Cai YQ, Zhang WJ, Venables DS, Chen WD. 2020. Simultaneous measurements of the relative-humidity-dependent aerosol light extinction, scattering, absorption, and single-scattering albedo with a humidified cavity-enhanced albedometer. Atmospheric Measurement Techniques 13(5):2623-2634.

3 Laboratory Study of Humidified Ammonium Sulfate and Nigrosin Aerosol Mixtures

Water vapor is one of the most important environmental influences with respect to atmospheric radiation transport as it can have significant effects on the optical properties of the aerosol. Water uptake can cause optical lensing effects – typically resulting in enhanced absorption and scattering – and it can modify the aerosol morphology. For example, absorption enhancements of up to three times have been predicted due to lensing effects, with even larger scattering enhancements, while morphological restructuring can enhance scattering by more than two times. A novel method for probing the single scattering albedo of aerosol exposed to high relative humidity environments has been developed. This system comprises a CAPS-PMssa monitor operating at 450 nm, a controlled humidification system, and an accurate humidity measurement. The change in a light-absorbing aerosol's brightness, which is quantified by the single scattering albedo (SSA), due to humidification is not very well understood. To study these effects, we studied two ammonium sulfate and nigrosin mixtures, as well as pure aerosol. It was found that SSA enhancements could be parameterized based on the volume fraction of nigrosin within the aerosol using a simple quadratic function. The hygroscopic and refractive of these aerosol were also investigated, and these were compared to established volume mixing rules.

3.1 Introduction

Aerosol interact with light in the atmosphere by scattering and absorbing light. An important factor in determining an aerosol's optical properties, and therefore how it interacts with radiation in the environment, is its composition. In the atmosphere, aerosol are composed of complex mixtures of chemical species that can make predicting the optical properties of these aerosol difficult. Complicating things further, an aerosol's hygroscopicity is dependent on the composition of the aerosol. At the same time, an aerosol's composition, and by extension its optical properties, is dependent on the aerosol's hygroscopicity and the relative humidity of the atmosphere. Organic aerosol

make up anywhere between 20-90% of aerosol mass in the atmosphere, a large fraction of which are water-soluble (Decesari et al. 2005; Kanakidou et al. 2005). Even still, organic aerosol can modify the hygroscopicity of inorganic species. Saxena et al. found that organics can enhance water uptake in rural settings (accounting for 25-40% of water uptake), while they can diminish water uptake in urban settings. Many studies have focused on determining the growth factors of humidified mixtures of organics and inorganics salts. Typically, the inclusion of organics with inorganics will allow for greater water uptake at lower RH values by shifting the deliquescence RH lower; however, is will also suppress the water uptake for higher RH (Cruz and Pandis 2000; Chan and Chan 2003). It is worth noting that little work has been done to look at how the optical properties of aerosol mixtures are affected at high humidity. Of particular interest is the optical properties of light-absorbing organics, such as black and brown carbon, when mixed with hygroscopic non-absorbing aerosol. Wetted black carbon aerosol could contribute a forcing change as high as 0.07 Wm^{-2} (Bond et al. 2013). These are the biggest contributors to aerosol light absorption in the atmosphere but are often relatively hydrophobic when freshly emitted (Weingartner et al. 1997). Aging and mixing with more hygroscopic aerosol, such as non-absorbing organic species like ammonium sulfate, could result in large changes in optical properties due to humidification. In this chapter, we will investigate such a case using a novel humidified albedometer using a well-characterized absorbing aerosol species (nigrosin) mixed with an atmospherically relevant and well-characterized non-absorbing species (ammonium sulfate). We will observe changes in single scattering albedo (SSA) and absorption as a function of relative humidity and develop parameterizations that can be applied to atmospherically relevant mixtures of aerosol.

3.1.1 Optical Enhancement Due to Humidification

Water can make up a significant portion of an aerosol's mass depending on the aerosol's hygroscopic properties and the relative humidity of the aerosol's environment. Due to the deliquescence-efflorescence hysteresis of many inorganic salts, the history of the aerosol

is also an important factor in determining an aerosol's water content. Changes in optical properties resulting from changes in RH can be expressed as a ratio:

$$f_{opt}[RH_{hi}, RH_{lo}, \lambda] = \frac{\sigma_{opt}[RH_{hi}, \lambda]}{\sigma_{opt}[RH_{lo}, \lambda]} \qquad \text{Equation 3.1}$$

where the subscript $_{opt}$ is used as a placeholder for one of the following optical properties: extinction (ext), scattering (sca), or absorption (abs) cross sections. Another common intensive parameter used to describe aerosol is the single scattering albedo (SSA), which is a ratio of the scattering and extinction cross sections. The change in SSA as a function of relative humidity can also be expressed as an enhancement ratio. Size increases lead to enhancements in scattering, which can lead to reduced visibility, especially in urban settings (Gupta et al. 2006; Zhang et al. 2010). Water also affects the morphology of the aerosol, coating the particles and changing their shape or composition with various (positive or negative) effects on their optical and radiative forcing properties (China et al. 2015; Wu et al. 2018). Many absorption methods, such as filter-based or photoacoustic, are fraught with biases at high RH (Arnott et al. 2003; Langridge et al. 2013). Quantifying how changes in RH can affect the optical properties of light-absorbing aerosol has remained an open challenge, and a lack of observational data for light-absorbing aerosol has contributed to the large uncertainty that aerosol is given in climate models (Cappa et al. 2012). For example, studies that assume a flat absorption response may overestimate SSA by as much as 0.05 (Redemann et al. 2001).

3.1.2 Morphology of internally mixed spheres

One way to model the optical properties of aerosol is Mie theory, which assumes a spherically symmetric aerosol. For some aerosol, this is not an accurate assumption. For example, freshly emitted soot has a fractal morphology, while mineral dust can exhibit irregular shapes when emitted. However, several aerosol species have morphologies that allow their optical properties to be closely approximated using Mie theory. The internal structure of humidified aerosol is an important consideration for accurate Mie calculations. Many models assume a homogenously mixed aerosol and calculate the

refractive index as volume weighted average of the refractive indices of individual components:

$$n_T = \sum_i \left(\frac{d_i}{d_T}\right)^3 \cdot ni \qquad \text{Equation 3.2}$$

where d_T and d_i are the volume equivalent diameters of the mixed particle and its individual components, respectively. The volume-weighted refractive index, n_T, can therefore be determined as a function of the refractive indices of each individual component, n_i. However, an individual aerosol may not be so well-mixed. For humidified aerosol that include solid and insoluble components such as soot, the components may be more distinct from each other. A common model for this is the core-shell model, where an insoluble core is surrounded by a liquid shell. Typically, the core is made to be strongly absorbing, like with soot, and the shell is made to be non-absorbing, like with sulfate.

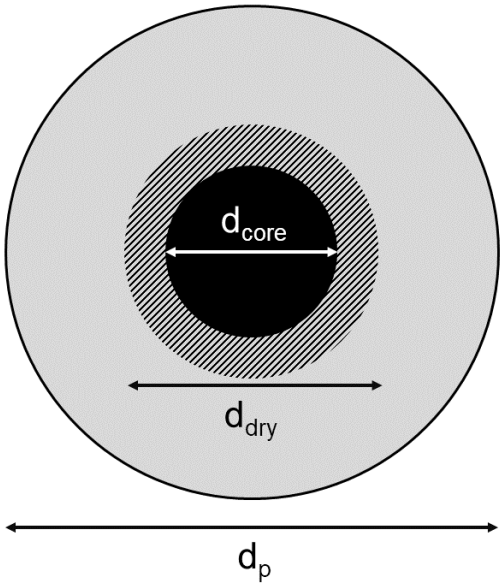

Figure 3.1: Diagram of the grey-shell model. The diameters depicted are as follows: d_p is the full diameter of the humidified aerosol, d_{dry} is the diameter of the aerosol prior to humidification, d_{core} is the undissolved remnant of the aerosol after humidification.

The grey-shell model refers to a model with a strongly absorbing core and slightly absorbing shell. This model has been used to describe soot coated in brown carbon, a less refractory organic compound that absorbs well in the UV, a system which has been found to have a net warming effect on the atmosphere (Saleh et al. 2014). A variation of the grey-shell model, depicted in Figure 3.1, can be conceived for water-soluble light-absorbing aerosol. For an aerosol of increasing diameter due to water uptake, the core will diminish in size according to its solubility:

$$d_{core}^3 = d_{dry}^3 - C(d_P^3 - d_{dry}^3) \qquad \text{Equation 3.3}$$

where d_p is the volume equivalent diameter of the aerosol, d_{dry} is the original diameter of the aerosol prior to humidification, and d_{core} is the diameter of the aerosol's core after humidification and dissolution. C is the solubility of the aerosol expressed as the volume dissolved per volume of water. In the context of an aerosol exposed to increasing relative humidity, as the core diminishes and aerosol diameter increases, the refractive index of the shell remains constant until the core is completely dissolved. This assumes the refractive index of the shell is determined by mixing the volume of dissolved core and volume of water in the shell. This volume ratio remains constant until the core is completely dissolved due to the dissolved fraction being dependent on the volume of water by C. As a result, changes in refractive index for multi-component cores only start occurring when one of the components become completely dissolved.

3.2 Experimental Methods

3.2.1 Experimental Setup

Aerosol were generated using a portable aerosol generator (TSI 3079A) and passed through two column-shaped desiccant diffusion driers containing silica gel beads (Droplet Measurement Technologies, Inc. ASSY 1110). The aerosol was then size selected using two methods in series to minimize the number of doubly charged particles within the sample. First, the aerosol was size selected based on the electric mobility using

a long column dynamic mobility analyzer (DMA, TSI Inc. 3080L) and an x-ray charge neutralizer (TSI 3087). A sheath flow of 10 lpm in the DMA was used for each experiment. Then the aerosol were size selected based on mass-to-charge ratio using the Centrifugal Particle Mass Analyzer (CPMA, Cambustion). The aerosol sample was then split between the H-CAPS-PM_{SSA} and either a CPC (TSI 3022A) or an additional SMPS (TSI 3938). This second SMPS consisted of a DMA (TSI 3081), neutralizer (TSI 3088), and a CPC (TSI 3750). The 3022A CPC was used during humidified aerosol experiments to quantify the particle concentration in the sample line and allowed for the calculation of the optical cross-sections of the aerosol. Size distributions measured by the SMPS were used in tandem with the H-CAPS-PM_{SSA} to determine the refractive indices of dry aerosol.

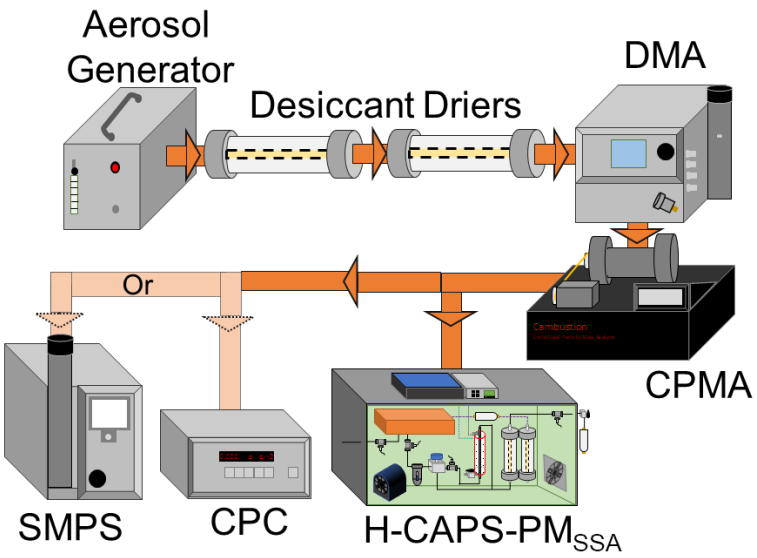

Figure 3.2: Setup used for experiments involving the determination the refractive index of aerosol mixtures at 450nm, as well as the humidification of aerosol mixtures. Generated aerosol are passed through two desiccant driers prior to being doubly size selected using an electrostatic classifier and centrifugal particle mass analyzer. The aerosol is then split between the humidified cavity attenuated phase-shift albedometer, condensation particle counter, and/or the scanning mobility particle sizer for measurement of optical properties, particle concentration, and particle size distribution, respectively.

3.2.2 Overview of Test Aerosol

We conducted experiments looking at the optical properties of aerosol composed of varying amounts of ammonium sulfate and nigrosin. Inorganic ammonium sulfate ($(NH_4)_2SO_4$) salt particles are atmospherically relevant and have high SSA. They are also highly hygroscopic, making it an important cloud condensation nucleus (CCN). Due the high SSA and hygroscopicity ammonium sulfate is used in the characterization and calibration of instrumentation that measure aerosol scattering and hygroscopicity. Nigrosin is an organic dye most often used for staining in biological microscopy. As an aerosol, nigrosin is strongly absorbing and can have an SSA values of 0.6 or less for smaller diameter particles. Due to these properties, nigrosin is often used as a soot surrogate when characterizing absorption measurement instrumentation. Nigrosin differs from soot in that it is slightly hygroscopic, whereas freshly emitted soot is hydrophobic. It is also spherical, which makes Mie-based optical models much more appropriate for calculating the optical properties than for soot to constrain in Mie-based optical models. Relevant properties of nigrosin and ammonium sulfate are listed in Table 3.1.

Table 3.1: Properties of aerosol components used in these experiments along with their Chemical Abstracts Service (CAS) registry number. Data sources are as listed: [1]chem.nlm.nih.gov, [2](Moteki et al. 2010), [3]sigmaaldrich.com, [4](Bluvshtein et al. 2017).

Aerosol	CAS #	ρ (g/cc)	C	M (g/mol)
Ammonium sulfate	7783-20-2	1.77[1]	0.432[1]	132.1[1]
Nigrosin	8005-03-6	1.60[2]	0.006[3,4]	616.5[1]

In the atmosphere, sulfates can modify the hygroscopicity of organic material when they are internally mixed. Such changes can affect the optical properties and atmospheric lifetime of organic aerosol. In the laboratory, mixtures of ammonium sulfate and nigrosin can be used to simulate mixtures of light-absorbing compounds with hygroscopic compounds in the lab. Several studies have implemented this approach, however they are often limited to testing mixing rules in relation to hygroscopicity (Flores et al. 2012; Langridge et al. 2013) and refractive index (Flores et al. 2012; Cotterell et al. 2020).

While Langridge et al. did perform absorption measurements, these were for the purpose of diagnosing RH dependent biases in the photoacoustic instrument (Langridge et al. 2013).

In addition to making measurements of pure ammonium sulfate and nigrosin, we also prepared two mixtures of these substances. The first mixture contained a 1:1 molar ratio of ammonium sulfate (AS:N=1.0) to nigrosin, while the second contained a 4.7:1 molar ratio (AS:N=4.7). The aerosol samples were prepared by weighing each aerosol component using a mass scale with resolution of 0.1 mg, and then mixing them with 100ml of milli-pore purified water. Aerosol samples containing nigrosin were then agitated in a sonication bath for a half-hour prior to humidification experiments to ensure complete dissolution.

3.2.3 Determination of Aerosol Refractive Indices

We determined the refractive index for each mixture of ammonium sulfate and nigrosin, as well as for pure nigrosin. Equipment issues prevented us from doing the same for pure ammonium sulfate; however, the refractive index of ammonium sulfate has been well characterized in several studies (Toon et al. 1976). Aerosol were mobility selected at 100nm, 200nm, and 300nm using a DMA, then mass selected using a CPMA, and finally, the optical properties were measured using the H-CAPS-PM_{SSA} running in its dry operational mode (RH<15% in the cavity). An additional SMPS, connected parallel to the H-CAPS-PM_{ssa}, was used to measure the size distribution of the aerosol sample. Each experiment was conducted separately based on selected size and aerosol species, accounting for 9 experiments in total. An experiment consisted of 5 or more size scans using the SMPS at a resolution of 64 channels per decade. Each experiment took between 10 and 15 minutes to complete. The H-CAPS-PM_{SSA} measured the extinction and scattering of the sample during the entire duration of each experiment. The refractive index is an important parameter for characterizing the aerosol and will be used in the determination of the aerosol's hygroscopic properties, as well as for optical modelling purposes.

3.2.4 Measurement of Humidified Mixtures

Humidification experiments were performed by sampling mobility and mass selected aerosol using the H-CAPS-PM_{SSA} and CPC in parallel. Aerosol flow was driven by these instruments, each of which had a pump. Initially, the aerosol was passed through the dry line in the H-CAPS-PM_{SSA} for five minutes. The relative humidity of these samples was usually less than 20%. Then a baseline check was performed by switching from the aerosol sample line to a line connected to room air via a HEPA filter. These baselines allowed us to account for any drift in the extinction and scattering signal. After the baseline check, aerosol was reintroduced into the sample line. Once the aerosol concentration stabilized after a minute or so, the H-CAPS-PM_{SSA} was set to operate in humid mode. This was performed by switching an actuated ball valve that diverted aerosol from the humidifier within the H-CAPS-PM_{SSA}. When the humidity measured immediately downstream of the H-CAPS-PM_{SSA} stabilized to around 50%, another baseline check was performed. Once aerosol was reintroduced, the relative humidity was ramped up. Baseline check were performed again when the relative humidity stabilized around 70% and 85%. Occasionally, another baseline was performed between these steps depending on the amount of time it was taking to ramp between 70% and 85%. After the 85% baseline check, the CAPS-PM_{SSA} collected data at high RH for another 5 minutes before ramping the relative humidity back downward. The ramp down occurred more quickly than the ramp up, so baseline checks were only performed before and after the ramp down. After the ramp down was complete, the H-CAPS-PM_{SSA} was switched back into dry operation and the aerosol sample was turned off.

3.3 Analysis and Results

3.3.1 Refractive Indices

For each experiment the concentration, N, at diameter D_p,was averaged for each of the scans made by the SMPS. The size distributions from aerosol of shared species but

different mass/mobility size selections were combined additively to create an aggregated size distribution:

$$N_{total}[D_p] = N_{100nm}[D_p] + N_{200nm}[D_p] + N_{300nm}[D_p] \qquad \text{Equation 3.4}$$

The H-CAPS-PM_{SSA} data was averaged over the 10- to 15-minute timespan that the SMPS was collecting data. The scattering was corrected for size-dependent truncation bias using our custom Mie truncation estimation software written in Python. We found in Chapter 2 that this software could be used to accurately determine the truncation bias using an empirical relationship. Uncertainties in the scattering and extinction measurement were determined using the uncertainties reported for the CAPS-PM_{SSA} by Onasch et al. (Onasch et al. 2015). The absorption was determined by taking the difference between extinction and scattering, and the uncertainties were propagated accordingly. The averaged optical properties for all three sizes of an aerosol species were then combined additively in a similar fashion to the size distribution data.

The refractive indices of the aerosol were determined analytically using a grid search algorithm similar to that employed by Cottrell et al. (Cotterell et al. 2020). We focused the real part of the grid in the range $1.4 \leq n \leq 1.7$ and imaginary part of the grid in the range $0.0 \leq k \leq 0.3$. The step size used to generate the grid was 0.001 for both n and k. A grid of complex refractive indices was then generated based on these input parameters. Subsequently, Mie calculations were performed to generate grids for the optical properties of the aerosol sample using the measured size distribution and the refractive index grid. The Mie calculations were performed using PyMieScatt , a Mie calculation routine written in Python and based on the Bohren-Huffman algorithm (Bohren and Huffman 1998; Sumlin et al. 2018). The Mie estimated extinction and SSA were then compared to the measured values and their uncertainties using the χ^2 statistical parameter. The refractive index is then determined by selecting the complex refractive index that yielded the smallest combined χ^2:

$$\chi^2_{comb.}[i_n, i_k] = \chi^2_{ext}[i_n, i_k] + \chi^2_{SSA}[i_n, i_k] \qquad \text{Equation 3.5}$$

where i_n and i_k are the positions within the grid. The χ^2 values are then defined as:

$$\chi^2_{ext}[i_n, i_k] = \frac{\left(B_{ext,meas}[i_n, i_k] - B_{ext,mie}[i_n, i_k]\right)^2}{\sigma^2_{ext,meas}}$$

$$\chi^2_{SSA}[i_n, i_k] = \frac{(\omega_{meas}[i_n, i_k] - \omega_{mie}[i_n, i_k])^2}{\sigma^2_{\omega,meas}[i_n, i_k]}$$

Equation 3.6

The uncertainty is determined by finding the range of refractive index values that fall within 1-σ on the χ^2 distribution, or $\chi^2 \geq \chi^2_{comb.,\ min} + 2.28$ for a dataset with two degrees of freedom. In Table 3.2, we report the real and imaginary components of the refractive index and compare these values to volume averaged values of the expected ammonium sulfate refractive indices and the measured refractive index of pure nigrosin.

Table 3.2: Comparison of the real (n) and imaginary (k) refractive indices at 450nm for measured values and those calculated from volume mixing rules from the literature value for ammonium sulfate (Toon et al. 1976) and the measured value for nigrosin. Uncertainties for each value are reported in parentheses.

Aerosol	$\boldsymbol{n_{meas}}$	$\boldsymbol{n_{vol}}$	$\boldsymbol{k_{meas}}$	$\boldsymbol{k_{vol}}$
Ammonium sulfate	--	1.53 (0.01)	--	$10^{-7}(10^{-7})$
AS:N = 4.7	1.56(0.03)	1.58 (0.02)	0.07 (0.02)	0.08 (0.02)
AS:N = 1.0	1.61(0.04)	1.62 (0.03)	0.12 (0.02)	0.13 (0.03)
Nigrosin	1.63(0.04)	1.63 (0.04)	0.16 (0.03)	0.16 (0.03)

For the ammonium sulfate nigrosin mixtures, the volume averaged values were in good agreement with the values measured directly. However, for both mixtures, the volume-averaged values were slightly higher than the measured values. The measured values for pure nigrosin are in good agreement with other studies that have been conducted on similar wavelength ranges. Liu et al. (Liu et al. 2013) characterized their ellipsometry instrument for use with organic compounds using nigrosin and found a refractive index of 1.63+0.13j at 450nm. Cotterell et al. (Cotterell et al. 2020), as well as Radney and Zangmeister (Radney and Zangmeister 2015), measured the complex refractive index at 405nm and found refractive indices of 1.61+0.16j and 1.63+0.18j, respectively. These values were in better agreement with our results but had a lower real refractive index and

higher imaginary part than the values measured by Liu et al. (Liu et al. 2013) at 405nm (1.67+0.11j). Nigrosin is a manufactured product, and it is entirely possible that measured refractive indices are dependent on the lot number.

3.3.2 Determination of Hygroscopic Properties

Despite efforts to keep the sample line between the humidifier and the CAPS-PM_{SSA} isothermal, higher relative humidity values are observed upstream of the CAPS-PM_{SSA} (Carrico et al. 2021). As a result, deliquescence is typically observed below value reported in literature. For example, the deliquescence point of ammonium sulfate is observed at $RH = 65\%$ as opposed to the expected value of $RH = 81\%$ (Tang and Munkelwitz 1994; Onasch et al. 1999). The deliquescence of the AS:N=4.7 mixture was observed at $RH = 69\%$, while the AS:N=1.0 mixture and nigrosin exhibit deliquescence. The focus of our analysis will then be on RH values greater than 70% where the aerosol are all expected to be hydrated. The optical properties measured using the H-CAPS-PM_{SSA} were bin averaged based on their relative humidity values, and the bin sizes were chosen to be centered on integer values of RH and have an RH width of 1%. Additionally, differences in losses due to aerosol deposition have not fully been characterized between the dry line and the humid line of the H-CAPS-PM_{SSA}. As a result, optical enhancements are calculated by referencing optical measurements at $RH_{ref} = 53\%$. This value was chosen because it was the lowest stable RH across all experiments.

The hygroscopic parameter was determined as a function of RH for each experiment from the extinction enhancement data. We refer to the hygroscopic parameter determined using this method as the extinction hygroscopic parameter, or κ_{ext}. Least-squares minimization and Mie calculations were used to determine the κ_{ext} value that best predicted the measured extinction enhancements. This was performed by first estimating the growth factor using a test κ value, then estimating the extinction from that growth factor using PyMieScatt. This was performed until the κ_{ext} that minimized the χ^2 statistic was determined:

$$\chi^2 = \frac{\left(f_{ext,Mie} - f_{ext,Meas.}\right)^2}{\sigma_{fext}^2} \qquad \text{Equation 3.7}$$

where σ_{fext}^2 is the uncertainty in the measured extinction enhancement. For each RH delineated extinction measurement, Monte Carlo simulations of extinction were performed to estimate the uncertainty of the κ_{ext}. Each simulation consisted of randomly generating an extinction enhancement, aerosol refractive index, and relative humidity from their measured values and their uncertainties. The measured enhancement, refractive index, and humidity were assumed to have Gaussian uncertainty, and the randomly generated values were generated using the measured value and uncertainty as a seed in a Gaussian weighted random number generator. These simulations were performed alongside the least-squares regression to estimate κ_{ext} for the randomly generated f_{ext} values. Onasch et al. found that extinction measurements using the CAPS-PM_{SSA} have an uncertainty of 5% (Onasch et al. 2015). The uncertainty in f_{ext} is about 7% as determined from basic error propagation. Each κ value was determined by averaging the results of 100 simulations and using the standard error of all simulations as a measure of uncertainty.

As can be seen from Figure 3.3, κ_{ext} varied as a function of RH. To accurately estimate $\kappa_{ext}[RH]$, we had to first estimate κ_{ext} at $RH_{ref} = 53\%$. For ammonium sulfate, since RH_{ref} was less than the observed deliquescence RH, it is safe to assume $\kappa_{ext}[53\%] = 0$ for ammonium sulfate. However, the same assumption might not hold for other aerosol types. Estimation of $\kappa_{ext}[53\%]$ was performed by first guessing the value of $\kappa_{ext}[53\%]$ and running the κ_{ext} determination code to determine κ_{ext} for every measured f_{ext} between 54%≤RH≤65%. Linear regression was then used to estimate $\kappa_{ext}[53\%]$ by fitting κ_{ext} and extrapolating the resulting fit to 53%. This was performed iteratively until $\kappa_{ext}[53\%]$ remained unchanged. The results from Figure 3.3 for κ_{ext} [70%] and κ_{ext} [85%], as well as the reference value $\kappa_{ext}[53\%]$, are summarized in Table 3.3. The κ_{ext} values for pure aerosol agree with those reported in the literature. Hygroscopic parameter, κ_{ext}, were estimated from growth factors from Flores et al. to be 0.10±0.02 and

0.10±0.05 at RH = 80% and 90%, respectively (Flores et al. 2012). Hygroscopic parameter estimated from growth factors in Brem et al. was on the lower end of our reported uncertainty ranges at κ=0.05 (Brem et al. 2012). This growth factor was based on the assumption that scattering is linearly dependent on volume for small particles and may underestimate the κ values as a result. For ammonium sulfate, Petters and Kreidenweis suggests a range of 0.33 to 0.72 derived from hygroscopic parameters (Petters and Kreidenweis 2007). Using an H-TDMA to measure growth factors and infer κ values, Hansen et al. found κ in the range of 0.45 to 0.58 for ammonium sulfate at RH=85%. The $\kappa_{ext}[RH]$ for pure ammonium sulfate and both mixtures were found to decrease with increasing RH. This trend is consistent with previous measurements and is also predicted by the Aerosol Inorganic Model (Clegg et al. 1998; Royalty et al. 2017).

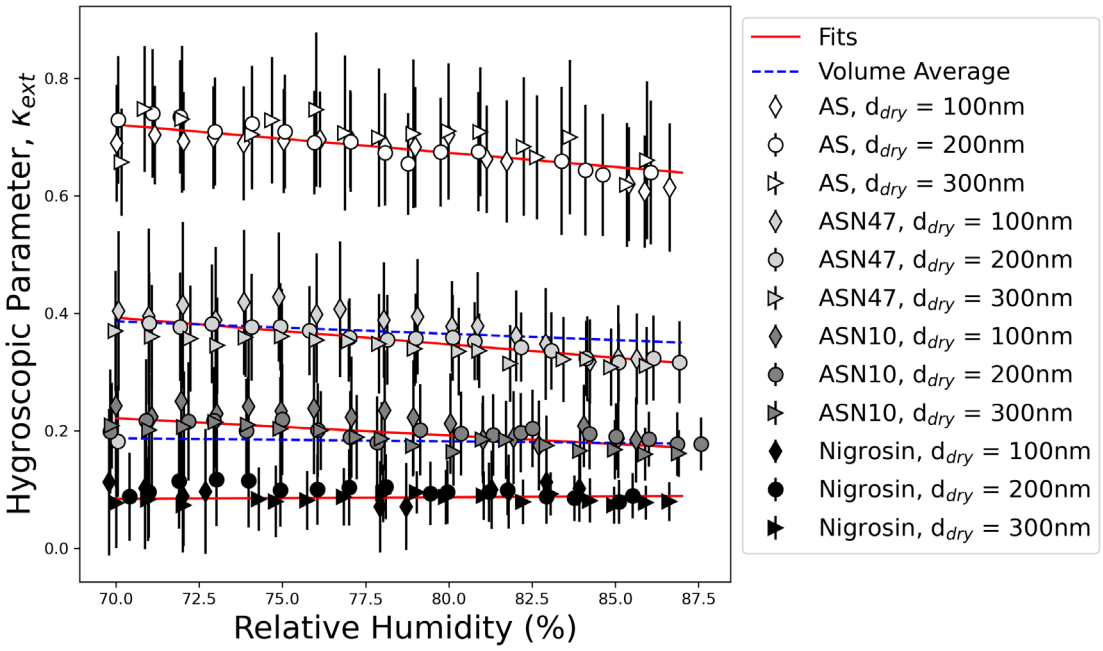

Figure 3.3: Hygroscopic parameter, κ, determined for RH greater than 70% for each experiment. Diamonds (♦), dots (●), and triangles (▶) are used to represent data size selected at 100nm, 200nm, and 300nm, respectively. In addition, the darkness of the marker colors increases with increasing Nigrosin fraction. Linear regression was used to determine the red lines, while volume averages of the κ-fits for both mixtures are represented by dashed blue lines.

The hygroscopic parameter, κ, was originally intended as a singular descriptor of aerosol hygroscopicity. The decreasing trend of κ_{ext} as a RH increases suggests that either the κ-Köhler theory fails as a single parameter descriptor of aerosol or the derivation of κ from extinction data is prone to RH dependent biases. The former possibility is suggested by Lewis, as his analysis of Köhler theory suggests κ decreases as a solute becomes more diluted in a droplet at RH below 95% (Lewis 2008).

Table 3.3:Hygroscopic parameters determined for RH=70% and RH=85% as well as the hygroscopic parameter used for reference at RH=53%. Uncertainties for each value are given in parentheses.

Aerosol	$\boldsymbol{d_p}$	$\boldsymbol{\kappa}$[53%]	$\boldsymbol{\kappa}$[70%]	$\boldsymbol{\kappa}$[85%]
Ammonium sulfate	100	0	0.69 (0.10)	0.61 (0.10)
	200		0.73 (0.11)	0.64 (0.10)
	300		0.66 (0.09)	0.62 (0.11)
AS:N = 4.7	100	0.05 (0.03)	0.40 (0.14)	0.32 (0.08)
	200		0.38 (0.09)	0.32 (0.07)
	300		0.37 (0.10)	0.31 (0.07)
AS:N = 1.0	100	0.14 (0.06)	0.24 (0.14)	0.19 (0.07)
	200		0.20 (0.11)	0.19 (0.06)
	300		0.21 (0.07)	0.17 (0.05)
Nigrosin	100	0.08 (0.01)	0.11 (0.13)	0.10 (0.06)
	200		0.09 (0.07)	0.09 (0.04)
	300		0.08 (0.08)	0.07 (0.03)

Petters and Kreidenweis suggest that κ can be predicted for multicomponent aerosol using volume weighted averages of each component's κ-value (Petters and Kreidenweis 2007). The hygroscopic parameter for the AS:N=1.0 mixture is in good agreement with those calculated from Flores et al, which was found to be 0.27±0.02 and 0.23±0.01 at RH=80% and 90%, respectively. Volume weighted averages were applied to the trendlines for ammonium sulfate and nigrosin. The volume weighted averages predicted

the hygroscopic properties of the mixtures well. However, the slopes of the volume weighted averages were quite different from the trendlines estimated for the mixtures. Interestingly, the estimated κ-values for the mixtures at RH=53% do not follow these volume mixing rules, as the AS:N=1.0 mixture had the highest estimated κ at RH=53%. For both mixtures, optical enhancements were greater than the optical enhancements of both pure aerosol at relative humidity values below 70%.

3.3.3 Single Scattering Albedo of Humidified Aerosol

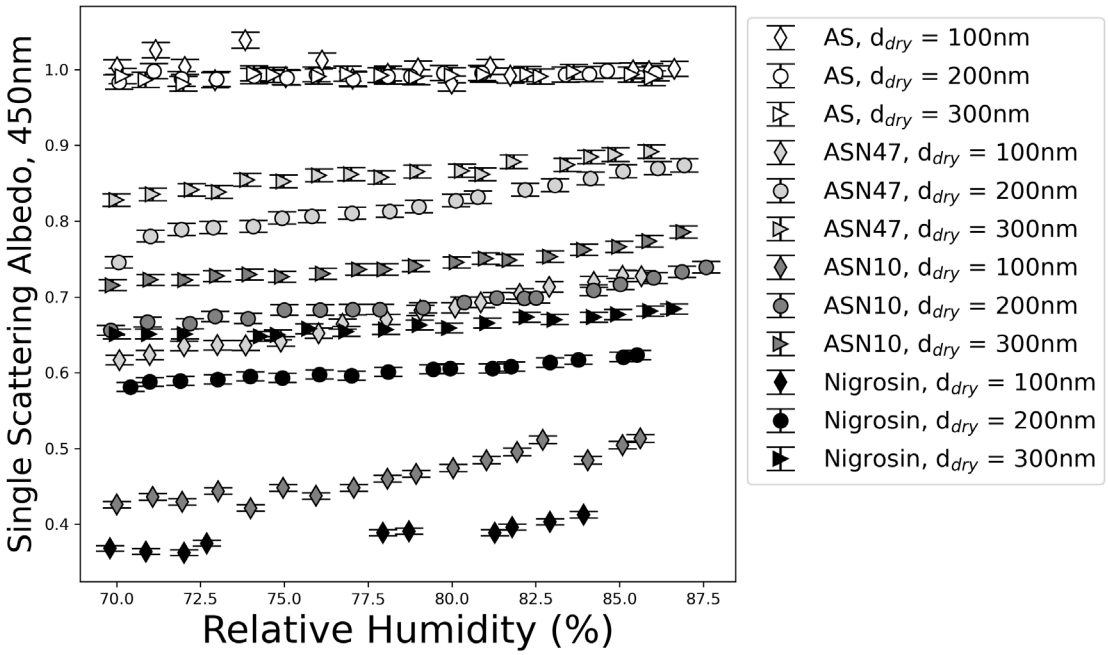

Figure 3.4: Single scattering albedo measured for relative humidity values greater than 70%. Marker shape and color scheme follow the same convention as Figure 3.3.

The H-CAPS-PM_{SSA} is uniquely capable of measuring the SSA of humidified aerosol to within 1%. It is also capable of inferring absorption using the extinction minus scattering (EMS) method. One limitation of the H-CAPS-$PM_{SSA,}$ and a primary source of uncertainty in the SSA measurement, is size-dependent truncation of the scattering phase-function. In Chapter 2, we showed two methods for correcting size-dependent truncation biases and found that for humidified aerosol, the best method was to use an empirical

relation based on estimated aerosol diameter. The empirical relation was determined from three aerosol species: nigrosin, poly-styrene latex spheres, and ammonium sulfate. The real and imaginary refractive index ranges that these aerosol cover are 1.53-1.63 and 0.00-0.17, respectively. Since the correction scheme compared favorably to hydrated ammonium sulfate aerosol, we apply the same correction scheme here as well. SSA calculated using corrected scattering measurements for each experiment is shown in Figure 3.4. Unsurprisingly, the SSA of each aerosol type increased as RH increased. The greatest overall change in aerosol SSA was observed for the mixtures, while the lowest change observed was for ammonium sulfate.

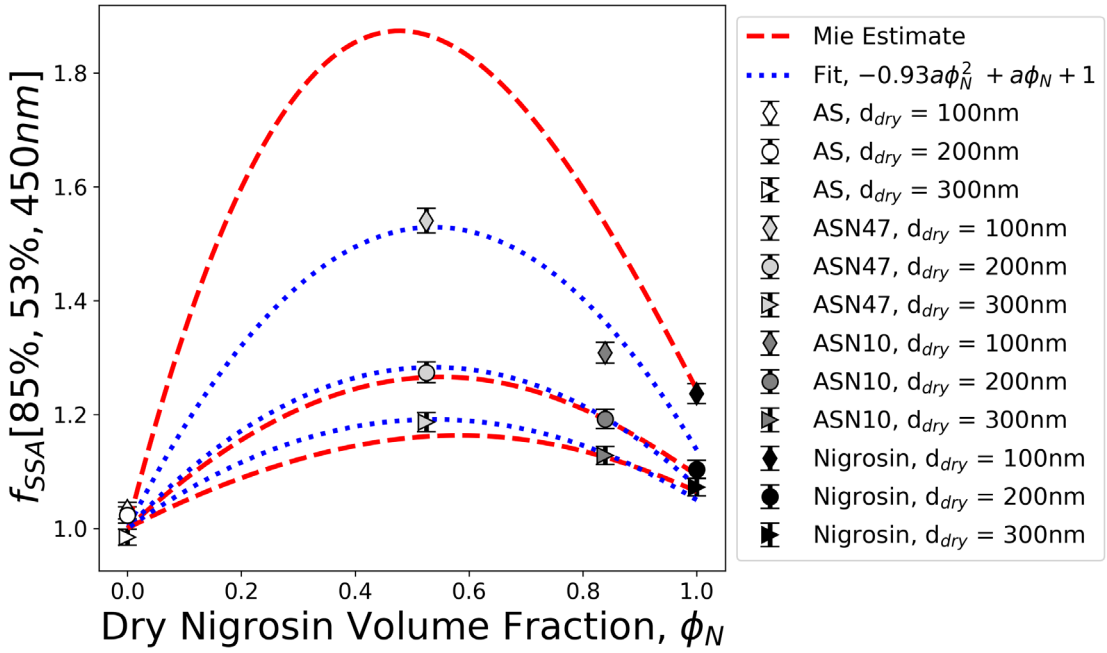

Figure 3.5: The albedo enhancement at RH=85% is dependent on the volume fraction of nigrosin in the aerosol. The enhancements for volume fractions ranging from 0 to 1.0 were estimated using Mie calculations and volume mixing rules for refractive indices and κ. A quadratic fitting function was used to find an empirical relation for the SSA enhancement. The fitting parameters are found to be dependent on the difference in RH values used to calculate f_{SSA} as well as the dry diameter of the aerosol.

The SSA of ammonium sulfate is not expected to change for two reasons: 1) Water will not increase the absorption of ammonium sulfate by a measurable amount, and 2) The

SSA of ammonium sulfate cannot increase because it is already near 1.0. The enhancements, $f_{SSA} = SSA[RH]/SSA[53\%]$, is seen to be both aerosol- and size-dependent. Smaller size aerosol tends to have the greatest enhancements, owing in large part to having a lower SSA at RH=53%. The AS:N=4.7 mixture has the highest enhancement (1.49) when compared to other aerosol of similar size, followed by the AS:N=1.0 mixture and the pure nigrosin aerosol. This is depicted in Figure 3.5, where we compare measured values of $f_{SSA}[85\%, 53\%]$ to Mie theory applied to aerosol with varying degrees of nigrosin volume fraction, $\phi_N = V_N/(V_{AS} + V_N)$. When $\phi_N = 0$, $f_{SSA} = 1$ due to the SSA of ammonium sulfate already being near 1.0. When $\phi_N = 1$, there will be a modest enhancement in SSA due to nigrosin's low SSA and hygroscopicity. Increasing the amount of ammonium sulfate in the aerosol result in two effects: increased $SSA\left[RH_{ref}\right]$ and increased water uptake which will result in increased $SSA[RH]$.

If $SSA\left[RH_{ref}\right]$ becomes close to 1.0, it starts to limit the amount of SSA enhancement because $SSA[RH]$ cannot be greater than 1.0. This results in a curved shape with minima at $\phi_N = 0,1$ and a maximum somewhere in the range $0 < \phi_N < 1.0$. As a result, we developed a quadratic empirical model to describe the SSA enhancement as a function of nigrosin volume fraction:

$$f_{SSA}\left[RH, RH_{ref}, 450nm\right] = -0.93a\phi_N^2 + a\phi_N + 1 \qquad \text{Equation 3.8}$$

where a is the fitting parameter related to the relative humidity and dry aerosol diameter by:

$$a = (5.5 \pm 0.1) \times \frac{RH - RH_{ref}}{d_{dry}} \qquad \text{Equation 3.9}$$

These values were calculated by fitting Equation 3.8 to measured data for measurements with RH>70% and then using linear regression to determine their dependence on the difference in RH and dry diameter. The linear regression yielded high coefficients of determination, with $R_a^2 = 0.98$, indicating a strong correlation between the fit parameters and the ratio of the difference in RH and the dry diameter. Similar methods have been

developed that parameterize scattering enhancements based on the organic carbon to ammonium sulfate ratio (Malm et al. 2005; Orozco et al. 2016). In contrast, this empirical model could be used to estimate the change in SSA of atmospherically relevant light-absorbing species, such as water-soluble organics, resulting from water uptake. There is good agreement between Mie Theory and measurements for the 200 and 300nm size selected aerosol but poor agreement with the 100nm size-selected aerosol. This discrepancy could be the result of the size distribution of the 100nm sample not being truly monodisperse, as is assumed by the Mie model. The change in optical efficiency is much greater between 100nm and 200nm than it is for aerosol between 200nm and 300nm. This means that the presence of larger aerosol can have an outsized effect on the SSA enhancement for aerosol size selected for 100nm as compared to those size selected at 200nm or 300nm. In addition, comparisons of this approach to Mie simulated aerosol suggest that the approach may be limited to fine-mode aerosol of diameters less than 500nm. Beyond this range, the dependence of a on dry diameter and humidity will diverge from that given in Equation 3.9.

3.3.4 Absorption Enhancements of Humidified Aerosol

Absorption was calculated using the Extinction minus Scattering (EMS) method after scattering had been corrected for size-dependent truncation biases. In Figure 3.6 we parameterized f_{abs}(RH, 53%) as a function of $f_{sca}(RH, 53\%)$ using linear fits. The fit parameters and their uncertainties are reported in Table 3.4. Due to the difficulty of measuring f_{abs} and the lack of instrumentation available that can perform the measurement, this parameterization could be used to compliment scattering enhancement measurements made using nephelometer. For each panel in Figure 3.6, the data was averaged into 12 equal sized bins based on f_{sca} to show the trends more clearly. We report the absorption enhancements for the AS:N=4.7 and AS:N=1.0 in Panels a) and b), respectively. The mixtures' f_{abs} increase with increasing f_{sca} initially, and then they either flatten out or begin to decrease with increasing f_{sca}.

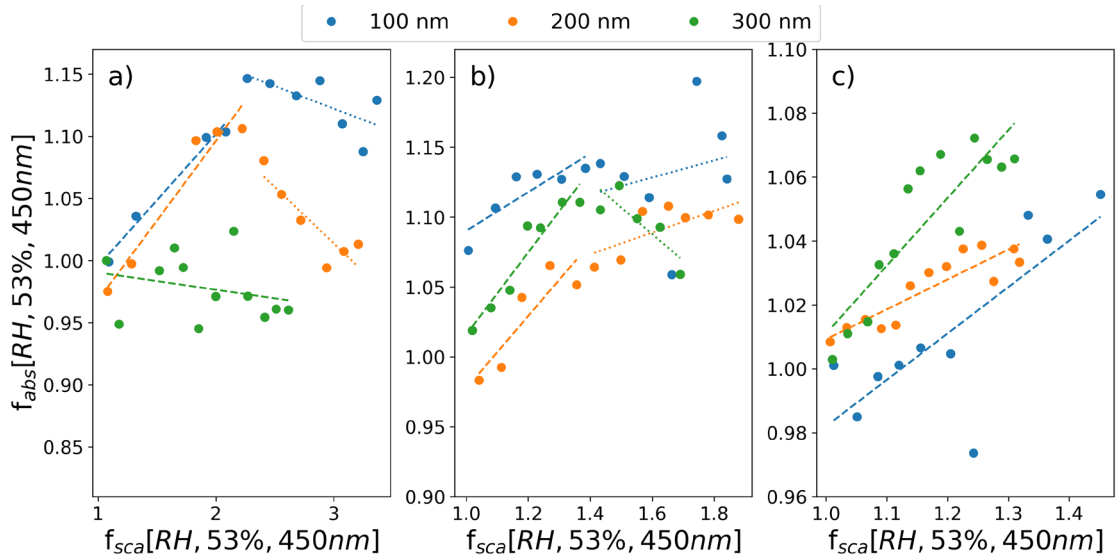

Figure 3.6: Measured absorption enhancements plotted against scattering enhancements for a) AS:N=4.7 mixture, b) AS:N=1.0 mixture, and c) pure nigrosin. Each plot is delineated by the size selected dry diameter using blue (100nm), orange(200nm), and green (300nm) markers. Linear regression is performed on each plot to parameterize absorption enhancement as a function of scattering enhancement. The results of this parameterization of reported in Table 3.4.

The mixtures are therefore represented with two linear functions, with the exception of the 300nm AS:N=4.7 dataset. The piecewise relationship was not found to carry over for the pure nigrosin, shown in Panel c). The absorption enhancement of pure nigrosin is dependent on the dry diameter of the aerosol, which is shown to a greater degree in Figure 9 of the instrumental paper by Carrico et al. (Carrico et al. 2021). We do not report the values for ammonium sulfate here, as the H-CAPS-PM_{SSA} is not sensitive enough to detect changes in absorption for hydrated ammonium sulfate aerosol.

The low solubility of nigrosin (see Table 3.1) suggests that the morphology of humidified nigrosin would be that of a core-shell configuration with a core of pure nigrosin and a slightly absorbing shell. However, comparisons with Mie theory shown in Figure 3.7 suggest the nigrosin may be more evenly dispersed. It is unclear if this means the solubility of nigrosin is higher than manufacturer specifications at such small sizes or if the nis being more evenly dispersed throughout the aerosol without dissolution (i.e.

fragmentation). Furthermore, decreasing f_{abs} with increasing f_{sca} observed for the AS:N=4.7 mixture is not predicted by volume mixing, core-shell, or grey-shell models. This could be indicative of some morphological changes occurring within the aerosol when enough water becomes present within the aerosol.

Table 3.4: Parameterization of the fits from Figure 3.6 using the linear model $f_{sca} = m \cdot f_{abs} + c$ for scattering enhancements above and below the enhancement cutoff (f_{cut}) by aerosol species and diameter (d_p) also listed.

			$f < f_{cut}$		$f > f_{cut}$	
	d_p (nm)	f_{cut}	m	c	m	c
ASN47	100	2.25	0.10 (0.01)	0.88 (0.02)	-0.04 (0.02)	1.23 (0.05)
	200	2.25	0.12 (0.02)	0.83 (0.03)	-0.09 (0.02)	1.29 (0.07)
	300	0	-	-	-0.01 (0.02)	1.00 (0.03)
ASN10	100	1.4	0.13 (0.04)	0.95 (0.05)	0.06 (0.12)	1.03 (0.20)
	200	1.4	0.25 (0.08)	0.71 (0.10)	0.08 (0.03)	0.96 (0.06)
	300	1.4	0.29 (0.04)	0.72 (0.05)	-0.19 (0.07)	1.39 (0.11)
Nigrosin	100	0	-	-	0.14 (0.04)	0.84 (0.05)
	200	0	-	-	0.09 (0.01)	0.92 (0.02)
	300	0	-	-	0.21 (0.04)	0.80 (0.04)

Compaction of the aerosol from a fractal to a more spherical aerosol is an unlikely explanation, as nigrosin is unlikely to form aggregates (Presser 2012). One potential explanation is that the ammonium sulfate and nigrosin mixture forms a core-shell structure with nigrosin on the outside and aqueous ammonium sulfate on the inside. Absorption enhancements greater than 1.0 are not expected from Mie calculations from this morphology, so the only explanation for the decrease in enhancements seen in panel b) would be a restructuring of the aerosol from a core-shell morphology with nigrosin making up the core to a core-shell morphology with aqueous ammonium sulfate making up the core. There is evidence of core-shell morphologies comprised of organic shells and

aqueous inorganic cores that readily take up water (Robinson et al. 2013). However, nigrosin is a solid, and such morphology has only been observed for liquid organic shells where the diffusion of water through the shell is rapid. Of course, any discussion of morphology is purely speculative, and more work is necessary to understand how these mixtures behave at high relative humidity.

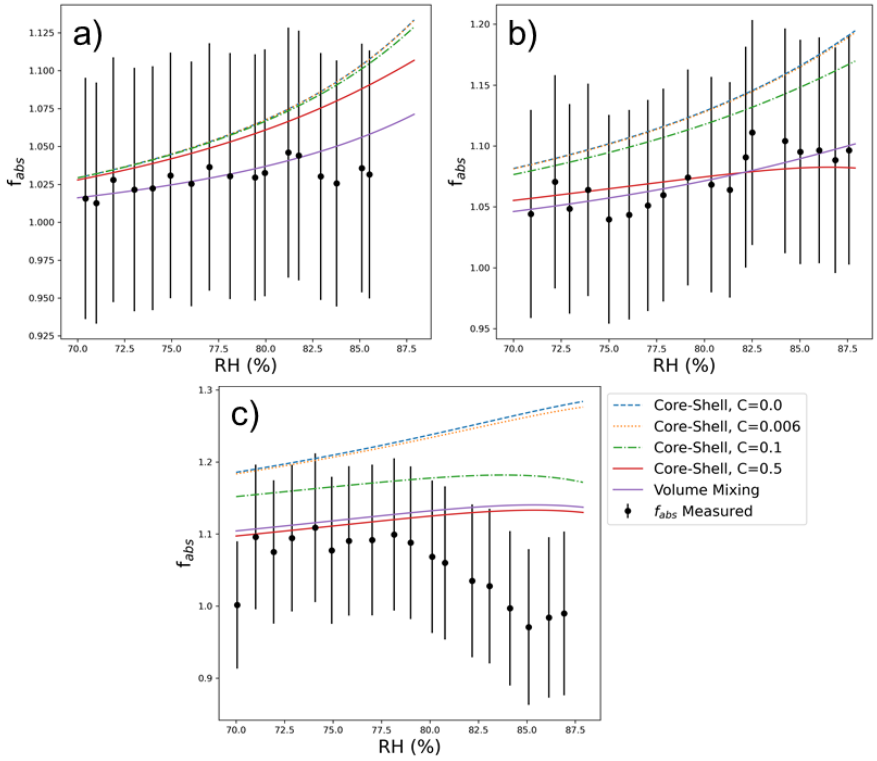

Figure 3.7: Comparison of measured absorption enhancements to Mie calculations as a function of relative humidity. These plots show data for: a) Nigrosin, b) AS:N=1.0, and c) AS:N=4.7 size selected at 200nm. The Mie calculations include core-shell calculations with varying levels of solubility as well as a calculation that assumes the aerosol is homogenously mixed (Volume Mixing).

Another possibility for decreasing absorption enhancements is that truncation is being overcorrected, especially for the larger sizes. The correction scheme, described in more detail in Chapter 2, operates under the assumption that the truncation dependence on refractive index is negligible for these aerosol, and the inclusion of water to absorbing aerosol might be one condition where that assumption falls apart. Apart from the

humidified ammonium sulfate, whose SSA should not deviate from 1.0 in a humid environment, it is especially difficult to quantify the truncation of these aerosol. As shown in Chapter 2, estimating this truncation using Mie theory will consistently underestimate truncation. In addition, the quantifying of the truncation of absorbing aerosol within the CAPS-PM_{SSA} requires simultaneous measurement of the aerosol's absorption. We performed this in Chapter 2 using a three-wavelength photoacoustic instrument; however, large uncertainties are associated with this as the absorption is being performed on a separate volume of aerosol at different wavelengths. In addition, to quantify the absorption of humidified light-absorbing aerosol would require simultaneous measurement of absorption at the same humidity, a measurement that is not possible using photoacoustic or filter-based absorption measurement techniques (Arnott et al. 2003; Langridge et al. 2013).

3.4 Summary and Conclusion

The optical and hygroscopic properties of aerosol containing varying amounts of ammonium sulfate and nigrosin have been investigated with the humidified cavity attenuated phase-shift albedometer (H-CAPS-PM_{SSA}). The optical and hygroscopic properties each aerosol species was found to be dependent on the volume fraction of nigrosin and ammonium sulfate. Mixing rules were found to closely predict both the refractive indices and the hygroscopic parameter, κ_{ext}, inferred from extinction and scattering data for each of the mixtures. However, the mixing rules failed to predict the hygroscopic parameters of the aerosol below the deliquescence of ammonium sulfate. These findings suggests that the mixing rules for κ should only be implemented for hydrated aerosol. Additionally, the slope of the hygroscopic parameter inferred from extinction data was steeper than that predicted from volume mixing. It is possible that volume mixing may not be very predictive of κ at higher relative humidity values for mixtures of ammonium sulfate and nigrosin.

The H-CAPS-PM_{SSA} sets itself apart from other instruments in that it can quantify changes in albedo as a function of relative humidity to within 1% accuracy. Using the instrument, inferences can therefore be made about an aerosol's absorption. We carried out experiments on aerosol containing different fractions of ammonium sulfate and nigrosin because they have been well characterized in previous lab studies and could provide a framework for conducting future studies on humidified mixtures of organics and ammonium sulfate. We successfully parameterized the enhancement in an aerosol's albedo because of humidification using a quadratic relation with the volumetric mixing ratio of nigrosin as the independent variable. Mie estimates of this parameterization showed stronger agreement with the 200nm and 300nm datasets than for the 100nm datasets and suggest the ideal diameter range for this parameterization is 200-500 nm. A parabolic function could still be applied beyond this range, according to Mie calculations; however, the diameter need be parameterized differently outside the 200-500 nm range. Similar volumetric parameterization schemes, or those involving ratios of organic carbon to elemental carbon, can be determined for atmospherically relevant aerosol for use in climate models. Absorption enhancement was also parameterized in terms of scattering enhancements, and it was found that absorption enhancement was related to scattering enhancement via linear, or piecewise linear, functions. The H-CAPS-PM_{SSA} technology is relatively new, and it could be some time before enough in situ field measurements are performed to inform climate models. In the meantime, future work should focus on the study of atmospherically relevant mixtures in controlled laboratory experiments. This work could be meaningful not just for climate models, but for field campaigns during which is not feasible to deploy a humidified albedometer, like the H-CAPS-PM_{SSA}. The results of experiments on known mixtures of prominent atmospheric species can be applied to measurements in the atmosphere that include the determination of atmospheric species present as well as the optical properties of aerosol.

3.5 References

Arnott WP, Moosmuller H, Sheridan PJ, Ogren JA, Raspet R, Slaton WV, Hand JL, Kreidenweis SM, Collett JL. 2003. Photoacoustic and filter-based ambient aerosol light absorption measurements: Instrument comparisons and the role of relative humidity. Journal of Geophysical Research-Atmospheres 108(D1).

Bluvshtein N, Flores JM, He QF, Segre E, Segev L, Hong NN, Donohue A, Hilfiker JN, Rudich Y. 2017. Calibration of a multi-pass photoacoustic spectrometer cell using light-absorbing aerosols. Atmospheric Measurement Techniques 10(3):1203-1213.

Bohren CF, Huffman DR. 1998. Absorption and Scattering of Light by Small Particles. Wiley.

Bond TC, Doherty SJ, Fahey DW, Forster PM, Berntsen T, DeAngelo BJ, Flanner MG, Ghan S, Karcher B, Koch D et al. . 2013. Bounding the role of black carbon in the climate system: A scientific assessment. Journal of Geophysical Research-Atmospheres 118(11):5380-5552.

Brem BT, Gonzalez FCM, Meyers SR, Bond TC, Rood MJ. 2012. Laboratory-Measured Optical Properties of Inorganic and Organic Aerosols at Relative Humidities up to 95%. Aerosol Science and Technology 46(2):178-190.

Cappa CD, Onasch TB, Massoli P, Worsnop DR, Bates TS, Cross ES, Davidovits P, Hakala J, Hayden KL, Jobson BT et al. . 2012. Radiative Absorption Enhancements Due to the Mixing State of Atmospheric Black Carbon. Science 337(6098):1078-1081.

Carrico CM, Capek TJ, Gorkowski KJ, Lam JT, Gulick S, Karacaoglu J, Lee JE, Dungan C, Aiken AC, Onasch TB et al. . 2021. Humidified Single Scattering Albedometer (H-CAPS-PMSSA): Design, Data-Analysis, and Validation. Aerosol Science and Technology:1-25.

Chan MN, Chan CK. 2003. Hygroscopic properties of two model humic-like substances and their mixtures with inorganics of atmospheric importance. Environmental Science & Technology 37(22):5109-5115.

China S, Scarnato B, Owen RC, Zhang B, Ampadu MT, Kumar S, Dzepina K, Dziobak MP, Fialho P, Perlinger JA et al. . 2015. Morphology and mixing state of aged soot particles at a remote marine free troposphere site: Implications for optical properties. Geophysical Research Letters 42(4):1243-1250.

Clegg SL, Brimblecombe P, Wexler AS. 1998. Thermodynamic model of the system H+-NH4+-Na+-SO42--NB3--Cl--H2O at 298.15 K. Journal of Physical Chemistry A 102(12):2155-2171.

Cotterell MI, Szpek K, Haywood JM, Langridge JM. 2020. Sensitivity and accuracy of refractive index retrievals from measured extinction and absorption cross sections for mobility-selected internally mixed light absorbing aerosols. Aerosol Science and Technology 54(9):1034-1057.

Cruz CN, Pandis SN. 2000. Deliquescence and Hygroscopic Growth of Mixed Inorganic−Organic Atmospheric Aerosol. Environmental Science & Technology 34(20):4313-4319.

Decesari S, Facchini MC, Fuzzi S, McFiggans GB, Coe H, Bower KN. 2005. The water-soluble organic component of size-segregated aerosol, cloud water and wet depositions from Jeju Island during ACE-Asia. Atmospheric Environment 39(2):211-222.

Flores JM, Bar-Or RZ, Bluvshtein N, Abo-Riziq A, Kostinski A, Borrmann S, Koren I, Koren I, Rudich Y. 2012. Absorbing aerosols at high relative humidity: linking hygroscopic growth to optical properties. Atmospheric Chemistry and Physics 12(12):5511-5521.

Gupta P, Christopher SA, Wang J, Gehrig R, Lee Y, Kumar N. 2006. Satellite remote sensing of particulate matter and air quality assessment over global cities. Atmospheric Environment 40(30):5880-5892.

Kanakidou M, Seinfeld JH, Pandis SN, Barnes I, Dentener FJ, Facchini MC, Van Dingenen R, Ervens B, Nenes A, Nielsen CJ et al. . 2005. Organic aerosol and global climate modelling: a review. Atmos. Chem. Phys. 5(4):1053-1123.

Langridge JM, Richardson MS, Lack DA, Brock CA, Murphy DM. 2013. Limitations of the Photoacoustic Technique for Aerosol Absorption Measurement at High Relative Humidity. Aerosol Science and Technology 47(11):1163-1173.

Lewis ER. 2008. An examination of Kohler theory resulting in an accurate expression for the equilibrium radius ratio of a hygroscopic aerosol particle valid up to and including relative humidity 100%. Journal of Geophysical Research-Atmospheres 113(D3).

Liu P, Zhang Y, Martin ST. 2013. Complex Refractive Indices of Thin Films of Secondary Organic Materials by Spectroscopic Ellipsometry from 220 to 1200 nm. Environmental Science & Technology 47(23):13594-13601.

Malm WC, Day DE, Kreidenweis SM, Collett JL, Carrico C, McMeeking G, Lee T. 2005. Hygroscopic properties of an organic-laden aerosol. Atmospheric Environment 39(27):4969-4982.

Moteki N, Kondo Y, Nakayama T, Kita K, Sahu LK, Ishigai T, Kinase T, Matsumi Y. 2010. Radiative transfer modeling of filter-based measurements of light absorption by particles: Importance of particle size dependent penetration depth. Journal of Aerosol Science 41(4):401-412.

Onasch TB, Siefert RL, Brooks SD, Prenni AJ, Murray B, Wilson MA, Tolbert MA. 1999. Infrared spectroscopic study of the deliquescence and efflorescence of ammonium sulfate aerosol as a function of temperature. Journal of Geophysical Research: Atmospheres 104(D17):21317-21326.

Onasch TB, Massoli P, Kebabian PL, Hills FB, Bacon FW, Freedman A. 2015. Single Scattering Albedo Monitor for Airborne Particulates. Aerosol Science and Technology 49(4):267-279.

Orozco D, Beyersdorf AJ, Ziemba LD, Berkoff T, Zhang Q, Delgado R, Hennigan CJ, Thornhill KL, Young DE, Parworth C et al. . 2016. Hygrosopicity measurements of aerosol particles in the San Joaquin Valley, CA, Baltimore, MD, and Golden, CO. Journal of Geophysical Research: Atmospheres 121(12):7344-7359.

Petters MD, Kreidenweis SM. 2007. A single parameter representation of hygroscopic growth and cloud condensation nucleus activity. Atmospheric Chemistry and Physics 7(8):1961-1971.

Presser C. 2012. Absorption coefficient measurements of particle-laden filters using laser heating: Validation with nigrosin. Journal of Quantitative Spectroscopy & Radiative Transfer 113(8):607-623.

Radney JG, Zangmeister CD. 2015. Measurement of Gas and Aerosol Phase Absorption Spectra across the Visible and Near-IR Using Supercontinuum Photoacoustic Spectroscopy. Analytical Chemistry 87(14):7356-7363.

Redemann J, Russell PB, Hamill P. 2001. Dependence of aerosol light absorption and single-scattering albedo on ambient relative humidity for sulfate aerosols with black carbon cores. Journal of Geophysical Research-Atmospheres 106(D21):27485-27495.

Robinson CB, Schill GP, Zarzana KJ, Tolbert MA. 2013. Impact of Organic Coating on Optical Growth of Ammonium Sulfate Particles. Environmental Science & Technology 47(23):13339-13346.

Royalty TM, Phillips BN, Dawson KW, Reed R, Meskhidze N, Petters MD. 2017. Aerosol Properties Observed in the Subtropical North Pacific Boundary Layer. Journal of Geophysical Research-Atmospheres 122(18):9990-10012.

Saleh R, Robinson ES, Tkacik DS, Ahern AT, Liu S, Aiken AC, Sullivan RC, Presto AA, Dubey MK, Yokelson RJ et al. . 2014. Brownness of organics in aerosols from biomass burning linked to their black carbon content. Nature Geoscience 7(9):647-650.

Sumlin BJ, Heinson WR, Chakrabarty RK. 2018. Retrieving the aerosol complex refractive index using PyMieScatt: A Mie computational package with visualization capabilities. Journal of Quantitative Spectroscopy and Radiative Transfer 205:127-134.

Tang IN, Munkelwitz HR. 1994. Aerosol Phase-Transformation and Growth in the Atmosphere. Journal of Applied Meteorology 33(7):791-796.

Toon OB, Pollack JB, Khare BN. 1976. Optical-Constants of Several Atmospheric Aerosol Species - Ammonium-Sulfate, Aluminum-Oxide, and Sodium-Chloride. Journal of Geophysical Research-Oceans and Atmospheres 81(33):5733-5748.

Weingartner E, Burtscher H, Baltensperger U. 1997. Hygroscopic properties of carbon and diesel soot particles. Atmospheric Environment 31(15):2311-2327.

Wu Y, Cheng T, Liu D, Allan JD, Zheng L, Chen H. 2018. Light Absorption Enhancement of Black Carbon Aerosol Constrained by Particle Morphology. Environmental Science & Technology 52(12):6912-6919.

Zhang QH, Zhang JP, Xue HW. 2010. The challenge of improving visibility in Beijing. Atmospheric Chemistry and Physics 10(16):7821-7827.

4 Toward Non-Invasive Measurement of Atmospheric Temperature Using Vibro-Rotational Raman Spectra of Diatomic Gases

We demonstrated precise determination of atmospheric temperature using vibro-rotational Raman (VRR) spectra of molecular nitrogen and oxygen in the range of 292-293K. We used a continuous wave fiber laser operating at 10 W near 532nm as an excitation source in conjunction with a multi-pass cell. First, we will show that the approximation that nitrogen and oxygen molecules behave like rigid rotors leads to erroneous derivations of temperature values from VRR spectra. Then, we will account for molecular non-rigidity and compare four different methods for the determination of air temperature. Each method requires no temperature calibration. The first method involves fitting the intensity of individual lines within the same branch to their respective transition energies. We also infer temperature by taking ratios of two isolated VRR lines; first from two lines of the same branch, and then from one line from the S-branch and one from the O-branch. Finally, we take ratios of groups of lines. Comparing these methods, we found that a precision up to 0.1K is possible. In the case of O_2, a comparison between the different methods show that the inferred temperature was self-consistent to within 1K. The temperature inferred from N_2 differed by as much as 3K, depending on which VRR branch was used. Here, we discuss the advantages and disadvantages of each method. Our methods can be extended to the development of instrumentation capable of non-invasive monitoring of gas temperature with broad potential applications (for example, in laboratory, ground-based, or airborne remote sensing).

4.1 Introduction

Small changes in temperature can have non-linear effects on several processes. One such case is the nucleation of non-sea-salt sulfate particles from sulfuric acid in the atmosphere, where a decrease in temperature of a couple of degrees Celsius can result in an order of magnitude increase in new particle formation (Easter and Peters 1994). As a result, fluctuations in temperature can result in enhanced nucleation rates of particles. For

example, Platis et. al. (Platis et al. 2016) observed a new particle formation event in an inversion layer with large fluctuations in temperature. However, measurements of the inversion layer are often limited by coarse time resolution, and the direct relationship between temperature fluctuations and new particle formation is unknown. Also, fluctuations in water vapor saturation ratio are dependent on temperature fluctuations (Kulmala et al. 1997). The conditions most favorable for new particle formation involving water are those where saturation ratio and temperature are anti-correlated (Nilsson and Kulmala 1998; Platis et al. 2016). Temperature fluctuations can also affect the supersaturation in clouds, which in turn determines the activation and eventual growth of cloud droplets. In fact, thermodynamic fluctuations due to turbulent mixing in clouds may broaden the size distribution of droplets, which has implications for precipitation and the cloud optical properties (Chandrakar et al. 2016; Chandrakar et al. 2018). To understand the effect that temperature fluctuations can have on the evolution of aerosol and cloud droplets, continuous monitoring of temperature would be ideal. This can be difficult above the ground level using direct means of temperature measurements, which are often performed by aircraft and radiosondes. Temperature fluctuations can be difficult for aircraft to measure, especially in clouds where condensation can limit the time response and accuracy of temperature measurements (Bange et al. 2013). While research aircraft are capable of high temporal and spatial resolution measurements in the horizontal direction (along the flight path), the range-resolved resolution of these measurements is poor (Muppa et al. 2016). Remote sensing techniques cannot only provide vertical profiles but can also monitor the evolution of those vertical profiles over time.

Raman and Rayleigh scattering techniques are used in a variety of applications where temperature must be determined remotely (Laurendeau 1988). Some of these techniques have been developed to measure the temperature during combustion processes, while others have been developed to measure atmospheric temperature. For example, Rayleigh scattering is often used to measure changes in molecular number density in flames, which are in turn related to temperature using the ideal gas law under the assumption that the

medium being measured has constant pressure and known molecular composition (Haumann and Leipertz 1984; Hoffman et al. 1996). Additionally, changes in laser intensity, and elastic scattering from large particles, must be accounted for when using Rayleigh techniques; in fact, cloud droplets and dust can degrade the precision of the technique (Laurendeau 1988). In an alternative approach, the intensity of pure rotational Raman (PRR) transitions can be used to determine the temperature of flames and the atmosphere without needing to make assumptions about the pressure or the composition of the gas (Michael C Drake and Rosenblatt 1978). PRR light detection and ranging (LiDAR) is the most widely accepted remote air temperature measurement technique used by the atmospheric LiDAR community (Cooney 1972; Behrendt and Reichardt 2000; Radlach et al. 2008). A significant advantage of Raman-based techniques is the ability to take a ratio of two portions of the scattered spectrum, eliminating the need to monitor the laser intensity. However, the proximity of the rotational Raman lines to elastic scattering signal presents a significant challenge especially in turbid environments, such as clouds. Modern narrow band-pass filters have allowed the technique to be employed with minimal systematic errors in aerosol layers and optically thin clouds (Wulfmeyer et al. 2015). Several methods have been developed to extract temperature information from the vibrational spectra of N_2 and O_2, which are spectrally separated from elastic scattering (Lapp et al. 1973). The spectral separation allows for the use of optical filters that attenuate elastically scattered light better to reduce the systematic errors imposed by large particle scattering. The Stokes vibrational line has also been used for satellite-based temperature determination in the stratosphere using a similar principle to the Rayleigh methods described above, but Rayleigh measurements are necessary to estimate density (Keckhut et al. 1990). Temperature can also be determined by taking a ratio of the Stokes and anti-Stokes pure vibrational scattering; however, this technique is not tenable at atmospherically relevant temperatures due to weak anti-Stokes signal (Laurendeau 1988). Several hybrid methods have also been developed to estimate atmospheric temperature. Su et al. compared the Stokes Q-Branch Raman transition to a PRR line with a high rotational quantum number to determine atmospheric temperature

up to a height of 22 km. The technique determined the temperature within a cloud to within 1.5 K of a radiosonde measurement (Su et al. 2020)

Temperature can be determined from the S- and O-branches of the vibro-rotational Raman (VRR) spectrum of O_2 and N_2 in a similar fashion to the PRR spectrum. For both cases, Maxwell-Boltzmann statistics dictate that molecules populating lower energy rotational states will begin to populate higher energy rotational states as temperature increases (Long 1977). The VRR spectrum is spectrally located further from the excitation wavelength than the PRR spectrum. This is especially advantageous in environments including particulate matter, such as aerosol or droplets, as the filters needed to isolate the VRR spectrum will be less prone to allowing the elastic scattering signal to leak to the photodetector. Along with being spectrally distant from the elastic scattering band, the vibro-rotational spectra of O_2 and N_2 are also spectrally separated from each other, unlike in PRR spectra. The PRR spectrum includes lines from every Raman active gaseous constituent in the atmosphere. In fact, for an excitation source at 532 nm the vibro-rotational Raman (VRR) spectra of O_2 and N_2 can be found well separated from each other between 575 and 585 nm and 600 and 615 nm, respectively (Behrendt et al. 2002). Because the Raman lines from one atmospheric constituent will not overlap with the Raman lines from another atmospheric constituent, direct calculations of temperature from the VRR spectra are more simple than from the PRR spectra. However, the VRR lines are about two orders of magnitude weaker than the PRR lines, representing a significant disadvantage. Therefore, we are not suggesting methods that employ VRR to derive temperature should replace the PRR method in every case; however, the VRR method can be significantly advantageous in situations where elastic scattering could drastically deteriorate the accuracy and sensitivity of the PRR method.

An important consideration for applications reliant on the intensity of VRR lines is the fact that the Raman cross-section is dependent on the rotational quantum number, J, due to vibrational-rotational coupling. The coupling is a direct consequence of diatomic molecules behaving such as non-rigid rotors. Ustav and Varghese determined the

temperature of gases in flames by simultaneously fitting the intensity profiles of the S-, O-, and Q- branches (Utsav and Varghese 2013), though they note that temperature determination is mostly influenced by the shape of the Q-Branch. A LiDAR system was also developed that determines temperature by taking a ratio of individual VRR N_2 lines, as well as fitting the intensity of individual N_2 lines (Liu and Yi 2014). While they showed that their system was within 2.2 K of a radiosonde up to 7 km, Liu and Yi treat the nitrogen molecule as a rigid rotor that we show lead to significant bias. This bias may have been offset by the low spectral resolution of their system, which could result in overlap errors from adjacent lines.

In this work, we demonstrate how temperature can be derived from the fully resolved O- and S- branches in the Raman fundamental band of N_2 and O_2. Our methods use the integrated intensity of individual lines within the VRR spectra to determine the temperature. The intensity of each line depends on the Raman cross-section of the molecule, the Maxwell-Boltzmann distribution, the VRR line strength, the nuclear spin statistics, and other factors as can be seen from Equation 4.1 below. Each of these components can be expressed mathematically from first principles, which allows for temperature to be inferred from VRR spectra without the need for ad hoc temperature calibration. We start our discussion by considering two theoretical approaches to the problem. First, molecules are treated as rigid rotors, an approach typically used in PRR applications. While non-rigidity can affect the intensities of PRR lines, it is usually believed to be small enough to be ignored. However, the vibrational-rotational coupling is stronger in the VRR spectra and must be accounted for (Buckingham and Szabo 1978; Asawaroengchai and Rosenblatt 1980). We show that this approach leads to significant biases in temperatures derived from the S- and the O-branch. Then, we examine the case of molecular non-rigidity where the Raman cross-section is dependent on the rotational quantum number. The correction is shown to improve the accuracy of temperatures determined from the VRR spectra, as well as the agreement between temperatures derived from the S-branch and those derived from the O-branch. From there, we set out to derive and implement four separate methods that infer temperature from the S- and O-

branches of N_2 and O_2. An inter-comparison between the different methods allows us to determine the relative accuracy and precision of each method.

4.2 Materials and methods

4.2.1 Experimental Setup and Procedures

All spectra used to ascertain atmospheric temperature were measured using the experimental setup in Figure 4.1 (Kiefer et al. 1972; Borysow and Fink 2005). We used a half waveplate (WP) to rotate the laser's polarization to be perpendicular to the detector. This ensured that only the depolarized component of the Raman scattered reached the

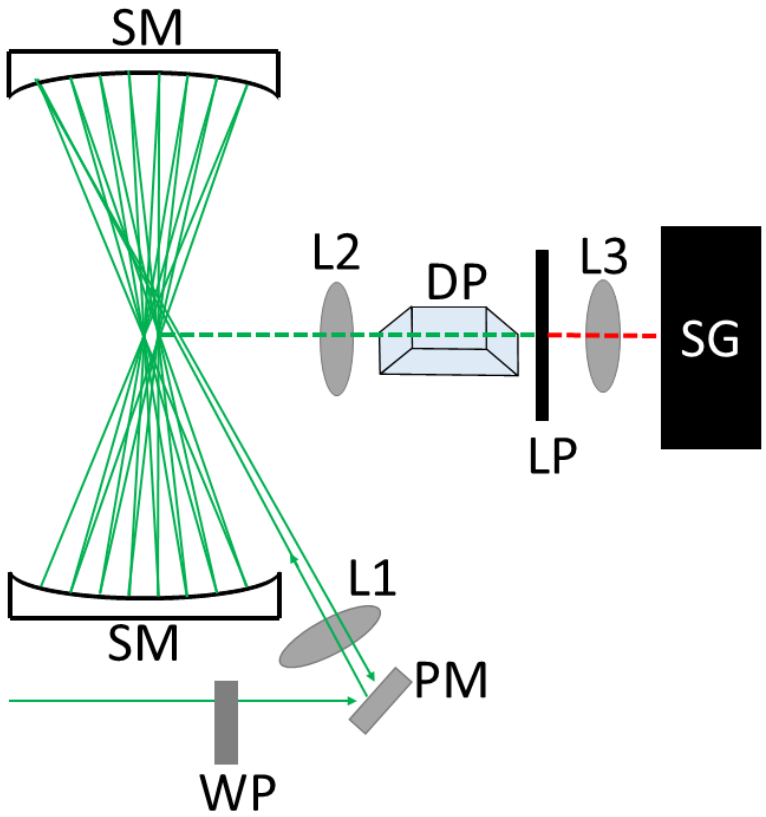

Figure 4.1: Experimental setup for measuring the spectrum of N_2 and O_2 consists of: WP: half waveplate PM: planar mirror, L1: focusing lens (f = 150 mm), SM: spherical concave mirrors (f = 50 mm), L2: plano-convex lens (75 mm), L3: plano-convex lens (250 mm), DP: dove prism, LP: long-pass filter, SG: spectrograph.

spectrograph (Long 1977; Borysow et al. 2019). This had the effect of reducing the intensity of the Q-branches of each gas species and all their isotopologues without affecting the intensity of the S- and O- Branches. This was optimized by rotating the WP to reduce the observed contribution of the Q-branch. A planar mirror (PM) redirected the laser beam through a focusing lens (L1), which focused the beam in the center of a multi-pass cavity. The multi-pass cell consisted of two 50.2 mm spherical concave mirrors (SM) with 100 mm radius of curvature. Both SM were separated by 200 mm, or four focal lengths. Using this setup, we could achieve 40 passes through the scattering region at the center of the cell. Collection lenses (L2, L3) imaged the scattering region on to the spectrograph's entrance slit, while a Dove prism (DP) rotated light from the scattering region to cover the entrance slit. A long-pass filter (LP), inserted in the collimated portion of the beam, blocked elastic scattering from entering the spectrograph while allowing Raman scattering to pass. LP had a cut-off wavelength of 535 nm, an optical density greater than 7 at 532 nm, and a transmission of about 98% for the VRR spectral region. A lot of effort was put into reducing the amount of light reflected off surfaces to ensure light leakage was minimal. The small amount of background light that still leaked through the system was removed by collecting background spectra and accounted for no more than 5% of the signal for high J peaks and was negligible for lower J peaks. The spectrograph (SG), a 0.5 m system with a 1200 groove/mm diffraction grating, was coupled to a CCD camera that was thermo-electrically cooled to -50^{o} C. This resulted in a spectral resolution of 0.1 nm (or 3 cm^{-1}). Examples of the VRR spectra of atmospheric molecular nitrogen and oxygen at ambient temperature are shown in Figure 4.1. We estimate that light transmission from the imaging plane to the CCD camera is on the order of 0.1%. To gather enough photons for each experiment, spectra were measured with 15 exposures of 60 s each. Using multiple exposures allowed for high photon counts without exceeding the pixel depth of the CCD sensor. Across all experiments, the room air temperature varied from 292.2 K to 293.3 K, as measured by a thermocouple situated about a meter away from the measurement area. This small temperature change was achieved by adjusting the room temperature using a small air conditioning unit.

Data analysis was performed using custom Python scripts. First, baseline subtraction was performed in post-process using linear regression, and we then corrected for the ν^3 line intensity dependence of the VRR spectra (see Equation 4.1 below). Optical corrections were subsequently applied to account for the wavelength dependent properties of the spectrograph's optical components as provided by the manufacturer. This included the quantum efficiency of the CCD sensor, the reflectivity of three mirrors, and the efficiency of the diffraction grating. Cosmic rays removal was performed by comparing each exposure to the average of all exposures, and any pixel with signal outside of a three sigma limit within each exposure was replaced with the median value over all exposures. Integration of each peak was performed using the trapezoid method, with the center point of each integration range being determined by reconstructing the spectrum using cubic interpolation. While the lines within a single branch were integrated using the same integration width, the integration width varied between different branches of the VRR spectra. These integration ranges were determined by minimizing uncertainties related to line overlap. Broadening effects due to changes in temperature should not change these integration ranges. The perceived broadening of the Raman lines is entirely due to instrumental resolution and broadening changes as a function of $\sqrt{T}$. Broadening will remain significantly less than our instrumental resolution for any atmospherically relevant temperature.

4.2.2 High-Resolution Raman Spectra of Molecular Oxygen and Nitrogen

From Figure 4.2, we can see that care must be taken when selecting lines to determine temperature. VRR lines in the immediate vicinity of the Q-Branch need to be avoided due to the overlap biases. The lines to be avoided include $J = 0,1$ and $J = 2,3$ of the S-branch and O-branch of N_2, respectively. The same can be said for $J = 1$ and $J = 3$ in O_2 S-branch and O-branch, respectively. We also avoid using lines that overlap with the pure vibrational Raman lines of isotopologues $^{14}N^{15}N$ and $^{16}O^{18}O$. The isotopologues vibrational lines overlap with $J = 5,6$ and $J = 7,9$ in the O-branch of N_2 and O_2, respectively. Near room temperature, the maximum Raman intensity is measured at $J = 6$

and $J = 9$ for N_2 and O_2, respectively, after which the intensity decreases quickly. Furthermore, N_2 lines with even J are more favorable due to their higher intensity with respect to odd numbered lines due to nuclear spin degeneracy. Therefore, for N_2, we will focus on even lines within the ranges of 2132-2306 cm^{-1} (O-branch, $4 \leq J \leq 24$) and 2355-2523 cm^{-1} (S-branch, $2 \leq J \leq 24$). The analysis for O_2 will focus on the lines within the ranges of 1413-1533 cm^{-1} (O-branch, $5 \leq J \leq 23$) and 1575-1689 cm^{-1} (S-branch, $3 \leq J \leq 23$).

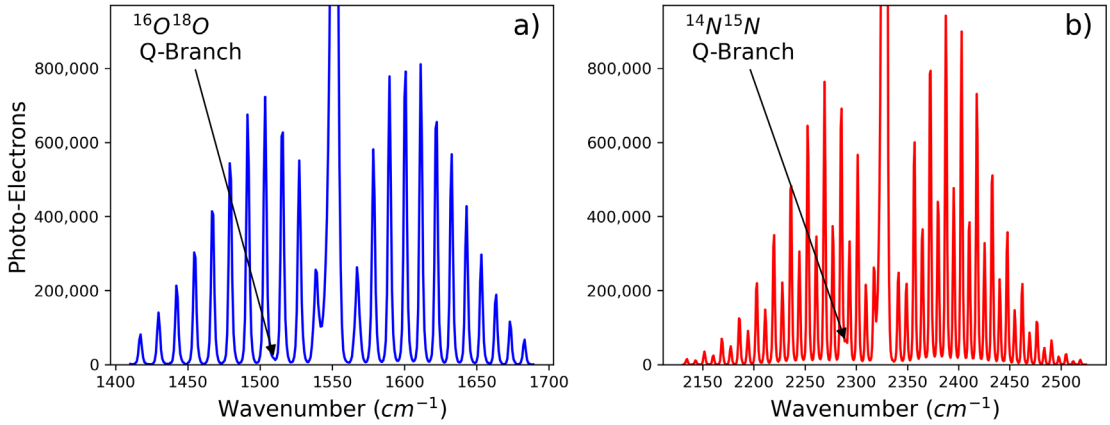

Figure 4.2: Spectra taken in the vicinity of the fundamental band of molecular (a) nitrogen and (b) oxygen with 60s integration time.

4.2.3 Accuracy and precision of temperature estimates

Atmospheric temperature was determined from 24 separate spectra, 11 from O_2 and 13 from N_2. For each experiment, the thermocouple was used to determine the temperature of the room. However, as mentioned earlier, the thermocouple was positioned about a meter from the scattering volume. This was because we wanted to avoid light scattered off the thermocouple from entering the spectrograph. To ensure room temperature was measured, we ensured the thermocouple was not in contact with the optical bench. Even if the thermocouple were closer to the scattering plane, it would have been difficult to determine, with high accuracy, the temperature in the scattering region. In fact, 400 W of continuous-wave laser power was focused onto the scattering region of the multi-pass

cell. Therefore, the thermocouple readings are not ideal for determining the accuracy of the temperature values determined from the VRR spectra. We still use the thermocouple for comparison throughout the paper; however, inter-comparisons of Raman derived temperatures are our primary tool in determining the precision and self-consistency of our approaches. By comparing rigid rotor and non-rigid rotor derived temperatures to the thermocouple, we show how agreement between the Raman and thermocouple temperatures can be improved using non-rigidity corrections. However, by comparing temperature derived from the S-branch to temperature derived from the O-branches, we show that non-rigid rotor corrections are also necessary for Raman-based inferred temperatures to be self-consistent or agree with each other.

Of the four methods, we first use the fitting of integrated intensities of the individual VRR lines within the O- and S-branch from each spectra to determine temperature. The temperatures derived from fitting line intensities within the S- and O- branch are compared to each other to determine self-consistency and precision of the fitting method. To test self-consistency, we take the mean of the temperature difference for two different methods over all spectra analyzed. Precision is determined by taking the standard deviation of the temperature difference for two different methods over all spectra analyzed. Throughout Section 4.3, each method derived to infer temperature from VRR spectra is compared to the temperature determined by the fitting method. We choose to use the fitting method as the reference because it incorporates all viable lines within a branch and has been previously used to determine temperature in both PRR and VRR temperature applications (M. C. Drake and Rosenblatt 1976; Michael C Drake and Rosenblatt 1978; Liu and Yi 2014). These comparisons are branch specific, meaning that a measurement method that uses VRR transitions from the S-branch of nitrogen is compared to the temperature and uncertainty determined from the fitting of the S-branch of nitrogen, et cetera. In Section 4.4, we explore the self-consistency and precision of all methods performed and look at how each method correlates as the temperature in the room changes.

4.3 Results

4.3.1 Temperature dependence of a rigid diatomic molecule

The Raman signal from a single vibro-rotational transition $v = 1 \leftarrow v = 0,\ J + 2 \leftarrow J$, measured in units of number of photons, taken at temperature T, is equal to (Long 1977):

$$I(v,J,T) = A \times \sigma \times \nu^3(v,J) S(J) \frac{N}{Q_r} g_J e^{-\frac{E_J}{k_B T}} \qquad \text{Equation 4.1}$$

where A includes all fundamental constants and factors accounting for the scattering geometry common to all vibro-rotational Raman lines, σ is the cross section common to all rotational transitions within the rigid rotor approximation, N is the total number of molecules, g_J is the nuclear spin factor associated with a rotational quantum number J, E_J is the energy of the rotational state J, and $\nu(v,J)$ is the frequency of the Raman line corresponding to the vibrational quantum numbers v and the rotational quantum number J. $S(J)$ is the rotational and vibro-rotational line strength which differs for the S-branch and the O-branch:

$$\text{S-Branch: } S(J) = \frac{(J+1)(J+2)}{(2J+3)}$$
$$\text{O-Branch: } S(J) = \frac{J(J-1)}{(2J-1)} \qquad \text{Equation 4.2}$$

Finally, the partition function, Q_r, represents the sum over all rotational states:

$$Q_r = \sum_J g_J (2J+1) e^{-\frac{E_J}{k_B T}} \qquad \text{Equation 4.3}$$

In the case of O_2, the nuclear statistical factor, g_J, is equal to 0 for even J and equal to 1 for odd J, while for N_2, g_J is equal to 6 for even J and 3 for odd J. The alternating intensity of N_2 and the absence of even rotational states of O_2 seen in Figure 4.1 is a direct result of g_J. $I(v,J,T)$ is measured in units of number of photoelectrons and carries a counting error of $\sqrt{I(v,J,T)}$. The $I(v,J,T)$ term corrected for the wavelength dependent optical efficiency of the spectrograph and the ν^3 dependence in Equation 4.1 is denoted with a prime $I'(v,J,T) = I(v,J,T)/\nu^3(v,J)$.

4.3.2 Least-squares regression of VRR line intensity

We follow the method of temperature estimation from fundamental Raman bands of N_2 and O_2 first derived by James and Klemperer (James and Klemperer 1959) and later used by Asawaroengchai and Rosenblatt (Asawaroengchai and Rosenblatt 1980). The rigid-rotor form of the equation can be derived from Equation 4.1:

$$k_B ln\left(\frac{I'(J)}{S(J) \times g_J}\right) = k_B ln\left(\frac{Q_r}{A\sigma N}\right) - \frac{1}{T_{Fit}} \times E_J \qquad \text{Equation 4.4}$$

The left-hand side of Equation 4.4 is the dependent variable, while the energy, E_J, is the independent variable. The logarithm on the right side of the equation includes only constants, and therefore forms the intercept. Temperature can be extracted from Equation 4.4 using linear least-squares regression. We show an example of these fits in Figure 4.3, where we infer temperature by fitting integrated VRR transitions of N_2. For these fits, we did not include lines directly adjacent to the pure vibrational line and those overlapping with the primary isotopologue's vibrational line. For N_2, only the lines with even

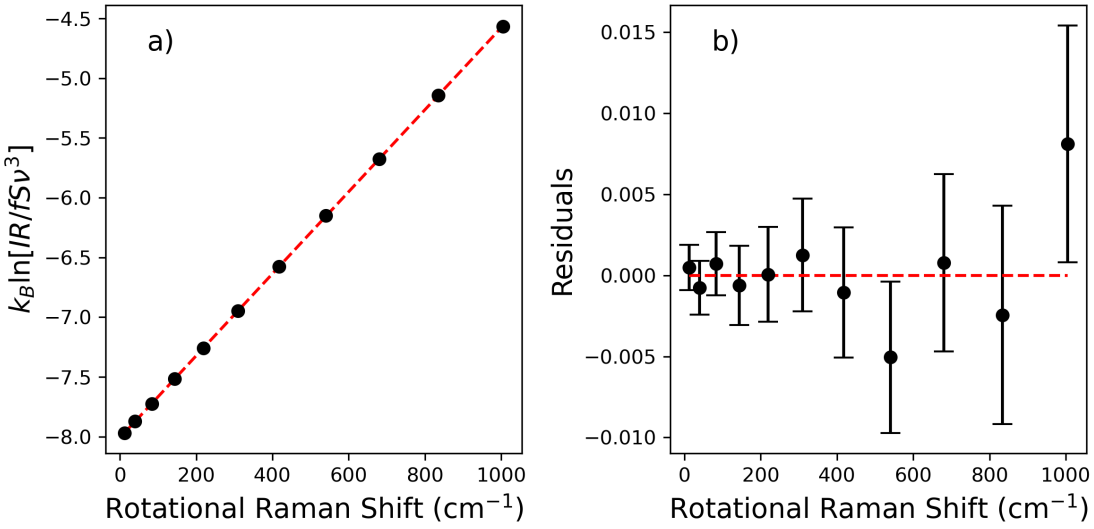

Figure 4.3: Temperature can be determined by fitting the intensity of individual lines. **(a)** The temperature is inferred from the S-Branch of N_2 from the inverse of the slope. The error bars are much smaller than the data markers. **(b)** The residual plot shows that the uncertainty is comparable to the residuals.

rotational quantum numbers were used in the fits to reduce the effects of bias from overlapping lines.

Least-squares regression was performed on integrated line intensities from each of the O_2 and N_2 VRR spectra. Each fit was optimized by minimizing the χ^2 statistic. For each of the experiments, $R^2 > 0.99$ and $\chi^2 < 1.5$, suggesting good agreement between model and data. In Table 4.1, we show the statistics of comparing the results from each branch to the thermocouple (TC), as well as temperatures derived from each branch to each other. On average, the temperature determined using the S-branch and O-branch of both gases differ significantly. These differences vary only a small amount, as shown by the standard deviation of the differences between S- and O- branch temperatures in Table 4.1. Additionally, none of the fitting-derived temperatures agree with the room temperature measured by the thermocouple. The low temperature values inferred from the S-branch of both gases suggest that the intensity of lines decay faster with respect to J than predicted by the rigid-rotor approximation in the S-Branch. Meanwhile, the high temperature values inferred from the O-branch of both gases suggests the intensity of lines are decaying slower with respect to J than predicted by the rigid-rotor approximation in the O-Branch.

Table 4.1: Comparisons of temperatures derived from fitting VRR line intensities and measured using thermocouple (TC) when molecules are assumed to be rigid-rotors. The columns from left to right are the mean difference of the S-branch and thermocouple temperatures, the O-branch and thermocouple temperatures, the mean difference of the S- and O-branch temperatures, and the standard deviation of the difference of S- and O-branch temperatures.

Gas	$\overline{\mathbf{T_S - T_C}}$	$\overline{\mathbf{T_O - T_C}}$	$\overline{\mathbf{T_S - T_O}}$	$\overline{\boldsymbol{\sigma}_{\mathbf{T_S - T_O}}}$
N_2	-9.1 K	8.8 K	-17.9 K	0.3 K
O_2	-11.9 K	12.9 K	-24.2 K	0.2 K

4.3.3 Temperature dependence of the non-rigid diatomic molecule

Table 4.2: Molecular constants used in non-rigidity corrections for O_2 and N_2. These are the rotational constant (B_e), zero-point vibrational energy (ω_e), the polarizability anisotropy ratio (b_0), and the uncertainty in the anisotropy ratio (Δb_0).

	N_2	**O_2**	**Units**	**Ref.**
B_e	1.99824	1.4376766	cm^{-1}	(Herzberg and Huber 1979)
ω_e	2358.57	1580.19	cm^{-1}	(Herzberg and Huber 1979)
b_0	0.48	0.49	n/a	(Borysow et al. 2019)
δb_0	0.01	0.01	n/a	(Borysow et al. 2019)

The results in the previous section suggest that the Raman cross-section is dependent on the rotational quantum number. In this sub-section, we will demonstrate how treating O_2 and N_2 molecules as non-rigid rotors can improve the agreement between the two branches of the VRR spectra for both gases. The rigid-rotor approximation assumes that there is no vibrational-rotational coupling during a vibro-rotational transition. It has been shown, however, that this is not the case for the vibro-rotational spectrum of N_2 and O_2 (James and Klemperer 1959; Asawaroengchai and Rosenblatt 1980; Hamaguchi et al. 1981; Borysow et al. 2019). These works showed that the ratios of S- and O-branch line intensities with the same initial rotational state diverged from the rigid rotor approximation. This divergence is dependent on the quantity b_0, defined as (Asawaroengchai and Rosenblatt 1980):

$$b_0 = {\beta_e}/{r_e\beta_e'} \qquad \text{Equation 4.5}$$

where β_e and β_e' are the polarizability anisotropy and its first derivative at the equilibrium inter-nuclear distance r_e. Recently, we reported new, more accurate measurements of b_0 obtained from Raman spectra of fundamental bands of molecular O_2 and N_2 (Borysow et al. 2019). We report these values in Table 4.2. The dependence of line intensities on vibro-rotational interactions can be effectively accounted for using the first-order approximation of the Herman-Wallis factor, f_{01} (Herman and Wallis 1955) (Asawaroengchai and Rosenblatt 1980):

$$f_{01}(J) = 1 - 4b_0\epsilon m \qquad \text{Equation 4.6}$$

where $m = 2J + 3$ for the S-branch and $m = -2J + 1$ for the O-branch. The quantity ϵ is twice the ratio of the rotational constant of the molecule (B_e) and its zero-point vibrational energy (ω_e) (Hamaguchi et al. 1981). The values for B_e and ω_e can be found in Table 4.2. The subscript $_{01}$ designates the fundamental band.

4.3.4 Applying non-rigidity to least-squares regression

The Herman-Wallis correction factor acts as a J-dependent modification of the intensity of a vibro-rotational transition. We can modify Equation 4.4 to reflect this:

$$k_B ln\left(\frac{I'(J)}{S(J) \times g_J \times f_{01}(J)}\right) = C_o - \frac{1}{T} \times E_J \qquad \text{Equation 4.7}$$

where we designated the intercept from Equation 4.4 as C_o, and the non-rigidity correction has been incorporated into the left-hand side of the equation with the other J-dependent parameters. As can be seen from Table 4.3, the inclusion of the non-rigid rotor correction greatly improved the agreement between the temperatures inferred from the S- and O-branches of both gases. The quality of the fits are still high, with each fit having an $R^2 > 0.99$ and a $\chi^2 < 0.75$. However, the mean difference in temperatures from the N_2 branches is 3.0 K, with temperature inferred from the O-branch being the highest. While it is still unclear what the source of this discrepancy might be, it may be related to the difficulty in resolving the N_2 VRR spectra (which we discuss with more detail in Section 4.4.1). However, the precision of the measurement can be within 0.3 K. The O_2 measurements are in much better agreement; however, the uncertainty of the O-branch measurement is much larger than its S-branch counterpart. This could be the result of the O-branch having less viable VRR lines than the S-branch, resulting in fewer degrees of freedom while fitting. Considering the agreement between the two branches is 0.3 K, we can say that the fits of O_2's VRR line intensities are consistent to within 0.3 K and a precision of 0.3 K. The agreement of the temperatures inferred from VRR spectra and

those measured using the thermocouple also significantly improved as a result of incorporating the non-rigidity correction.

Table 4.3: Statistical comparisons of temperatures and uncertainties determined from fitting VRR line intensities. The columns, from left to right, are the gas, the mean difference of the S- and O-branch temperatures ($\overline{T_s - T_o}$), the standard deviation of the difference between the S- and O-branch ($\sigma_{T_s - T_o}$), the mean uncertainty of the S-branch temperature ($\overline{\Delta T_s}$), and the mean uncertainty of the O-branch temperature ($\overline{\Delta T_o}$).

Gas	$\overline{\mathbf{T_S - T_O}}$	$\boldsymbol{\sigma_{T_S - T_O}}$	$\overline{\boldsymbol{\Delta T_s}}$	$\overline{\boldsymbol{\Delta T_O}}$
N_2	-3.0 K	0.3 K	0.3 K	0.4 K
O_2	-0.3 K	0.3 K	0.5 K	1.4 K

4.3.5 Deriving temperature from two isolated lines of the same branch

By taking a ratio of the integrated intensities of two distinct VRR transitions, the temperature term in Equation 4.1 can be isolated. For optically corrected intensities of VRR lines with rotational quantum numbers J_1 and J_2, the ratio, R'_{J_1,J_2} is:

$$R'_{J1,J2} = \frac{I'(v,J_1,T)}{I'(v,J_2,T)} = \frac{f_{01}(J_1)}{f_{01}(J_2)} \times q(J_1,J_2) e^{-\frac{E_{J_1}}{k_B T}} e^{\frac{E_{J_2}}{k_B T}} \qquad \text{Equation 4.8}$$

where $q(J_1,J_2)$ is a ratio of the vibro-rotational line strengths:

$$\text{S-Branch: } q(J_1,J_2) = \frac{(J_1+1)(J_1+2)(2J_2+3)}{(J_2+1)(J_2+2)(2J_1+3)},$$
$$\text{O-Branch: } q(J_1,J_2) = \frac{J_1(J_1-1)(2J_2-1)}{J_2(J_2-1)(2J_1-1)} \qquad \text{Equation 4.9}$$

rearranging Equation 4.8 yields:

$$T(R'') = \frac{E_{J_2} - E_{J_1}}{k_B * ln\left[\frac{R''_{J_1,J_2}}{q(J_1,J_2)}\right]} \qquad \text{Equation 4.10}$$

The ratio R''_{J_1,J_2} includes the previously discussed corrections in addition to the non-rigidity corrections:

$$R''_{J_1,J_2} = R'_{J_1,J_2} \times \frac{f_{01}(J_2)}{f_{01}(J_1)} \qquad \text{Equation 4.11}$$

This formulation can be applied to any two-line combination in the VRR spectrum.

4.3.6 Propagation of uncertainty in temperature

We identified several sources of uncertainty that are accounted for in our analysis. Numerical integration is employed to quantify the intensity of each line. Due to the limited resolution of the spectrograph, the VRR lines overlap on the edges. This means that each integral is biased by signal from the Raman lines adjacent to it. We refer to this uncertainty as adjacent line bias. We estimated these uncertainties by fitting each spectrum with a series of Gaussian functions, one for each VRR line. Adjacent line bias was estimated by integrating the contribution from all adjacent Gaussian functions within the range of integration for a particular line. Another source of uncertainty is the numerical integration, performed using the trapezoidal rule. Integration ranges were chosen for each branch and gas, such that the sum of these three uncertainties were minimized. For N_2, the integration ranges were chosen to be 8.6cm^{-1} and 7.6cm^{-1} wide for the O- and S-branch lines, respectively. The integration ranges for O_2 were chosen to be 12.2cm^{-1} and 10.4cm^{-1} for the O- and S-branch lines, respectively. We also include the random uncertainty associated with the photon counting statistics (square root of the number of photons):

$$\Delta I'(J) = \sqrt{I'(J) + \Delta^2_{Integration} + \Delta_{Adj.Bias}{}^2} \qquad \text{Equation 4.12}$$

The only variables carrying an appreciable amount of uncertainty in Equation 4.10 are the experimental ratio of Raman line intensities, R'_{J_1,J_2}, and the non-rigidity correction, $f_{01}(J)$. The energies of corresponding transitions have been measured before and are known with accuracy better than 6 digits (Bendtsen 1974; Fletcher and Rayside 1974). We can therefore propagate the uncertainties using the following relation:

$$\Delta T = \frac{dT(R'')}{dR''}\Delta R'' \qquad \text{Equation 4.13}$$

Computing the derivative in Equation 4.13, we have:

$$\Delta T = \frac{\left|E_{J_2} - E_{J_1}\right|}{k_B * \ln\left[\frac{R''_{J_1,J_2}}{q(J_1,J_2)}\right]^2} \times \frac{\Delta R''}{R''} \qquad \text{Equation 4.14}$$

The uncertainty is directly proportional to the relative uncertainty of the corrected line ratios. The relative uncertainty of the corrected line ratios, R''_{J_1,J_2}, simplifies to the summation in quadrature of the relative uncertainty of the line intensities, as well as the relative uncertainty in non-rigidity corrections. Selecting lines with high intensity is favorable, as these lines will tend to have the lowest uncertainty relative to the intensity. However, intensity is not the only consideration when selecting lines. Using Equation 4.10, the uncertainty can be simplified to:

$$\frac{\Delta T}{T} = \frac{k_B T}{\left|E_{J_2} - E_{J_1}\right|} \times \frac{\Delta R''}{R''} \qquad \text{Equation 4.15}$$

where the uncertainty in R'' is determined from the uncertainty of the two lines using Equation 4.12. We can now see that the uncertainty is dependent on temperature and the difference in transition energy of each state. The uncertainty of temperature increases quadratically with temperature, leading to reduced accuracy as temperature increases. This can be counteracted by selecting lines that are far apart, effectively increasing the difference in energy between the two states. When temperature increases, lines with low rotational quantum number decrease in intensity, while lines with high rotational quantum number increase in intensity. When two lines are spectrally close, meaning the difference in their transition energies is low, the relative change in intensity of one line in comparison to the other is small. The resulting ratio of intensities is less sensitive to changes in temperature for two lines with small differences in transitional energy than two lines with large differences.

4.3.7 Two-Line Ratio Method

The temperature was inferred from every possible line combination within the chosen spectral window. The three possible combinations include using two lines from the S-Branch, using two lines from the O-Branch, or using one line from each branch. In Figure 4.4 and Figure 4.5, we compare the temperature values calculated using Equation 4.10 for every line combination to the values inferred from the least-squares fit for each experiment. Figure 4.4 focuses on temperatures derived from two-line, different branch ratios (TLDR), while Figure 4.5 focuses on temperature derived from two-line, same branch ratios (TLSR). In each figure, we plot the mean difference between every temperature value calculated from the two line ratio and those temperature values inferred by fitting VRR line intensities.

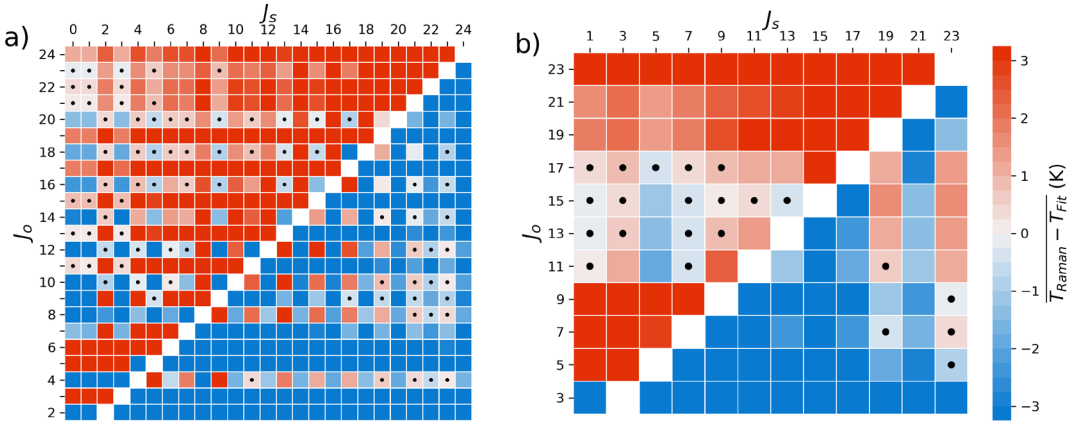

Figure 4.4: Mean temperature difference between the temperature derived from the two-line, different branch, method and the average of the least-squares method results for: **(a)** Nitrogen and **(b)** Oxygen. Black dots represent line combinations where the mean temperature difference and standard deviation of the temperature difference were both less than 1 K.

Several lines in Figure 4.4 and Figure 4.5 are consistent and have a precision with respect to the fitting method of less than 1K. We define the consistency with respect to the fitting method as the mean of the temperature differences for each line combination over all experiments, whereas the precision with respect to the fitting method is defined as the standard deviation of the temperature differences over all experiments. Table 4.4 compares the total number of lines that meet this 1 K requirement to the total number of lines for each gas and branch.

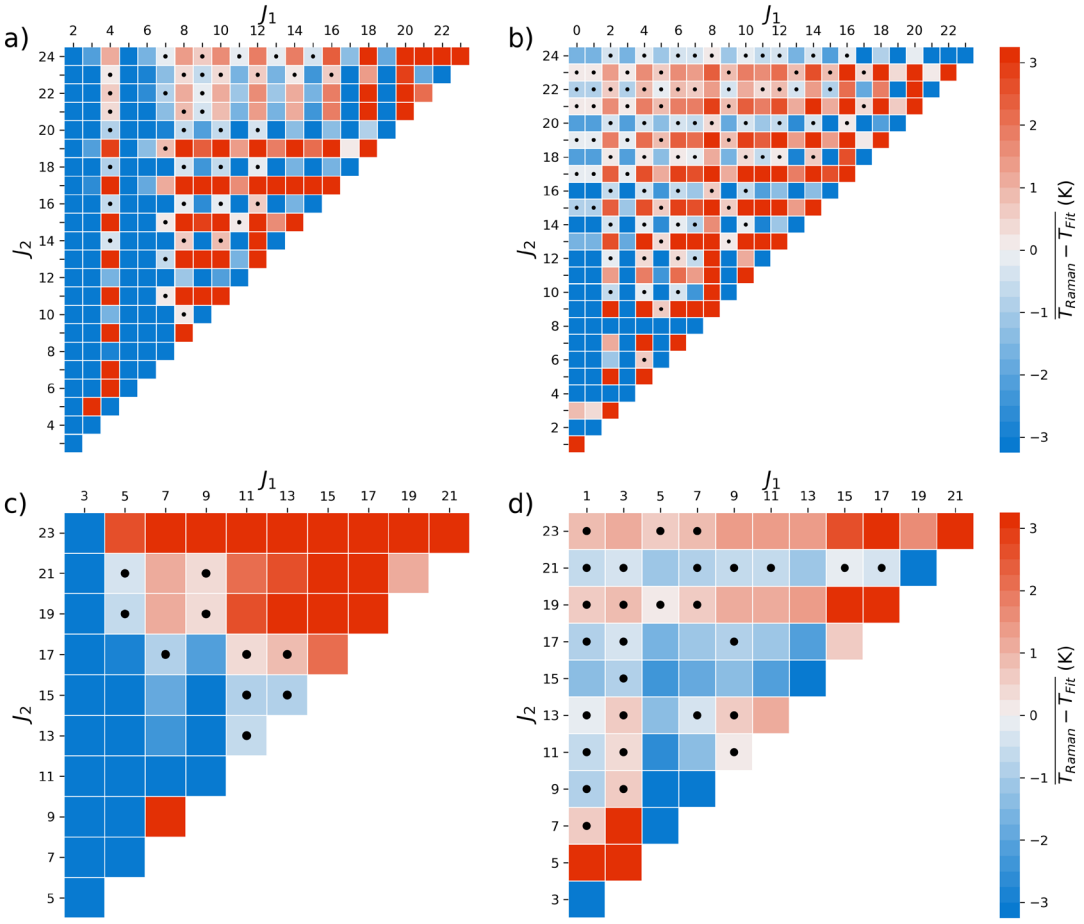

Figure 4.5: Mean temperature difference between the temperature derived from the two line, same branch, method and the least-squares method for the: (a) Nitrogen O-branch, (b) Nitrogen S-branch, (c) Oxygen O-branch, (d) Oxygen S-branch. Black dots represent line combinations where the mean difference and standard deviation of the difference are both less than 1 K, same as Figure 4.4.

Table 4.4: Summary of the two-line ratio method applied to two S-Branch lines (S), two O-Branch lines (O), and one line from each branch (TLDR). Here we show the total number of line combinations (N_{total}), the number of line combinations that meet the <1 K criteria ($N_{<1K}$), and the percentage of lines that meet these criteria. This table summarizes Figure 4.4 and Figure 4.5 above.

	N_2 (O)	**N_2 (S)**	**N_2 (TLDR)**	**O_2 (O)**	**O_2 (S)**	**O_2 (TLDR)**
N_{total}	253	300	552	55	66	121
$N_{<1K}$	39	87	80	10	28	22
$\frac{N_{<1K}}{N_{total}} \times 100\%$	15.4%	29%	14.5%	18.2%	42.4%	18.2%

Overall, the S-branches for both gases have a greater number of line combinations that meet the 1 K criteria than their O-branches or TLDR counterparts. The nitrogen S-branch includes the highest number of line combinations that meet the 1 K criteria, while the oxygen S-branch includes the highest percentage of lines meeting the 1 K criteria. The O-branch for each gas has a lower percentage of lines meeting our criteria because of greater overlap with the pure vibrational line, as well as the overlap with the Q-Branch corresponding to the second most abundant isotopologue. The TLDR method is comparable to the TLSR methods applied to the O-Branch in terms of the percentage of lines meeting our 1 K criteria for both gases.

In Table 4.5, we show the lines with the lowest absolute mean difference compared to temperature values determined by fitting VRR line intensities. Each of these line combinations is within 0.3 K of the fit inferred temperatures. The precision of each line with respect to the fit inferred temperature values is less than 0.7 K in each case. The line combinations with the best precision with respect to the fit derived temperature values are listed in Table 4.6 for each branch. The standard deviation is 0.3 K or less for each of the branches, and the mean differences for each of the lines are 1.0 K or less for everything but the N_2 TLDR result. It is also worth pointing out that the lines with the greatest precision are separated by at least 10 rotational quantum numbers.

Table 4.5: Line combinations with the lowest mean difference between the two-line ratios and the temperature values inferred from fitting. The columns are the gas and branch (in parentheses) temperature were inferred from. Two-line, different branch, columns are designated by TLDR. The rows, in order, are the line combination ($[J_1, J_2]$), the mean temperature difference ($\overline{T_{J_1,J_2} - T_{fit}}$), the standard deviation of the temperature difference $\sigma\left(\overline{T_{J_1,J_2} - T_{fit}}\right)$ and the mean uncertainty of the two-line same branch method ($\overline{\Delta T_{J_1,J_2}}$). For the TLDR columns the S-branch line is designated by J_1 and the O-branch line is designated by J_2.

	N_2 (O)	**N_2 (S)**	**N_2 (TLDR)**	**O_2 (O)**	**O_2 (S)**	**O_2 (TLDR)**
$[J_1, J_2]$	[12,18]	[12,18]	[6,12]	[5,21]	[15,21]	[9,15]
$\overline{T_{J_1,J_2} - T_{fit}}$	-0.2 K	0.2 K	-0.1 K	-0.3 K	-0.1 K	0.0 K
$\sigma\left(\overline{T_{J_1,J_2} - T_{fit}}\right)$	0.6 K	0.4 K	0.7 K	0.2 K	0.5 K	0.3 K
$\overline{\Delta T}$	0.5 K	0.7 K	0.9 K	0.3 K	1.0 K	0.8 K

Table 4.6: Line combinations with the lowest standard deviation for the difference between the two-line ratio temperature values and the ``fit inferred'' temperature values for each gas and branch. The rows and column labels follow the same convention as Table 4.5.

	N_2 (O)	**N_2 (S)**	**N_2 (TLDR)**	**O_2 (O)**	**O_2 (S)**	**O_2 (TLDR)**
$[J_1, J_2]$	[4,14]	[4,14]	[20,4]	[5,19]	[3,19]	[7,17]
$\overline{T_{J_1,J_2} - T_{fit}}$	-0.3 K	-0.1 K	-1.8 K	-0.7 K	1.0 K	0.0 K
$\sigma\left(\overline{T_{J_1,J_2} - T_{fit}}\right)$	0.3 K	0.1 K	0.2 K	0.2 K	0.1 K	0.1 K
$\overline{\Delta T}$	0.4 K	0.7 K	0.6 K	0.3 K	0.4 K	0.5 K

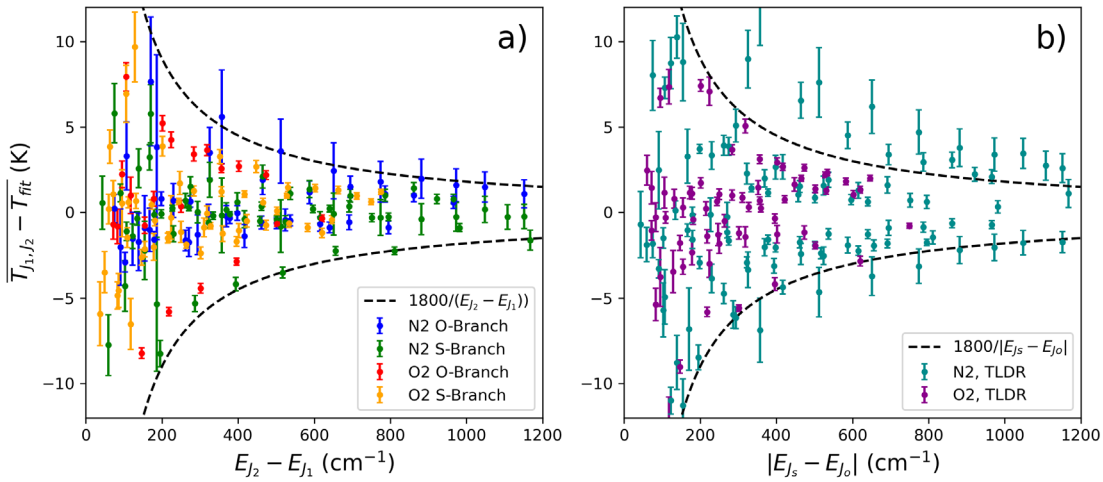

Figure 4.6: The mean difference between temperature values determined using the **(a)** two-line, same branch, and **(b)** two-line, different branch, methods and temperatures inferred from fitting for all spectra analyzed. Error bars represent the standard deviation of the temperature difference across all spectra. The dashed lines are used as a guide to illustrate the inverse relationship between the variability in temperature difference and energy difference. It should be noted that using Equation 4.15 this line is equivalent to a relative uncertainty in the line ratio of 0.003

As previously discussed, uncertainty is inversely proportional to the difference in rotational transition energies, or the wavenumber separation of the two VRR lines used. This is illustrated in Figure 4.6, where a clear decrease in mean temperature difference and variability is observed as the separation between the two lines increases. This shows that a line combination is more likely to have high consistency with respect to the fitting method as the two lines become more separated but does not preclude a line combination with lower separation. As can be seen, there are several line combinations in the range $E_n < 400$ cm^{-1} that are consistent with the fit to within 1K with respect to the fitting method. Figure 4.7 shows a more detailed summary of the uncertainty calculations. Line combinations with the greatest separation appear in the upper left-hand corner of each plot. While there are some exceptions, such as line combinations involving lines that overlap with the pure vibrational lines, the estimated uncertainty is lower for line combinations closer to the upper left-hand corner of each plot. For N_2, many of the line

combinations involving odd rotational quantum numbers have higher uncertainty. This is likely due to these line combinations having higher relative uncertainty from lower photon statistics and greater sensitivity to overlap from neighboring lines.

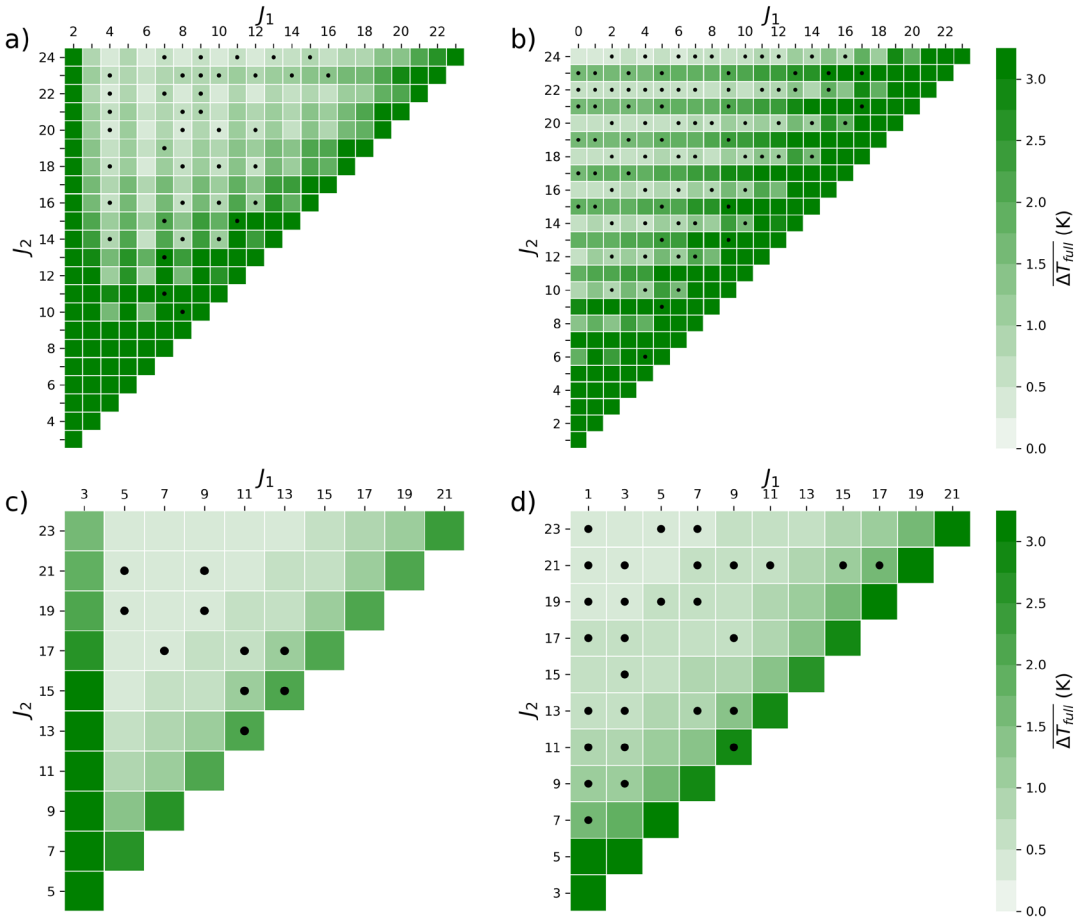

Figure 4.7: Average of uncertainty estimated using Equation 4.15 for: **(a)** Nitrogen O-branch, **(b)** Nitrogen S-branch, **(c)** Oxygen O-branch, **(d)** Oxygen S-branch. A black dot in a box represents line combinations where the mean difference and standard deviation of the difference are both less than 1K, same as Figure 4.4.

4.3.8 Multi-Line Ratio Method

So far, we either relied on taking the ratio of two isolated lines or fitting the intensity of a collection of isolated lines. However, this can be impractical, as isolating single lines requires a polychromator and a photo-detector array with high enough resolution to fully resolve each line. In applications that infer temperature from PRR spectra, it is more

typical to use photomultipliers to measure the light transmitted through narrow-band interference filters. These filters isolate two sections of the PRR spectra, each section including multiple lines. In addition to its simplicity, a major advantage of this type of setup is that each photodetector is measuring a higher signal, resulting in greater precision in comparison to the methods employing ratios of two isolated PRR lines. Finally, the typical transmission of filters is significantly higher than that of a polychromator system. Inspired by this approach and building from the theoretical work above, we derived a means of inferring temperature by taking a ratio of two regions within the VRR spectra.

We follow a similar approach to how we derived temperature from two isolated lines in the same branch. The energy of a line with rotational quantum number $J + i$, where i is an integer, is related to the energy of a line with rotational quantum number, J, through the following relation:

$$\begin{aligned} E_{J+i} &= E_J + i(1 + 2j + i)\big(B_0 - D_0 \times (2J(1 + J) + i + 2iJ + i^2)\big) \\ &= E_J + \Delta E_{J,J+i} \end{aligned} \qquad \text{Equation 4.16}$$

where B_0 and D_0 are rotational and centrifugal distortion constants, respectively. The values for these constants were determined for O_2 by Fletcher and Rayside (Fletcher and Rayside 1974), while Bendtsen (Bendtsen 1974) determined them for N_2. Using Equation 4.1 corrected for the ν^3 contribution, we can represent the intensity of $n + 1$ adjacent lines using a summation:

$$I'(J, n, T) = \sum_{i=0}^{n} I'_{J+n} = A\sigma \frac{N}{Q_R} e^{-\frac{E_J}{k_B T}} \times \sum_{i=0}^{n} S(J + i) g(J + i) f_{01}(J + i) e^{-\frac{\Delta E_{J,J+i}}{k_B T}} \qquad \text{Equation 4.17}$$

If we take the ratio of two sections of the VRR spectra, the first beginning at J_1 and including $n + 1$ lines and the second beginning at J_2 and including $l + 1$ lines, we get:

$$R'_{J_1,J_2,n,l} = \frac{\sum_{i=0}^{n} I_{J_1+n}}{\sum_{k=0}^{p} I_{J_2+p}} = e^{\frac{E_{J_2} - E_{J_1}}{k_B T}} \times F(J_1, J_2, n, p, T), \qquad \text{Equation 4.18}$$

where:

$$\mathrm{F(J_1}, J_2, \mathrm{n, l, T}) = \frac{\sum_{i=0}^{n} S(J_1 + i) g(J_1 + i) f_{01}(J_1 + i) e^{-\frac{\Delta E_{J,J+i}}{k_B T}}}{\sum_{l=0}^{p} S(J_2 + l) g(J_2 + l) f_{01}(J_2 + l) e^{-\frac{\Delta E_{J,J+l}}{k_B T}}}$$

We can then obtain an expression for temperature that is like Equation 4.10:

$$\mathrm{T_{mult}} = \frac{\mathrm{E_{J2}} - \mathrm{E_{J1}}}{\mathrm{k_B ln} \frac{\mathrm{R'_{J_1,J_2,n,l}}}{\mathrm{F(J_1, J_2, n, l, T)}}} \qquad \text{Equation 4.19}$$

Determining temperature with this formulation requires an iterative approach, similar to the multi-line analysis of Salzman, Masica, and Coney due to the dependence of $F(J_1, J_2, n, l, T)$ on temperature (Salzman et al. 1971). The analysis to determine temperature T_1 can be performed by calculating $F(J_1, J_2, n, l, T_0)$ using a starting temperature value, T_0, that is above 0 K. This can be repeated to calculate T_2 from $F(J_1, J_2, n, l, T_1)$ and then repeated continually until $\left(T_\eta - T_{\eta-1}\right)^2$ was less than the desired tolerance (we use 0.001 K), where η is the total number of iterations. The calculation converges to the final temperature value for any reasonable starting temperature; however, the number of iterations needed to calculate the final temperature is dependent on the difference between the final temperature and the starting temperature. We report results using $T_0 = 273$ K but found that we get the same results when T_0 is 1 K, 290 K, and 350 K. Using Equation 4.5, we were able to identify two sections of each VRR branch by selecting regions where line combinations are most consistent and precise with respect to the fit inferred temperatures (black dots). This was somewhat difficult for the O-branch of O_2, as the lines most in agreement with the fitting method were overlapped by the $^{16}O^{18}O$ Q-line. We were forced to use two small sections of the signal that were not spaced far apart. While the calculation can be performed on sections of different sizes, we opted to report calculations with two evenly sized sections of the spectra. We performed the analysis on each branch, and we report the lines used and wavenumber ranges in Table 4.7.

Table 4.7: Parameters used to determine the temperature from each branch in the VRR spectra for O_2 and N_2 using the multi-line ratio method. The top row shows the gas and branch (in parentheses). The rows represent the rotational quantum number (J) and wavenumber ranges (ν) used to estimate temperature using the multi-line ratio formulation.

	N_2 (O)	**N_2 (S)**	**O_2 (O)**	**O_2 (S)**	**Units**
$[J_1, J_1 + n]$	8-12	4-8	11-13	3-7	n/a
$[J_2, J_2 + p]$	20-24	16-20	15-17	19-23	n/a
$[\nu_1, \nu_1 + \nu_n]$	2232-2273	2369-2407	1473-1498	1573-1606	cm^{-1}
$[\nu_2, \nu_2 + \nu_p]$	2130-2173	2458-2495	1448-1474	1658-1688	cm^{-1}

Table 4.8: Comparison of the multi-line ratio approach to inferring temperature with the fitting method. The columns represent the gases and branch (in parentheses) used for inferring temperature. The rows in order on the number of iterations (η), the mean difference of the multi-line ratio and fitting methods ($\overline{T_{multi} - T_{fit}}$), the standard deviation of the multi-line ratio and fitting methods ($\sigma(T_{multi} - T_{fit})$), and the mean uncertainty of the multi-line ratio method ($\overline{\Delta T_{multi}}$).

	N_2 (O)	**N_2 (S)**	**O_2 (O)**	**O_2 (S)**
η	4	5	5	5
$\overline{T_{multi} - T_{fit}}$	0.0 K	-0.3 K	-0.2 K	-0.1 K
$\sigma(\overline{T_{multi} - T_{fit}})$	0.3 K	0.1 K	0.4 K	0.1 K
$\overline{\Delta T_{multi}}$	0.1 K	0.1 K	0.3 K	0.1 K

Table 4.8 shows that the multi-line ratio temperature values were consistent with respect to the fitting method to within 1 K, even for the O-branch of O_2. However, limitations on the O-branch of O_2 lead to lower precision than the other branches. A maximum of 5 iterations were needed to satisfy the minimization condition of the calculation. We have not seen any relation between the number of lines included in the calculation and the number of iterations required for convergence. The convergence appears stable, even when the number of iterations is increased well beyond the precision requirement. We also successfully applied the method to include different line counts in each part of the

ratio. Comparing Table 4.8 to Table 4.5 and Table 4.6, we can see that the precision with respect to the fit inferred temperature values is comparable to that of the best line combinations using the TLSR method. We assume adjacent line bias uncertainty to be negligible compared to photon statistics, so the intensity ratio's relative uncertainty, $(\Delta R'/R')^2$, reduces to the sum of inverse intensities. The uncertainty in temperature is calculated iteratively, starting with a null uncertainty. The only non-negligible sources of uncertainty in $F(J_1, J_2, n, l, T)$ are related to the non-rigid rotor corrections and each iteration's temperature. The mean uncertainty calculated across all experiments were comparable for all four branches.

4.4 Discussion

4.4.1 Comparing Methods of Inferring Temperature

We derived and implemented four methods to infer temperature from the VRR spectra of N_2 and O_2 and discussed their performance when compared to the least-squares regression method. We now broaden the scope of our analysis by comparing each of the methods described above with each other, as seen in Figure 4.8. We found that the temperatures determined by fitting the S- and O-branch of N_2 disagreed by at least 2.5 K. The reason for that is likely related to the fact that the VRR spectra of N_2 is less resolved than those of O_2, thus making the determination of the single line intensity less reliable. In particular, the resolution limitations might have affected the determination of b_0 from the VRR analysis, which was calculated from the same setup. We found that if a value of $b_0 = 0.55$ for N_2 is used, the difference in temperature values determined from fitting O- and S- branches separately drops to only a few tenths of a Kelvin. There is generally strong agreement between different measurement methods when comparing the results of the same VRR branch (<0.4 K), which indicates that a greater degree of consistency is attainable from the N_2 VRR spectra with improved instrument resolution.

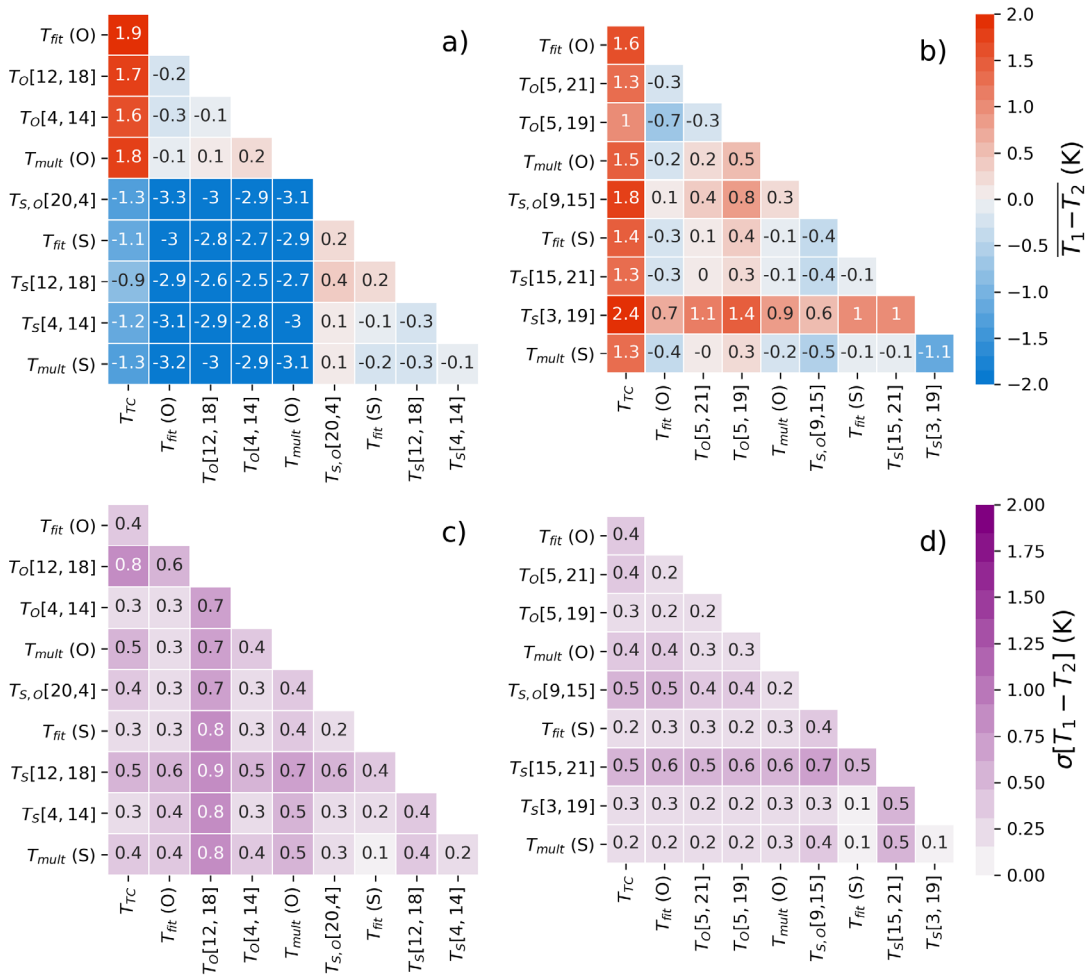

Figure 4.8: Comparisons of all the methods used to infer temperature from the VRR spectra are listed as: **(a)** The mean difference of all methods applied to the N_2 VRR spectra. **(b)** The mean difference of all methods applied to the O_2 VRR spectra. **(c)** The standard deviation of the difference of all methods applied to N_2. **(d)** The standard deviation of the difference of all methods applied to O_2. The temperature measurements compared are those from a collocated thermocouple (T_{TC}), fitting (T_{fit} (branch)), two-line, same branch, ratio ($T_{branch}[J_1,J_2]$), two-line, different branch, ratio ($T_{S,O}[J_s,J_o]$), and multi-line ratios (T_{mult} (branch)).

The comparative precision across all methods was ≤0.9 K for all cases involving the N_2 VRR spectra. Comparing the multi-line ratio and the fitting for the S-branch of N_2 suggests precision values as low as 0.1 K with respect to each other (consistent to within 0.2 K). Comparatively speaking, the different VRR methods are in much better

agreement for O_2 than for N_2. Several are within 0.1 K of each other and most fall within 0.5 K. The precision of these methods in comparison to each other is generally within 0.5 K, apart from the two-line ratios. It is apparent from Figure 4.8 that the two-line ratio method is generally worse in terms of precision in comparison to its counterparts for both gases, as we already noted earlier. Table 4.4 shows that the two-line ratio method is best applied to the S-Branch, as a lower proportion of lines were found to meet the <1 K criteria for the O-Branch and cross-branch estimates. Again, the most precise comparison (0.1K) is found by comparing the S-branch fit with the S-branch multi-line ratio approach. Fitting method, two-line ratios, and multi-line ratios are precise to within 1 K when applied to the VRR spectra of O_2. Additionally, each of these methods showed a high level of self-consistency to within 1 K. Overall, the methods we derived performed better when applied to O_2 VRR spectra than when applied to N_2 VRR spectra. While N_2 has greater abundance in the atmosphere, and therefore greater overall Raman signal, than O_2, the intensity of the lines within the O_2 spectrum are comparable to N_2 VRR transitions with even rotational quantum number. This is due largely to the nuclear spin statistic, g_J, which results in molecules having both even and odd rotational quantum number for N_2 and only odd rotational quantum number for O_2. Another effect of g_J is that the lines in the O_2 VRR spectrum have greater separation, are easier to resolve, and are less prone to adjacent line bias. Uncertainty due to adjacent line bias can be reduced by using methods that employ multiple lines, such as fitting the intensities or the multi-line ratio. However, high degrees of self-consistency and precision (<0.5 K) were still achievable using two-line ratios. Additionally, the precision of temperature values inferred from VRR spectra were small enough that temperature changes could be resolved over a relatively small temperature range.

4.4.2 Temperature Variation and Correlation

Across all experiments, the ambient temperature varied from 292.2 K to 293.3 K as measured by the thermocouple. Figure 4.9 compares the different methods we employed

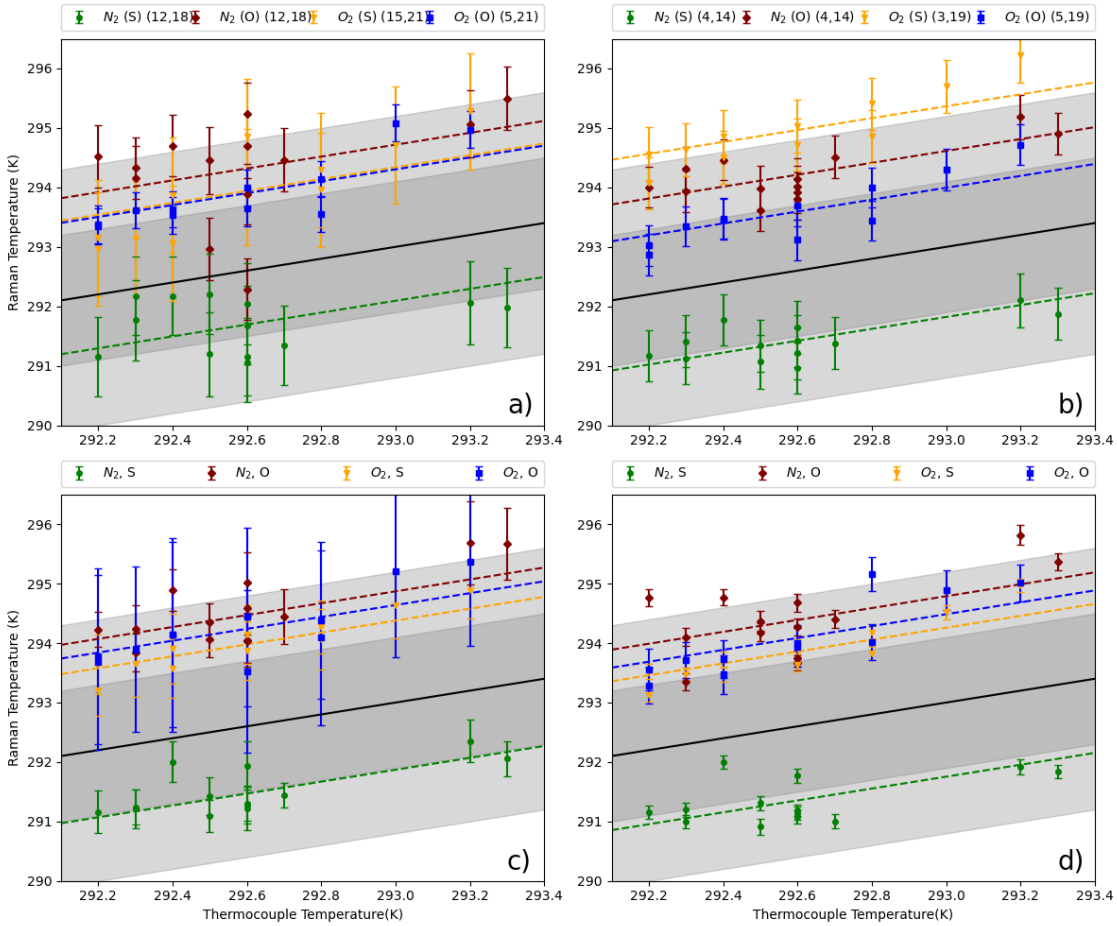

Figure 4.9: Temperature inferred from the VRR spectra plotted against the ranked temperature measured by the thermocouple, described by the following: **(a)** The line combinations most consistent with fitting method using the two-line, same branch, ratio. **(b)** Most precise line combinations with respect to the fitting method using two-line, same branch, ratio approach. **(c)** The temperature derived from fitting the VRR line intensities. **(d)** Temperatures determined by taking a ratio of multiple lines. The dark gray regions in each plot represent the 1 σ uncertainty of the thermocouple (1.1K) and the light gray regions represent the 2 σ uncertainty. The lines represent a line with a slope of 1.0, and linear regression was used to determine the offset with respect to the thermocouple

plotted with the ranked thermocouple readings. Most of the temperatures determined from Raman methods fall within the 95% confidence range of the thermocouple. As temperature increased in the room, increasing trends were also observed for the Raman calculations with varying degrees of correlation, as shown in Figure 4.10. Each

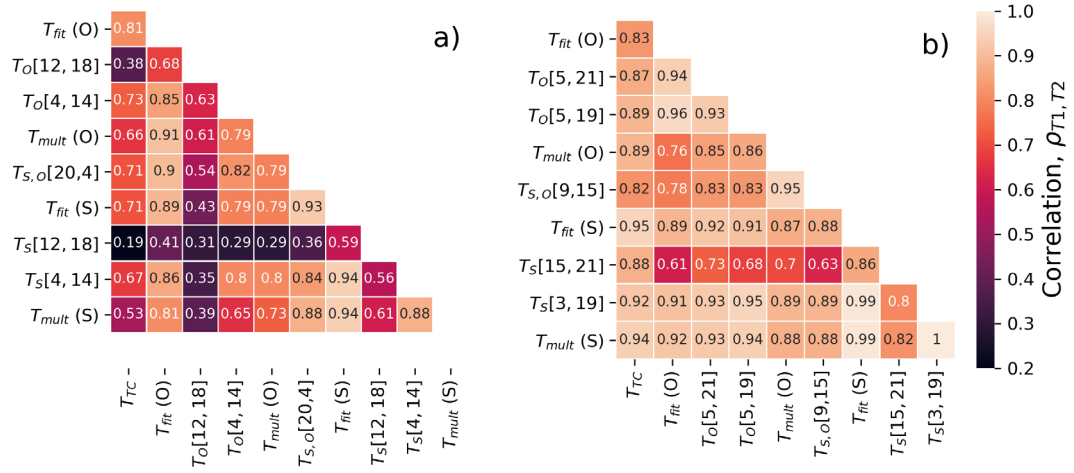

Figure 4.10: Pearson's correlation matrix composed of every method used to predict temperature from the VRR spectra of: **(a)** N_2 and **(b)** O_2. Labelling follows the same convention as Figure 4.8.

comparison shows a positive correlation and similar slopes over the temperature range explored. However, the correlations are higher for methods applied to O_2 VRR spectra than N_2 VRR spectra, especially the methods that involve two-line calculations. This is likely due to isolating single lines in the N_2 spectra being more difficult than for O_2. Overlap from adjacent lines reduces the overall precision of temperatures determined from isolated lines in the N_2 spectra. Additionally, temperature values inferred from the O_2 VRR spectra correlate better with the thermocouple than those inferred from the N_2 VRR spectra.

4.4.3 Additional Sources of Uncertainty

Temperatures determined from the S- and O-branch of O_2, along with the O-branch of N_2, are 1-3 K higher than those measured by the thermocouple. Furthermore, the temperature values determined from these three branches are in good agreement with each other. Despite large power densities in the scattering region, localized heating is unlikely. We estimate that over a 15-minute exposure, the temperature in the scattering region would only increase by 0.003 K at most. This estimate takes into account heating due to linear absorption, which is 0.2 Mm^{-1} in the atmosphere at 532 nm, and heat

dissipation (Whinnery 1974) (Arnott et al. 1999). Effects involving the motion of air in the room, the buoyancy of heated air, or absorption effects of aerosol were not considered. The first two effects would mitigate localized heating, and the third effect, which would would increase localized heating, is likely small. Again, most of the temperature values determined by analyzing the VRR spectra of O_2 and N_2 are within 2σ of the thermocouple's accuracy.

The instrumental transfer function, or the wavelength dependent intensity sensitivity of the detector in the spectrograph, represents a source of uncertainty in these experiments. The transfer function can be estimated experimentally by exposing the spectrograph to a black-body source or spontaneous emission from luminescent glasses (Hurst et al. 2007). These systems are often expensive, difficult to implement properly, and correction calibrations need to be performed often. These techniques can help diagnose the effects of distortions due to hot spots and etaloning (which is more of an issue in the near-infrared) (Choquette et al. 2007). Unable to perform these calibrations, we estimated the instrumental transfer function using the specifications of the spectrograph provided by the manufacturer. It is possible that the VRR transitions themselves could be used to improve this calibration in the future. Raj et al. recently showed how an intensity calibration could be performed using the intensity of PRR and VRR transitions (Raj et al. 2020). Additionally, further improvements could be achieved with a better alternative temperature measurement and by exploring a wider temperature range.

4.4.4 Generalizing the Results

We employed several methods of estimating atmospheric temperature from the VRR spectra of N_2 and O_2. These methods can be applied toward the development of instrumentation that can remotely infer temperature in turbid environments. In such applications, the investigated temperature values might be different, and the ranges might be wider than the temperature values we explored in this work. However, because our methods are reliant on the temperature dependence of the rotational states of a canonical gas through the Boltzmann distribution, these methods can be generalized to a greater

range of temperatures. For two-line ratios, a specific line pairing may only be appropriate for specific temperature values, especially if the intensity of one line becomes too small for a sensitive measurement to be made. The optimal line pairings for atmospherically relevant temperatures should be like those discussed in this work, as the intensities will not deviate enough to make them less sensitive. These optimal line pairings can be estimated using an approximated form of Equation 4.1:

$$I \propto Je^{\frac{-B_0 J^2}{k_B T}} = \sqrt{\frac{k_B T}{B_0}}\left(xe^{-x^2}\right), \text{ where } x = \sqrt{\frac{B_0}{k_B T}}J \qquad \text{Equation 4.20}$$

where B_0 is the rotational constant from Equation 4.16. The most intense line in the VRR spectra is for $x = 1/\sqrt{2}$, or $J_{max} = \sqrt{k_B T/B_0}$. Therefore, if J_1 and J_2 are the optimal J values obtained by comparing two single lines at T_0, then, the optimal J values at a different temperature T should be $J_1\sqrt{T/T_0}$ and $J_2\sqrt{T/T_0}$. In the same vein, the optimal line pairs of one gas can be estimated from the results of another, because J should scale as $\sqrt{1/B_0}$. From Table 4.5, we can surmise that [12, 18] is the optimal line pairing for N_2 when compared to the fitting method; plugging this line pairing into the $[J_1, J_2]\sqrt{B_{0,N_2}/B_{0,O_2}}$ relation, we estimated that for O_2, the optimal values $[J_1, J_2] = [14.1, 21]$.

Table 4.9: Estimates of the optimal line pairing for the two-line ratio method using the results from Table 4.5. These calculations were referenced to a temperature T_0, as discussed in the text, of 293 K.

T [K]	O_2 (S)	N_2 (S)
210	[13, 17]	[10, 16]
273	[15, 21]	[12, 18]
293	[15, 21]	[12, 18]
1000	[27, 29]	[22, 34]
2000	[39, 55]	[32, 48]

Since the O_2 VRR spectra only includes odd-J valued lines, it can be surmised that the estimated optimal line pairing for O_2 is [15, 21]. This indeed is the line pair that we found to be most in agreement with the fit for the S-Branch of O_2, as per Table 4.5 supporting our argument. Therefore, we used this method to calculate estimated optimal line pairs for determining the temperature for different temperature regimes and report the values in Table 4.9.

Similar conclusions can be extended to the multi-line ratio and line fitting methods as well. The multi-line ratio incorporates a greater number of photons compared to the two-line ratio methods and therefore should be more sensitive across a greater range of temperatures. However, the ideal line groupings may change in a similar fashion to the two-line ratio method discussed above. The temperature range of the line fitting method is largely limited to the spectral range of the spectrograph used. Line selection is less important for this method as well since the method is performed by minimizing the χ^2-statistic. This method is dependent on the relative uncertainty of each line and so would favor the lines with the highest intensity in the spectral range of the instrument.

The value of b_0 in the non-rigidity correction should be applicable to temperature regimes not explored in this work. There is no theoretical basis for temperature dependence of b_0, though experimental work should be performed to confirm this theoretical prediction (Herman and Wallis 1955; James and Klemperer 1959; Hamaguchi et al. 1981). Typically, experiments to determine b_0 are performed at room temperature, and these measurements are in-turn used to determine temperature at different temperature regimes (Asawaroengchai and Rosenblatt 1980; Hamaguchi et al. 1981; Langhoff et al. 1983; Borysow et al. 2019). It has been shown that this room temperature determined b_0 values do improve the accuracy of temperature measurements at flame temperatures (Michael C Drake and Rosenblatt 1978; Utsav and Varghese 2013).

4.5 Conclusions

Our experimental setup and measurement procedure allowed for high resolution measurement of VRR spectra of N_2 and O_2. Using the fundamental properties of these molecules, we were able to determine atmospheric temperature within the scattering region of our multi-pass cell. For both gases, treating the molecules as non-rigid rotors not only improved the self-consistency of temperature derived from Raman measurements but also improved the agreement between Raman derived temperatures and the thermocouple. However, the VRR spectra of O_2, specifically the S-Branch, would be best for determining atmospheric temperature with high precision without the need for ad hoc temperature calibration. The S-Branch provided the best results in this work, largely due to higher line intensities and a greater number of viable lines due to less influence from overlapping vibrational lines. We found that greater resolution is likely needed when determining temperature from individual N_2 lines. A more accurate estimate of b_0 might further improve the temperature inferred from N_2 VRR spectra. Regardless, the N_2 S-branch would likely provide the most precise temperature measurement for applications where a calibration can be performed. This is because this branch would have the strongest signal out of the four branches explored.

We derived four methods of ascertaining atmospheric temperature from the VRR spectra of N_2 and O_2. These methods could be a starting point in the development of an instrument for contactless measurements of atmospheric temperature using VRR spectra of N_2 or O_2, though further work is necessary to scale these methods to a field deployable instrument. Our analysis to find the optimal line combinations was performed for a limited range of temperature values. The best line combinations will need to be revisited for different temperature regimes, and we provided a theoretical approach to estimate the optimal line pairs. However, our work shows that regardless of temperature, well separated line combinations are ideal. Of the methods implemented in this work, the multi-line ratio is the best in terms of attainable precision and practical applicability. A future implementation would still require well-characterized filters that isolate specific

line combinations. A calibrated version of the multi-line method can also be envisioned, where two sections of the spectra are isolated and a calibration constant allows for temperature to be determined, just like in PRR methods. We anticipate that the VRR method would be applicable to the same range of temperatures that purely rotational Raman can be, since the formulation is similar. Methods employing interference filters would have orders of magnitude greater transmission than our spectrograph setup, which would allow for higher time resolution. It would be interesting to apply such a setup to investigate the effects of temperature fluctuations on atmospheric processes. Line-fitting and two-line ratios can also be effective techniques, though they may only be viable options when using a polychromator or other light dispersion techniques. These methods do not have the strict filter requirements of the multi-line method.

It is worth reiterating that VRR-based temperature measurement will not replace PRR-based temperature measurements. However, we believe there are situations where the elastic scattering signal will be too strong for PRR-based measurement to be reliable. Determining temperature from VRR spectra may be useful in the development of short-range LiDAR systems that investigate turbid environments, such as near clouds. Additionally, VRR spectra could be used for temperature measurements in combustion diagnostics, especially in cases where incomplete combustion leads to the production of particles that could increase the elastic scattering coefficient in the measurement media and degrade the precision of other techniques.

4.6 References

Arnott WP, Moosmuller H, Rogers CF, Jin TF, Bruch R. 1999. Photoacoustic spectrometer for measuring light absorption by aerosol: instrument description. Atmospheric Environment 33(17):2845-2852.

Asawaroengchai C, Rosenblatt GM. 1980. Rotational Raman intensities and the measured change with internuclear distance of the polarizability anisotropy of H2, D2, N2, O2, and CO. The Journal of Chemical Physics 72(4):2664-2669.

Bange J, Esposito M, Lenschow DH, Brown PRA, Dreiling V, Giez A, Mahrt L, Malinowski SP, Rodi AR, Shaw RA et al. . 2013. Measurement of Aircraft State and Thermodynamic and Dynamic Variables. p. 7-75.

Behrendt A, Reichardt J. 2000. Atmospheric temperature profiling in the presence of clouds with a pure rotational Raman lidar by use of an interference-filter-based polychromator. Applied Optics 39(9):1372-1378.

Behrendt A, Nakamura T, Onishi M, Baumgart R, Tsuda T. 2002. Combined Raman lidar for the measurement of atmospheric temperature, water vapor, particle extinction coefficient, and particle backscatter coefficient. Applied Optics 41(36):7657-7666.

Bendtsen J. 1974. The rotational and rotation-vibrational Raman spectra of 14N2, 14N15N and 15N2. Journal of Raman Spectroscopy 2(2):133-145.

Borysow J, Fink M. 2005. NIR Raman spectrometer for monitoring protonation reactions in gaseous hydrogen. Journal of nuclear materials 341(2-3):224-230.

Borysow J, Capek T, Mazzoleni C, Moraldi M. 2019. Corrections to the Raman fundamental band of N-2 and O-2 due to molecular non-rigidity: computations and experiment. Molecular Physics.

Buckingham AD, Szabo A. 1978. Determination of derivatives of the polarizability anisotropy in a diatomic molecule from relative Raman intensities. Journal of Raman Spectroscopy 7(1):46-48.

Chandrakar KK, Cantrell W, Chang K, Ciochetto D, Niedermeier D, Ovchinnikov M, Shaw RA, Yang F. 2016. Aerosol indirect effect from turbulence-induced broadening of cloud-droplet size distributions. Proceedings of the National Academy of Sciences of the United States of America 113(50):14243-14248.

Chandrakar KK, Cantrell W, Shaw RA. 2018. Influence of Turbulent Fluctuations on Cloud Droplet Size Dispersion and Aerosol Indirect Effects. Journal of the Atmospheric Sciences 75(9):3191-3209.

Choquette SJ, Etz ES, Hurst WS, Blackburn DH, Leigh SD. 2007. Relative Intensity Correction of Raman Spectrometers: NIST SRMs 2241 through 2243 for 785 nm, 532 nm, and 488 nm/514.5 nm Excitation. Applied Spectroscopy 61(2):117-129.

Cooney J. 1972. Measurement of Atmospheric Temperature Profiles by Raman Backscatter. Journal of Applied Meteorology 11(1):108-112.

Drake MC, Rosenblatt GM. 1976. FLAME TEMPERATURES FROM RAMAN-SCATTERING. Chemical Physics Letters 44(2):313-316.

Drake MC, Rosenblatt GM. 1978. Rotational Raman scattering from premixed and diffusion flames. Combustion and Flame 33:179-196.

Easter RC, Peters LK. 1994. Binary Homogeneous Nucleation: Temperature and Relative Humidity Fluctuations, Nonlinearity, and Aspects of New Particle Production in the Atmosphere. Journal of Applied Meteorology 33(7):775-784.

Fletcher WH, Rayside JS. 1974. High resolution vibrational Raman spectrum of oxygen. Journal of Raman Spectroscopy 2(1):3-14.

Hamaguchi H-O, Buckingham AD, Jones WJ. 1981. Determination of derivatives of the polarizability anisotropy in diatomic molecules. Molecular Physics 43(6):1311-1319.

Haumann J, Leipertz A. 1984. Flame-temperature measurements using the Rayleigh scattering photon-correlation technique. Optics Letters 9(11):487-489.

Herman R, Wallis RF. 1955. Influence of Vibration-Rotation Interaction on Line Intensities in Vibration-Rotation Bands of Diatomic Molecules. The Journal of Chemical Physics 23(4):637-646.

Herzberg G, Huber KP. 1979. Molecular Spectra and Molecular Structure. New York: Van Nostrand Reinhold Company.

Hoffman D, Munch KU, Leipertz A. 1996. Two-dimensional temperature determination in sooting flames by filtered Rayleigh scattering. Optics Letters 21(7):525-527.

Hurst WS, Choquette SJ, Etz ES. 2007. Requirements for Relative Intensity Correction of Raman Spectra Obtained by Column-Summing Charge-Coupled Device Data. Applied Spectroscopy 61(7):694-700.

James TC, Klemperer W. 1959. Line Intensities in the Raman Effect of 1Σ Diatomic Molecules. The Journal of Chemical Physics 31(1):130-134.

Keckhut P, Chanin ML, Hauchecorne A. 1990. STRATOSPHERE TEMPERATURE-MEASUREMENT USING RAMAN LIDAR. Applied Optics 29(34):5182-5186.

Kiefer W, Bernstein H, Wieser H, Danyluk M. 1972. The vapor-phase Raman spectra and the ring-puckering vibration of some deuterated analogs of trimethylene oxide. Journal of Molecular Spectroscopy 43(3):393-400.

Kulmala M, Rannik U, Zapadinsky EL, Clement CF. 1997. The effect of saturation fluctuations on droplet growth. Journal of Aerosol Science 28(8):1395-1409.

Langhoff SR, Bauschlicher CW, Chong DP. 1983. Theoretical-Study of the Effects of Vibrational-Rotational Interactions on the Raman-Spectrum of N2. Journal of Chemical Physics 78(9):5287-5292.

Lapp M, Penney CM, Goldman LM. 1973. Vibrational Raman scattering temperature measurements. Optics Communications 9(2):195-200.

Laurendeau NM. 1988. Temperature-Measurements by Light-Scattering Methods. Progress in Energy and Combustion Science 14(2):147-170.

Liu FC, Yi F. 2014. Lidar-measured atmospheric N-2 vibrational-rotational Raman spectra and consequent temperature retrieval. Optics Express 22(23):27833-27844.

Long DA. 1977. Raman Spectroscopy. New York, NY, USA: McGraw Hill.

Muppa SK, Behrendt A, Späth F, Wulfmeyer V, Metzendorf S, Riede A. 2016. Turbulent Humidity Fluctuations in the Convective Boundary Layer: Case Studies Using Water Vapour Differential Absorption Lidar Measurements. Boundary-Layer Meteorology 158(1):43-66.

Nilsson ED, Kulmala M. 1998. The potential for atmospheric mixing processes to enhance the binary nucleation rate. Journal of Geophysical Research: Atmospheres 103(D1):1381-1389.

Platis A, Altstädter B, Wehner B, Wildmann N, Lampert A, Hermann M, Birmili W, Bange J. 2016. An Observational Case Study on the Influence of Atmospheric Boundary-Layer Dynamics on New Particle Formation. Boundary-Layer Meteorology 158(1):67-92.

Radlach M, Behrendt A, Wulfmeyer V. 2008. Scanning rotational Raman lidar at 355 nm for the measurement of tropospheric temperature fields. Atmospheric Chemistry and Physics 8(2):159-169.

Raj A, Kato C, Witek HA, Hamaguchi H-o. 2020. Toward standardization of Raman spectroscopy: Accurate wavenumber and intensity calibration using rotational Raman spectra of H2, HD, D2, and vibration–rotation spectrum of O2. Journal of Raman Spectroscopy n/a(n/a).

Salzman JA, Masica WJ, Coney TA, States U, Administration NA, Space, Center LR. 1971. Determination of gas temperatures from laser-Raman scattering. Washington, D.C.; Springfield, VA: National Aeronautics and Space Administration ; For sale by the Clearinghouse for Federal Scientific and Technical Information.

Su J, McCormick MP, Lei L. 2020. New Technique to Retrieve Tropospheric Temperature Using Vibrational and Rotational Raman Backscattering. Earth and Space Science 7(4):e2019EA000817-e2019EA000817.

Utsav KC, Varghese PL. 2013. Accurate temperature measurements in flames with high spatial resolution using Stokes Raman scattering from nitrogen in a multiple-pass cell. Applied Optics 52(20):5007-5021.

Whinnery JR. 1974. Laser measurement of optical absorption in liquids. Accounts of Chemical Research 7(7):225-231.

Wulfmeyer V, Hardesty RM, Turner DD, Behrendt A, Cadeddu MP, Di Girolamo P, Schlüssel P, Van Baelen J, Zus F. 2015. A review of the remote sensing of lower tropospheric thermodynamic profiles and its indispensable role for the understanding and the simulation of water and energy cycles. Reviews of Geophysics 53(3):819-895.

5 Conclusions

5.1 Summary of Motivations

Aerosol's impact on radiative transfer represents a large source of uncertainty in climate models, and reducing these uncertainties has proven to be one of the toughest challenges in atmospheric science (Regayre et al. 2018; Bellouin et al. 2020). Atmospheric parameters, such as temperature and water vapor concentration, can have a large influence on the properties of aerosol and therefore on their impact on climate. The size and optical properties of hygroscopic aerosol, such as sea salt or mixed particles containing ammonium sulfate, are dependent on the local relative humidity. Quantifying the change in absorption of aerosol as a function of humidity has proven to be difficult. The reasons for this are two-fold: the traditional methods of obtaining absorption have poor performance at high relative humidity, and the available measurements of absorption enhancement span a large range of values depending on aerosol origin and age.

Fluctuations in relative humidity can affect how much light is scattered and absorbed by aerosol and, therefore, aerosol effects on the radiative balance of the planet. Absorption enhancements in humidified aerosol can also lead to local changes in temperature, a feedback which could suppress the formation of clouds. Due to lack a of data on humidity effects on light-absorbing aerosol, it is unclear how significant humidity related absorption enhancements are on these semi-direct aerosol effects. Fluctuations in temperature and humidity due to turbulence can also lead nonlinear responses in terms of aerosol optical properties, new particle formation, and activation of aerosol into cloud droplets. To investigate the links between aerosol properties, relative humidity, and turbulence, new methods of remotely measuring temperature and water vapor are necessary.

5.2 Summary and Implications

This dissertation describes research activities aimed at better understanding the complex effects water vapor and temperature can have on aerosol. Novel measurement methods were developed to directly measure the optical effects of water uptake on aerosol. Additionally, the first steps were taken toward the end goal of understanding the role of turbulence in on relative humidity and, therefore, on aerosol through the development of a method to noninvasively measure temperature.

A novel humidified cavity attenuated phase shift albedometer (H-CAPS-PM_{SSA}) is described and characterized in Chapter 2. We found sensitivities and measurement capabilities like those in Onasch et al. (Onasch et al. 2015), despite evidence that certain key parameters within the instrument might drift (Modini et al. 2020). Such characterizations enabled us to confidently perform measurements at high RH using the H-CAPS-PM_{SSA}. A custom software package to correct for size-dependent truncation biases was also described, and then compared to biases measured from aerosol. We found that the software underpredicted these biases because it does not account for the reflections on the glass tube within the instrument (Liu et al. 2018; Modini et al. 2020). Two empirical corrections were formulated: one based on aerosol diameter and one based on Mie calculations. While the Mie-based correction predicted the dry data better, the diameter-based empirical formula performed better when compared to humidified data. The diameter parameterization is applied to the humidified data in Chapter 3, as well as in Carrico et al (Carrico et al. 2021). The diameter-based empirical formula also had lower uncertainty, which was comparable to the uncertainty predicted by Onasch et al. (Onasch et al. 2015).

The H-CAPS-PM_{SSA} was used to measure the optical and hygroscopic properties of ammonium sulfate, nigrosin, and ammonium sulfate-nigrosin mixtures with molar ratios of 1:1 and 4.7:1. The refractive indices of nigrosin and the two mixtures were determined from scattering and extinction data, while the H-CAPS-PM_{SSA} was operated in dry mode. The refractive index of nigrosin agreed with values reported in literature. The refractive

indices of the mixtures were also compared to volume averages of the ammonium sulfate (from literature) and nigrosin refractive indices, and these were in good agreement as well. Next, least-squares and Monte Carlo analyses was performed on humidified extinction data for each aerosol species to determine their respective hygroscopic parameters, κ, as a function of relative humidity. For aerosol containing ammonium sulfate, κ decreased as relative humidity decreased. This is predicted for ammonium sulfate, as κ for the whole particle is dependent on the concentration of ammonium sulfate (Lewis 2019). However, this decrease was much steeper than expected for the mixtures based on hygroscopic volume mixing rules (Petters and Kreidenweis 2007). We also analyzed the change in single scattering albedo as humidity was increased. The greatest change in single scattering albedo was observed for the 4.7:1 ammonium sulfate to nigrosin mixture, whereas the lowest change in single scattering albedo was observed for pure ammonium sulfate. A parameterization scheme was developed to describe the single scattering albedo enhancement as a function of relative humidity and the volume fraction of nigrosin using an empirical quadratic relation. We also parameterize the absorption enhancement in terms of scattering enhancements. The parameterizations discussed in Chapter 3 could be used to estimate forcing of atmospheric aerosols. Parameterizing single scattering albedo enhancements based on the volume fraction of absorbing aerosol could be a powerful tool for modelling aerosol containing light-absorbing material in high RH environments. The parameterization uses only one fitting parameter, a, which is strongly dependent on the hygroscopicity of the two material.

For the purposes of quantifying the effects of relative humidity fluctuations and how they affect the optical properties of aerosol, novel means of remote temperature and water vapor measurements were developed. My contributions mostly focused on the temperature measurement; however, lab experiments looking into water vapor measurements were performed by Chibirev et al. (Chibirev et al. 2018). The results of this work are discussed in Chapter 4. We examined three different methods for inferring temperature from the vibro-rotational Raman (VRR) spectra of O_2 and N_2. The first method used linear regression to fit the intensities of lines within the VRR spectra using

the Maxwell-Boltzmann relation. This method was used to show the importance of correcting for non-rigidity when analyzing VRR spectra. Then, we developed a method to estimate temperature by taking a ratio of line intensities from any line in the VRR spectra of N_2 or O_2. Some key observations from this analysis were that the method performs best when the lines are selected from the same branch and is more precise when the lines are well spectrally separated from each other. Building off the two-ratio formulation and inspired by modern lidar techniques (Radlach et al. 2008) and the work of Salzman, Masica, and Coney (Salzman et al. 1971), we developed an expression for determining the temperature by taking ratios of multiple lines. This method has the advantage of increasing the number of photons used for the temperature calculation, thereby reducing photon counting statistics, as well as reducing the uncertainty resulting from overlapping lines. This method was found to be precise and self-consistent with the regression method. This method also has the advantage of being more straightforwardly scalable to the development of an imaging technique, development which will continue in the future.

5.3 Future Direction

5.3.1 Truncation Correction Software

The next software upgrade to be incorporated will consider the reflectivity of the cell into the custom software, similar to Modini et al.'s FORTRAN software (Modini et al. 2020). Additionally, the software was written with the goal of being used to predict truncation in instruments other than the H-CAPS-PM_{SSA}. Further empirical corrections to the Mie based truncation code may be necessary for experiments involving irregularly shaped aerosol, such as soot. Future work will also be done to test the software's ability to predict truncation in other instruments that measure scattering, such as those containing integrated nephelometers.

5.3.2 Humidification Experiments using H-CAPS-PM_{SSA}

Experiments to characterize the absorption characteristics of soot at medium to high relative humidity values are the next logical step for the H-CAPS-PM_{SSA}. Such an experiment would be performed by using a stable source for soot, such as the Argonaut inverted burner located at Los Alamos Laboratory, by controlling the fuel to air ratio. Soot will then be dried in a diffusion drier and then charge- and mass-selected using a SMPS and CPMA, like experiments in Chapters 2 and 3. To make soot more hygroscopic, we could expose the soot to a chamber of nitric or sulfuric acid. If the acid vapor pressure is near saturation, it will deposit onto the soot, making it more hydrophilic. We would then measure the Extinction and Scattering using the H-CAPS-PM_{SSA} at elevated relative humidity values. This could be compared to similar experiments where the acids are not used and water growth is expected to be minimal. Additionally, photochemical aging processes in the atmosphere could be simulated using the Potential Aerosol Mass (PAM) Oxidation Flow Reactor. The PAM reactor is a highly oxidizing chamber that simulates several days' worth of aging in the matter of minutes. Ancillary measurements are critical to the success of this experiment. For example, microscopy samples will be collected to quantify morphology of particles entering the CAPS. Modifications could be made to the CAPS to look at how humidity modifies aerosol morphology. The three-wavelength photoacoustic instrument will be critical for comparisons of SSA with the H-CAPS-PM_{SSA}. It may also be important for quantifying truncation related errors in the measurement, like how it was used for nigrosin in Chapter 2. This is due to the complex morphology of soot particles and how it affects the fraction of back scattered light to forward scattered light. Liu et al. found that the truncation correction was also strongly dependent on the asymmetry parameter (fraction of light backscattered to front scattered) of the aerosol put into the instrument (Liu et al. 2018). However, the photoacoustic cannot be humidified, so an empirical correction may be necessary based on aerosol morphology determined from microscopy measurements from which the asymmetry parameter could be estimated. Soot could then be parameterized in a similar fashion to the nigrosin ammonium sulfate mixtures from Chapter 3.

Expanding this parameterization beyond the 200-500nm range for the quadratic parameterization discussed in Chapter 3 is another major challenge. This will likely involve adding another fit parameter that accounts for aerosol diameter. SSA enhancements could also be combined with mass spectroscopy measurements to develop a parameterization scheme based on the organic carbon mass (OCM) ratio of the aerosol. Hygroscopicity tends to be lower for aerosol containing large amounts of carbonaceous material (Carrico et al. 2005, Malm, 2005 #727; Orozco et al. 2016). The carbon content of an aerosol can also be used to accurately predict SSA of freshly emitted biomass burning plumes (Pokhrel et al. 2016). Such parameterization schemes could be used to predict the SSA of brown carbon at elevated humidity, which currently is still not well characterized (Washenfelder et al. 2013). Brown carbon can become less absorptive and more hygroscopic due to oxidation and aging processes, so parameterizations based on chemical content are important (Forrister et al. 2015; Gorkowski et al. 2019).

5.3.3 Improving Rigid Rotor Corrections for N_2

When comparing the temperature inferred from the S-branch to those from the O-branch, the agreement is more consistent for N_2 than for O_2. This is likely the cause of the greater degree of overlap for the N_2 spectrum affecting the determination of temperature and the rigid rotor correction. By varying b_0 (the ratio of the polarizability anisotropy and its first derivative at the equilibrium inter-nuclear distance), we found the agreement between S- and O-branch inferred temperatures was optimized when $b_0 = 0.55$ ($\Delta T_S - \Delta T_O = -0.3K$). The value of for b_0 used for the estimation of the temperature from the N_2 spectra was determined taking ratios of lines $J \rightarrow J+2$ in the S-branch to $J \rightarrow J-2$ in the O-branch (expressed as Z^2) and fitting them to the rotational quantum number, J (Borysow et al. 2019). To account for overlap related errors, the same fitting scheme was applied with the addition of an intercept term to account for vertical shifts from data biases. A comparison of each fitting scheme, with and without the intercept term, is given in Figure 5.1. The b_0 value determined from the fit is nearly in agreement with the value derived from optimizing the temperature results and would result in temperatures

determined from the S- and O-branches being in greater agreement than if $b_0 = 0.48$. The difference in b_0 values predicted from temperature optimization and fitting with an intercept could be because the optimization scheme does not correct for biases due to overlap from adjacent line profiles. It is not entirely clear if this fitting scheme is accounting for bias in the data or if there is an additional term from the third-order perturbation derivation not being considered that should be for N_2. Future work should be done to confirm these results using a higher resolution spectrograph and refining the theoretical treatment of the Raman spectra, should it need be.

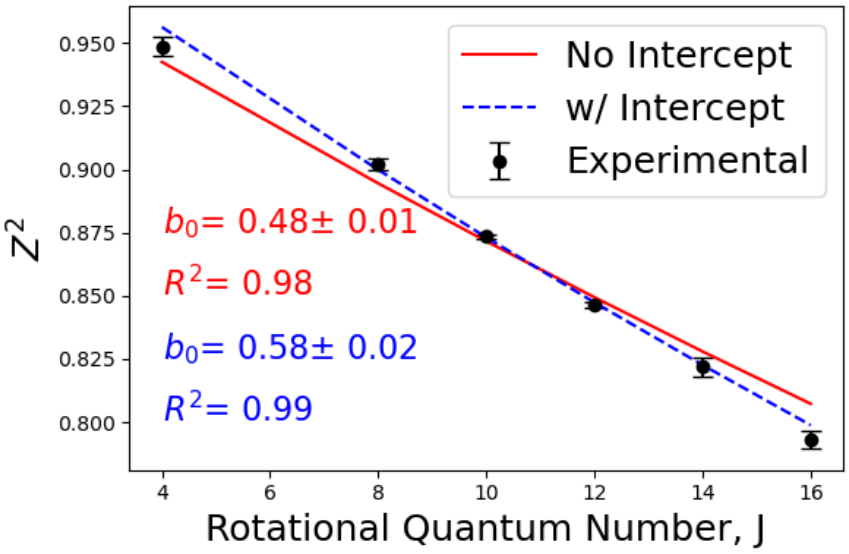

Figure 5.1: A comparison of least-squares regressions to determine rigid rotor correction term, b_0. The vertical axis represents the ratio of line intensities measured in the S- and O-branches. The expressions used for regression are identical save for an additional intercept term (blue) to account for biases resulting from overlapping lines. The intercept adjustment found in the blue fit was 0.024±0.006.

Determining temperature from the VRR spectra of N_2 and O_2 is part of a greater effort to quantify the effect turbulence has on aerosol and cloud droplets in the Michigan Tech Cloud Chamber (Π-Chamber). The instrument, which we refer to as the Ramanographer, will map the water vapor field and temperature to quantify the spatial and temporal variation of relative humidity within the Π-Chamber. To accomplish the mapping aspect,

thermoelectrically cooled CCD cameras (Andor iKon-M) will be used to image a $10x10cm^2$ area. Temperature measurements will be performed by isolating two sections of the VRR spectrum using narrow band-pass filters and imaging the transmitted light using two separate cameras. This method would be like the multi-line approach, which we found could be sensitive to within 3K using an integration time of 1s. This estimate is based on photon collection rates from the results of Chapter 4. However, the estimate does not consider the improved transmission of the Ramanographer compared to the spectrograph (at least an order of magnitude). As such, we estimate that the sensitivity using this approach in the Ramanographer could be lower than 1K. Water vapor concentration will be determined by isolating and imaging the vibrational bands of water vapor and N_2, and their ratio will be used to determine the water vapor concentration in the Π-Chamber. Cameras with band-pass filters centered on the elastic scattering will be used to image the elastic scattering off aerosol and cloud droplets, and these cameras could be positioned to measure light scattered in the forward, back, or perpendicular direction to estimate hygroscopic growth.

5.3.4 Raman Measurements in the Π-Chamber

While the end goal of the project is to measure the effects of turbulence on aerosol, an important first step of the instrument could be to show the dependence of relative humidity fluctuations on the covariance of vapor pressure and temperature derived by Kulmala (Kulmala et al. 1997). Such an experiment could be performed in a clean environment (minimal aerosol or cloud droplets) within the Π-Chamber, and such an experiment would allow for fine tuning of the instrument to reduce the effect of reflections from surfaces within the Π-Chamber. Then, aerosol and cloud droplet measurements could be performed. One such experiment could involve injecting ammonium sulfate into the cloud chamber and operating it in turbulent mixing mode while keeping the average relative humidity below 81%. Deliquescence observed by enhanced scattering from the elastic scattering cameras could then be related to regions that have elevated RH due to mixing processes. An interesting observation might be to

look at how the scattering enhancements evolve over time and whether the aerosol adsorb enough water to reduce the humidity to the point that aerosol stop deliquescing. Another potential experiment of interest to this work would be to look at how cloud processing affects the optical and hygroscopic properties of aged soot. This could be explored by deploying the H-CAPS-PM_{SSA} in the Π-Chamber facility to measure the optical properties of soot before and after cloud processing. Varying degrees of turbulence could be attained by adjusting the temperature differential within the Π-Chamber, which could then be quantified using temperature fluctuation data from the Ramanographer. Compaction and chemical processing of soot particles within the cloud chamber could alter both the optical and hygroscopic properties of the soot, which would be quantified using the H-CAPS-PM_{SSA} (Bhandari et al. 2019). This could lead to exciting developments in understanding cloud processing of soot and how cloud processing transforms the properties of the soot.

5.4 References

Bellouin N, Quaas J, Gryspeerdt E, Kinne S, Stier P, Watson-Parris D, Boucher O, Carslaw KS, Christensen M, Daniau AL et al. . 2020. Bounding Global Aerosol Radiative Forcing of Climate Change. Reviews of Geophysics 58(1).

Bhandari J, China S, Chandrakar KK, Kinney G, Cantrell W, Shaw RA, Mazzoleni LR, Girotto G, Sharma N, Gorkowski K et al. . 2019. Extensive Soot Compaction by Cloud Processing from Laboratory and Field Observations. Scientific Reports 9.

Borysow J, Capek T, Mazzoleni C, Moraldi M. 2019. Corrections to the Raman fundamental band of N-2 and O-2 due to molecular non-rigidity: computations and experiment. Molecular Physics.

Carrico CM, Kreidenweis SM, Malm WC, Day DE, Lee T, Carrillo J, McMeeking GR, Collett JL. 2005. Hygroscopic growth behavior of a carbon-dominated aerosol in Yosemite National Park. Atmospheric Environment 39(8):1393-1404.

Carrico CM, Capek TJ, Gorkowski KJ, Lam JT, Gulick S, Karacaoglu J, Lee JE, Dungan C, Aiken AC, Onasch TB et al. . 2021. Humidified Single Scattering Albedometer (H-CAPS-PMSSA): Design, Data-Analysis, and Validation. Aerosol Science and Technology:1-25.

Chibirev I, Mazzoleni C, van der Voort DD, Borysow J, Fink M. 2018. Raman spectrometer for field determination of H2O in natural gas pipelines. Journal of Natural Gas Science and Engineering 55:426-430.

Forrister H, Liu J, Scheuer E, Dibb J, Ziemba L, Thornhill KL, Anderson B, Diskin G, Perring AE, Schwarz JP et al. . 2015. Evolution of brown carbon in wildfire plumes. Geophysical Research Letters 42(11):4623-4630.

Gorkowski K, Preston TC, Zuend A. 2019. Relative-humidity-dependent organic aerosol thermodynamics via an efficient reduced-complexity model. Atmospheric Chemistry and Physics 19(20):13383-13407.

Kulmala M, Rannik U, Zapadinsky EL, Clement CF. 1997. The effect of saturation fluctuations on droplet growth. Journal of Aerosol Science 28(8):1395-1409.

Lewis ER. 2019. The Dependence of Radius on Relative Humidity and Solute Mass at High Relative Humidities Up to and Including 100%. Journal of Geophysical Research-Atmospheres 124(4):2105-2126.

Liu F, Snelling DR, Thomson KA, Smallwood GJ. 2018. Estimate of scattering truncation in the cavity attenuated phase shift PMSSA monitor using radiative transfer theory. Aerosol Science and Technology 52(5):588-596.

Modini RL, Corbin JC, Brem BT, Irwin M, Bertò M, Pileci RE, Fetfatzis P, Eleftheriadis K, Henzing B, Moerman MM et al. . 2020. Detailed characterization of the CAPS single scattering albedo monitor (CAPS PMssa) as a field-deployable instrument for measuring aerosol light absorption with the extinction-minus-scattering method. Atmos. Meas. Tech. Discuss. 2020:1-56.

Onasch TB, Massoli P, Kebabian PL, Hills FB, Bacon FW, Freedman A. 2015. Single Scattering Albedo Monitor for Airborne Particulates. Aerosol Science and Technology 49(4):267-279.

Orozco D, Beyersdorf AJ, Ziemba LD, Berkoff T, Zhang Q, Delgado R, Hennigan CJ, Thornhill KL, Young DE, Parworth C et al. . 2016. Hygrosopicity measurements of aerosol particles in the San Joaquin Valley, CA, Baltimore, MD, and Golden, CO. Journal of Geophysical Research: Atmospheres 121(12):7344-7359.

Petters MD, Kreidenweis SM. 2007. A single parameter representation of hygroscopic growth and cloud condensation nucleus activity. Atmospheric Chemistry and Physics 7(8):1961-1971.

Pokhrel RP, Wagner NL, Langridge JM, Lack DA, Jayarathne T, Stone EA, Stockwell CE, Yokelson RJ, Murphy SM. 2016. Parameterization of single-scattering albedo (SSA) and absorption Angstrom exponent (AAE) with EC / OC for aerosol emissions from biomass burning. Atmospheric Chemistry and Physics 16(15):9549-9561.

Radlach M, Behrendt A, Wulfmeyer V. 2008. Scanning rotational Raman lidar at 355 nm for the measurement of tropospheric temperature fields. Atmospheric Chemistry and Physics 8(2):159-169.

Regayre LA, Johnson JS, Yoshioka M, Pringle KJ, Sexton DMH, Booth BBB, Lee LA, Bellouin N, Carslaw KS. 2018. Aerosol and physical atmosphere model parameters are both important sources of uncertainty in aerosol ERF. Atmos. Chem. Phys. 18(13):9975-10006.

Salzman JA, Masica WJ, Coney TA, States U, Administration NA, Space, Center LR. 1971. Determination of gas temperatures from laser-Raman scattering. Washington, D.C.; Springfield, VA: National Aeronautics and Space Administration ; For sale by the Clearinghouse for Federal Scientific and Technical Information.

Washenfelder RA, Flores JM, Brock CA, Brown SS, Rudich Y. 2013. Broadband measurements of aerosol extinction in the ultraviolet spectral region. Atmospheric Measurement Techniques 6(4):861-877.

A Python Truncation Estimation (caps_trunc.py)

```
import numpy as np
import PyMieScatt as ps
from scipy.integrate import trapz

def settings(waveLength=450, diamSphere=10, diamTube=1.0, extraLength=0.6, angRes=0.2,
calBool = False, calDiam = 150, cal_NDp = 1, calRI=1.53):
        """
        This function allows for fully custumizable instrument settings that get input
        into the truncation correction functions. calBool should be set to True is any
        setting is changed.
        Parameters
        ----------
        diamSphere : float, optional
                diameter of integrating tube in CAPS in cm. The default is 10.
        diamTube : float, optional
                diameter of tube in CAPS in cm. The default is 1.0.
                extraLength : float, optional
                length outside both sides of integrating sphere calculation is performed
                (cm). The default 0.6.
        angRes : float, optional
                angular resolution of Mie calculations.. The default is 0.2.
        calBool: boolean, optional
                Boolean to determine whether new calibration value is necessary. Use if
                calDiam, cal_nDp, or calRI are different thant their default values.
                Default values assume that theinstrument was calibrated using a
                monodisperse sample of 150nm Ammonium Sulfate. The is False.
        calDiam: : float or array, optional
                Diameter of calibration aerosol. float data type will calculate
                calibration factor assumingmonodisperese aerosol, while array will
                calculate calibration factor assuming polydispersesize distribution. For
                polydisperse, cal_nDp is used as weighting factor. Ensure that arrays
                input for calDiam and cal_ndp are the same size. The default is 150nm.
        cal_nDp : float or array, optional
                Weights for size distribution of calibration aerosol. float data type will
                calculatecalibration factor assuming monodisperese aerosol, while array
                will calculate calibrationfactor assuming polydisperse size distribution.
                For polydisperse, cal_nDp is used as factor. Ensure that arrays input for
                calDiam and cal_ndp are the same size. The value is 1.
        Returns
        -------
        default_dict : dict
                Dictionary containing the default instrument values for calculating
                truncation. From the input parameters, the dictionary also includes z-axis
                integration limits and density:
                        z1: lower limit of z-axis integral: -0.5*diamSphere-extraLength
                        z2: upper limit of z-axis integral: 0.5*diamSphere+extraLength
                        npos: Integration density:
                        int((100/11.2)*(diam_sphere+2*extra_length))
        """
        if extraLength < 0.0:
                extraLength = 0.0
                print('extraLength must be set to value exceeding 0.0.'+\
                        ' extraLength set to 0.0 for this calculation.')
        else:
                pass
        if calBool == True:
                default_dict = {'wavlen': waveLength,\
                                'diam_sphere': diamSphere,\
                                'diam_tube': 1.0,\
                                'extra_length': 0.6,\
                                'z1': -0.5 * diamSphere - extraLength,\
```

```
                        'z2': 0.5 * diamSphere + extraLength,\
                        'npos': int((100/11.2) * (diamSphere + 2 * extraLength)),\
        if np.size(calDiam) == 1:
                truncCal = trunc_mono(calRI, calDiam, False, default_dict)
        else:
                truncCal = trunc_size_dist(calRI, calDiam, cal_NDp, False, default_dict)
                default_dict['trunc_cal'] = truncCal
        else:
                default_dict = {'wavlen': waveLength,\
                        'diam_sphere': diamSphere,\
                        'diam_tube': 1.0,\
                        'extra_length': 0.6,\
                        'z1': -0.5 * diamSphere - extraLength,\
                        'z2': 0.5 * diamSphere + extraLength,\
                        'npos': int((100/11.2) * (diamSphere + 2 * extraLength)),\
                        'ang_res': angRes,
                        'trunc_cal': 1.02245612148504}
        return default_dict
def trunc_mono(n, diam_aerosol, fullOutput=False, inst_settings = settings()):
        """
        Compute the SSA correction due to truncation for the CAPS-PM-SSA for monodisperse
        aerosol. The truncation follows as the inverse of the SSA correction given.Uses
        Bohren-Huffman Mie algorithm, via PyMieScatt, to compute the correction given
        aerosol index of refraction, aerosol diameter, and wavelength. A truncated and
        ideal Mie scattering efficiency several points within the geometry of the CAPS,
        and then integrated. The correction is derived a ratio of the integrals (ideal
        case in the numerator). The results are normalized to the truncation calculated
        for 150nm monodisperse aerosol. Informaiton about the z axis points used in the
        calculation, Mie scattering efficiencies, and angles used to compute truncated Mie
        scattering efficiencies can be output by setting fullOutput=True.

        Parameters
        ----------
        n: complex float
                Complex refrative index of the aerosol.
        diam_aerosol: float
                Diameter of monodisperse aerosol.
        wavlen: float, optional
        fullOutput: boolean, optional
                Outputs Scattering efficiencies, z-axis values, and angles of integration
                with correction.

        Returns
        -------
        trunc_corr: float
                Truncation for CAPS SSA measurement assuming monodisperse aerosol
        if fullOutput=True also outputs
                z_axis: array of floats
                        z-axis positions of particles within cavity. Units are in cm.
                qsca_trunc: float
                        Truncated scattering efficiency. Integrated from theta1 to theta2
                        across all z-axis values.
                qsca_ideal: float
                        Non-truncated scattering efficiency. Integrated from 0-180 degrees
                        z-axis values inside integrating sphere. Considered zero outside of
                        limits of the integrating sphere.
                theta1: array of floats
                        Forward scattering angle in radians of integration, truncated by
                        opening on far side of cavity.
                theta2: array of floats
                        Backward scattering angle in radians truncated by opening on near
                        side of cavity.
        """
        wavlen, diam_sphere, diam_tube, extra_length, z1, z2, npos, ang_res, trunc_cal =\
                inst_settings.values()
        size_param = (np.pi * diam_aerosol)/wavlen #size parameter
```

```
theta, _, _, su = ps.ScatteringFunction(n, wavlen, diam_aerosol, minAngle=0,
maxAngle=180, angularResolution=ang_res)
#Do not set angular resolution higher than 0.1

z_axis = np.linspace(z1, z2, npos)
theta1 = np.zeros(len(z_axis))
theta2 = np.zeros(len(z_axis))
qsca_trunc = np.zeros(len(z_axis))
qsca_ideal = np.zeros(len(z_axis))
i = 0
for z in np.nditer(z_axis):
        if z != 0.5 * diam_sphere:
                alpha = np.arctan((0.5*diam_tube)/abs(0.5*diam_sphere - z))
                #forward scattering angle
        else:
                pass
        if z != -0.5 * diam_sphere:
                beta = np.arctan((0.5*diam_tube)/abs(-0.5*diam_sphere - z))
                #back scattering angle
                #alpha and beta need to be adjusted based on section of cell we are
        in
        if z < -0.5 * diam_sphere:#outside of sphere
                theta1[i] = alpha
                theta2[i] = beta
                qsca_ideal[i] = 0 #ideally light would not get into cavity from
        outside
        elif z == -0.5 * diam_sphere:
                theta1[i] = alpha
                theta2[i] = np.pi/2
                qsca_ideal[i] = q_mie
        elif -0.5 * diam_sphere <= z <= 0.5 * diam_sphere:#inside cavity
                theta1[i] = alpha
                theta2[i] = np.pi - beta
                qsca_ideal[i] = q_mie #ideally full scattering efficiency measured
        elif z == 0.5 * diam_sphere:
                theta1[i] = np.pi/2
                theta2[i] = np.pi - beta
                qsca_ideal[i] = q_mie #ideally full scattering efficiency measured
        elif z > 0.5 * diam_sphere:
                theta1[i] = np.pi - alpha
                theta2[i] = np.pi - beta
                qsca_ideal[i] = 0 #ideally light would not get into cavity from
        outside
        su_trunc = su[np.where(np.logical_and(theta >= theta1[i], theta <=
                                                                theta2[i]))]
        theta_trunc=theta[np.where(np.logical_and(theta>=theta1[i],\
                                                        theta<=theta2[i]))]
        #calculate scattering efficiency
        qsca_trunc[i]=trapz((2*su_trunc*np.sin(theta_trunc))/size_param**2,\
                                theta_trunc)
        i+=1
trunc = trapz(qsca_trunc, z_axis)
ideal = trapz(qsca_ideal, z_axis)
#calculate trunc_corr. For regular calculations calculate top line. If determining
#truncation determining correction factor for calibrated data uncomment second
line, #comment #first line and determine the truncation correction
trunc_corr = (ideal / trunc)/trunc_cal
if fullOutput == True:
        return trunc_corr, z_axis, qsca_trunc, qsca_ideal, theta1, theta2
else:
        return trunc_corr
```

```
def trunc_lognorm(n,gmean,gstd,fullOutput=False,returnDist=False,\
                  inst_settings =settings()):
        """
        Compute the SSA correction due to truncation for the CAPS-PM-SSA for polydisperse
        aerosol with lognormal shape. The truncation follows as the inverse of the SSA
        correction given.

        Uses Bohren-Huffman Mie algorithm, via PyMieScatt, to compute the correction given
        aerosol index of refraction, aerosol distribution statistics, and wavelength. This
        function is built as a wrapper around trunc_size_dist, so a size distribution is
        generated for given geometric mean (gmean) and geometric standard deviation
        (gstd). A truncated and ideal Mie scattering coefficient is calculated at several
        points within the geometry of the CAPS, and integrated. The correction is derived
        from a ratio of the integrals (ideal case in the numerator). The results are
        normalized to the truncation calculated for 150nm monodisperse aerosol.
        Informaiton about the z axis points in the calculation, Mie scattering
        coefficeints, and angles used to compute truncated Mie scattering coefficients can
        be output by setting fullOutput=True.

        Parameters
        ----------
        n : complex float
                Refractive index of aerosol
        gmean : float
                Geometric mean of aerosol distribution
        gstd : float
                Geometric standard deviation of aerosol distribution. Must be greater than
        1.0.
        wavlen : float, optional
                Wavelength of light source. The default is 450.
        fullOutput : boolean, optional
                If True, outputs angular, positional, and scattering coefficient data. The
                default is False.

        Returns
        -------
        trunc_corr: float
                Truncation for CAPS SSA measurement assuming monodisperse aerosol
        if fullOutput=True also outputs
                z_axis: array of floats
                        z-axis positions of particles within cavity. Units are in cm.
                bsca_trunc: float
                        Truncated scattering coefficient. Integrated from theta1 to theta2
                        across all z-axis values.
                bsca_ideal: float
                        Non-truncated scattering coefficient. Integrated from 0-180 degrees
                        z-axis values inside sphere. Considered zero outside of limits of
                        the integrating sphere.
                theta1: array of floats
                        Forward scattering angle in radians of integration, truncated by
                        opening on far side of cavity.
                theta2: array of floats
                        Backward scattering angle in radians truncated by opening on near
                        side of cavity.
                dp: array of floats
                        Diameter of aerosol in size distribution
                ndp: array of floats
                        Number of aerosol in size distribution diameter bin.
        """
        if gstd <=1.0:
                raise ValueError('gstd must be greater than 1.0. Use trunc_mono for
                monodisperse aerosol')
        lower = gmean/gstd**3 #3 sigma below geometric mean
        upper = gmean*gstd**3 #3 sigma above geometric mean
        #define log normal distribution
        ithPart = lambda dp, dpgi, sigmagi: (1/(np.sqrt(2*np.pi)*np.log(sigmagi)*dp))*\
                np.exp(-(np.log(dp)-np.log(dpgi))**2/(2*np.log(sigmagi)**2))
        #create diameter array
```

```
        dp = np.logspace(np.log10(lower),np.log10(upper),int((upper - lower)/20)+5)
        #create weights for lognormal distribution
        ndp = ithPart(dp,gmean,gstd)
        trunc_result = trunc_size_dist(n, dp, ndp, fullOutput, inst_settings)

        if fullOutput==False:
                if returnDist == True:
                        return trunc_result, dp, ndp
                else:
                        return trunc_result
        else:
                if returnDist == True:
                        return trunc_result + (dp, ndp)
                else:
                        return trunc_result
def trunc_size_dist(n, dp, ndp, fullOutput=False, inst_settings = settings()):
        """
        Compute the SSA correction due to truncation for the CAPS-PM-SSA for polydisperse
        aerosol with size distribution. The truncation follows as the inverse of the SSA
        correction given.
        Uses Bohren-Huffman Mie algorithm, via PyMieScatt, to compute the correction given
        aerosol index of refraction, aerosol distribution statistics, and wavelength. It
        is best to use a continuos, compactly-supported distribution. A truncated and
        ideal Mie scattering coefficient is calculated at several points within the
        geometry of the CAPS, and integrated. The correction is derived from a ratio of
        the integrals (ideal case in the numerator). The results are normalized to the
        truncation calculated for 150nm monodisperse aerosol. Informaitonabout the z axis
        points in the calculation, Mie scattering coefficeints, and angles used to compute
        truncated Mie scattering coefficients can be output by setting fullOutput=True.

        Parameters
        ----------
        n : complex float
                Refractive index of aerosol
        dp : array of floats
                Diameter data for size distributions
        ndp : array of floats
                Number concentration (not normalzied)  for size distribution data. Must be
                same size as dp
        wavlen : float, optional
                Wavelength for CAPS instrument. The default is 450.
        fullOutput : boolean, optional
                If True, outputs angular, positional, and scattering coefficient data. The
                default is False.
        Raises
        ------
        ValueError
        dp and ndp arrays should be 1-D and have the same size.

        Returns
        -------
        trunc_corr: float
                Truncation for CAPS SSA measurement assuming monodisperse aerosol
        if fullOutput=True also outputs
                z_axis: array of floats
                        z-axis positions of particles within cavity. Units are in cm.
                bsca_trunc: float
                        Truncated scattering coefficient. Integrated from theta1 to theta2
                        across all z-axis values.
                bsca_ideal: float
                        Non-truncated scattering coefficient. Integrated from 0-180 degrees
                        z-axis values inside sphere. Considered zero outside of limits of
                        the integrating sphere.
                theta1: array of floats
                        Forward scattering angle in radians of integration, truncated by
                        opening on far side of cavity.
                theta2: array of floats
```

```
                Backward scattering angle in radians truncated by opening on near
                side of cavity.
"""
if len(dp) != len(ndp):
        raise ValueError('dp and ndp must have the same length')
wavlen, diam_sphere, diam_tube, extra_length, z1, z2, npos, ang_res, trunc_cal =\
        inst_settings.values()
k = (2*np.pi)/wavlen
su = np.empty([len(dp), int(180/ang_res)+1])
csca_dp = np.empty(len(dp))
for i1 in range(0,len(dp)):
t, _, _, unpol = ps.ScatteringFunction(n, wavlen, dp[i1], minAngle=0,\
                                       maxAngle=180,\
                                       angularResolution=ang_res)
#Do not set angular resolution higher than 0.1
csca_dp[i1] = 2*(np.pi/k**2) * trapz(unpol*np.sin(t),t)
su[i1] = unpol
bsca_mie = trapz(csca_dp * ndp, dp)
theta = t
z_axis = np.linspace(z1, z2, npos)#do not go below 1000
theta1 = np.empty(len(z_axis))
theta2 = np.empty(len(z_axis))
bsca_trunc = np.empty(len(z_axis))
bsca_ideal = np.empty(len(z_axis))
i = 0
for z in np.nditer(z_axis):
        if z != 0.5 * diam_sphere:
                alpha = np.arctan((0.5*diam_tube)/abs(0.5*diam_sphere - z))
                #forward scattering angle
        if z != -0.5 * diam_sphere:
                beta = np.arctan((0.5*diam_tube)/abs(-0.5*diam_sphere - z))
                #back scattering angle
        #alpha and beta need to be adjusted based on section of cell we are in
        if z < -0.5 * diam_sphere:#outside of sphere
                theta1[i] = alpha
                theta2[i] = beta
                bsca_ideal[i] = 0 #ideally light would not get into cavity from
        outside
        elif z == -0.5 * diam_sphere:
                theta1[i] = alpha
                theta2[i] = np.pi/2
                bsca_ideal[i] = bsca_mie
        elif -0.5 * diam_sphere <= z <= 0.5 * diam_sphere:#inside cavity
                theta1[i] = alpha
                theta2[i] = np.pi - beta
                bsca_ideal[i] = bsca_mie #ideally full scattering efficiency
        measured
        elif z == 0.5 * diam_sphere:
                theta1[i] = np.pi/2
                theta2[i] = np.pi - beta
                bsca_ideal[i] = bsca_mie
        elif z > 0.5 * diam_sphere:
                theta1[i] = np.pi - alpha
                theta2[i] = np.pi - beta
                bsca_ideal[i] = 0 #ideally light would not get into cavity from
        outside
        theta_trunc = theta[np.where(np.logical_and(theta >= theta1[i],\
                                                    theta <= theta2[i]))]
        Csca_trunc = np.empty(len(dp))
        for i2 in range(0, len(dp)):
                su_trunc = su[i2][np.where(np.logical_and(theta >= theta1[i],\
                                                          theta <= theta2[i]))]
                Csca_trunc[i2] = 2*(np.pi/k**2)*trapz(su_trunc *
                np.sin(theta_trunc),\
                                                      theta_trunc)
        bsca_trunc[i] = trapz(Csca_trunc * ndp, dp)
        #calculate scattering efficiency
```

```
        i+=1
trunc = trapz(bsca_trunc, z_axis)
ideal = trapz(bsca_ideal, z_axis)
#calculate trunc_corr. For regular calculations calculate top line. If determining
#truncationfor determining correction factor for calibrated data uncomment second
#line, comment first lineand determine the truncation correction
trunc_corr = (ideal / trunc)/trunc_cal #truncation
#trunc_corr = round(ideal / trunc, 4) #for determining truncation calibration
if fullOutput == True:
        return trunc_corr, z_axis, bsca_trunc, bsca_ideal, theta1, theta2
else:
        return trunc_corr
```

B Permission for Chapter 4

Chapter 4 was published in *Remote Sensing* which is an open access journal through MPDI. MPDI's Open Access and author permissions statement follows:

MDPI Open Access Information and Policy

All articles published by MDPI are made immediately available worldwide under an open access license. This means:

- everyone has free and unlimited access to the full-text of *all* articles published in MDPI journals;
- everyone is free to re-use the published material if proper accreditation/citation of the original publication is given;
- open access publication is supported by the authors' institutes or research funding agencies by payment of a comparatively low Article Processing Charge (APC) for accepted articles.

Permissions

No special permission is required to reuse all or part of article published by MDPI, including figures and tables. For articles published under an open access Creative Common CC BY license, any part of the article may be reused without permission provided that the original article is clearly cited. Reuse of an article does not imply endorsement by the authors or MDPI.

More information can be found at: https://www.mdpi.com/about/openaccess.